Towards the Detection of Anisotropic Magnetic Field Effects in Flavin-based Systems



Victoire Déjean
New College
University of Oxford

A thesis submitted
in partial fulfillment of
the requirements for the degree of

Doctor of Philosophy in Chemistry

Hilary 2021

Abstract

Towards the Detection of Anisotropic Magnetic Field Effects in Flavin-based Systems

Victoire Déjean, New College, Hilary 2021

Many animals, and in particular migratory birds, have the ability to use the geomagnetic field to navigate. The leading hypothesis to explain the origin of their compass sense is based on magnetosensitive radical pairs (RPs) formed in cryptochrome flavoproteins.

Numerous studies have demonstrated that the reactivity of light-induced RPs within flavin-based model systems and cryptochromes could be influenced by the magnitude of a magnetic field, giving rise to magnetic field effects (MFEs). Yet, many questions remain unanswered, especially regarding the ability of these systems to detect the direction of the field, which has been shown to provide critical information for navigation.

This work examines different chemical and spectroscopic approaches for their potential to yield or elucidate directionally sensitive magnetic field responses in flavin-based RPs. Chapter 1 explores whether selectively manipulating the magnetic properties of cryptochromes *in vivo* could disturb the bird's migratory behaviour. If it did, it would demonstrate that cryptochromes are i) sensitive to the field direction and ii) the primary magnetic sensor for avian magnetoreception. The potential of this ambitious experiment is assessed by examining the impact of isotopic substitution (which changes the hyperfine interaction driving the RPs' magnetosensitivity) on the MFE of model systems.

In vitro, the directionally dependent response of RPs to a field (anisotropic MFEs) can only be detected if the radicals are immobilised and oriented. In Chapters 2-3, several matrices are investigated as potential immobilisation media and the unexpected behaviour of flavins in glycerol solutions is further examined. Chapter 4 explores direct molecular alignment *via* protein crystallisation and introduces confocal microscopy as a powerful technique for the study of MFEs in crystals. By exploiting the capabilities of this technique, the MFEs of several cryptochromes, including avian cryptochromes, are investigated and contrasted, leading up to the examination of anisotropic MFEs in cryptochrome crystals (Chapter 5).

Acknowledgements

There are so many people to thank for their support over the past few years. First, of course, a huge thank you to Professor Christiane Timmel. You are a truly inspiring person and have been a fantastically supportive and fun supervisor. You made me feel at home in the lab and I am incredibly lucky to have been able to do my DPhil in your group! Thanks for all the spin-chemistry dinners, cake Mondays and invaluable life advice. On a side note, I will never be able to say the name of a certain pastry without being reminded of you!

I am very grateful to Professor Dirk Arts for being so accommodating and allowing us to have access to the Zeiss microscope which was used for a very large part of this thesis.

Marcin, I can honestly say that you taught me everything I know about coding and what being a rigorous sciencist means. Thanks for being a great friend and for making many late nights in the office a lot more bearable and suprisingly fun!

Jamie, I am really honored to have been able to show you the ropes on MAFIA (yes, I get to call it that at least once in my thesis!) and I am so glad you stayed for a DPhil and will be the one to take care of it from now on. Thanks for being such a friendly person, for the New College brunches and for making me feel a lot better about my own sense of direction! And thank you for digging into your Q drive to retrieve some of the data I needed for my thesis, you have been so incredibly helpful!

Thanks to Matt for being the ideal person to share a lab (and a windowless room in Russia) with, for being my English guru and for proof-reading a large part of this thesis. Your moral support during thesis writing was invaluable and I am really grateful for your friendship!

Next, I would like to acknowledge all the Part II students who worked with me over the years: Katherine, Steve and Bedwyr. It is always a lot nicer to work together with someone and I was really happy to do that with you all. Thanks for teaching me how to teach!

I am so grateful to all the members of the Timmel group for making the lab such a friendly place. Thanks, in particular, to Kevin, for being such an important pillar of the group, and to Gabriel and Ashley for sharing the EPR corner with me. Good luck to all the new DPhil students!

I have been very lucky to meet so many incredible friends in Oxford. Mirjam, you are the best friend I could have asked for to share the DPhil adventure with! Thanks for sticking by me through all the highs and lows of my life in the past few years. I am so happy we get to submit our theses together!

Living in ‘Marston manor’ and ‘Regent palace’ was definitely one the highlights of my

life in Oxford. Thanks to Mirjam, Fabrice, Sam, Naveen and Aaron (and Andrew!) for being fantastic housemates. I absolutely loved our Catan and G&Ds nights, and I had so much fun trying to light a BBQ with you! I really miss you guys!

Life in lockdown would have been infinitely harder without the support of my fantastic housemates Fred, Carla and Thomas (and Giorgia and Aeron the year before too). Thanks for supporting me during thesis writing and for dragging me to the MCR bar for a quick break. I will always have fond memories of our GBK and guitar nights. I still can't believe you did the impossible and managed to make me sing!

Of course, rowing has been a huge part of my life over the past few years and has given me so many great memories! Thanks to all the members of the New College Boat Club, and in particular to Joe, Veerle, Beth, Grace and Tanja. Waking up at 5:40 a.m. would have been a lot less fun without you! Rowing with you has been amazing and I cannot wait to do it one last time. GDBM, of course!

Thanks also to the New College MCR Committee 2020-2021. Attempting to make everyone's life a bit better during lockdown gave me a much needed sense of purpose and I was very lucky to be able to do that with all of you.

Finally, I need to thanks my parents. Je ne sais pas vraiment comment est-ce que j'ai atterri à Oxford, mais je suis certaine que ça a probablement quelque chose à voir avec le fait d'avoir appris l'existence des grandes écoles en passant devant l'ancienne Ecole Polytechnique ou d'avoir passé beaucoup de temps à la Villette. Merci de m'avoir offert une si belle vie! J'ai vraiment hâte de pouvoir vous voir en personne très bientôt!

Contents

Introduction **1**

0.1 Magnetoreception 1

0.2 Spin chemistry 2

0.2.1 Electron and nuclear spins in a magnetic field 3

Zeeman Interaction 4

Larmor precession 4

0.2.2 Spin-correlated radical pairs 5

Singlet and triplet states in a magnetic field 6

Spin-spin interactions 8

0.2.3 Magnetosensitivity of chemical reactions 9

Spin evolution of the radical pair 9

The radical pair mechanism 10

Low field effect 12

0.2.4 Requirements of a chemical compass 14

0.3 Flavin-based systems 15

0.3.1 Structure and general properties of flavins 15

0.3.2 Photocycles 17

MFEs in cryptochromes 17

MFEs in intermolecular model systems 18

0.4 Optical detection of magnetic field effects 20

0.4.1 Absorption-based techniques 20

0.4.2 Fluorescence-based techniques 22

0.4.3 MARY curves. 23

0.4.4 Enhanced magnetic field effects 24

1 Isotopic labelling of the Radical Pair 26

1.1 Fluorescence-detection of magnetic field effects 29

1.1.1 Low-volume PF MARY 29

Original experimental apparatus 30

Improvement to the apparatus 31

1.2 Effect of ^{13}C isotopic substitution on MFEs 34

1.2.1 Isotopic enrichment of FMN-ascorbic acid 35

Methods. 35

Results and discussion 35

1.2.2 Isotopic enrichment of FMN-HEWL 39

Methods. 39

Results and discussion 39

1.3 Conclusion and outlook 41

2 Encapsulating Flavins in Solid Matrices: Films, Gels and Viscous Solutions. 43

2.1 Immobilisation strategies 44

2.2 Rigid matrices considered for the physical entrapment of flavin-based systems 45

2.3 Experimental protocols 47

2.4 Photophysical characterisation 49

2.5 Determination of the degree of immobilisation 51

2.5.1 Introduction to fluorescence anisotropy 52

2.5.2 Steady-state anisotropy measurements 55

2.6 Magnetic field effects. 57

2.7 Using aqueous glycerol solutions as an immobilising medium 59

2.7.1 Methods. 59

2.7.2 Immobilising model systems 59

2.7.3 Immobilising cryptochromes 60

2.8 Conclusion and outlook 63

3 Magnetic Field Effects in Viscous Solutions 65

3.1 Methods 66

PF MARY 66

Transient absorption 66

Cavity ring-down spectroscopy 67

3.2 Origin of the magnetic field effect 67

3.2.1 Characteristics of the magnetic field effect 67

3.2.2 Photophysical characterisation of the system 68

3.2.3 Time-resolved MFE 69

3.3 Proposed mechanism 71

3.3.1 Potential mechanisms considered 71

Triplet-triplet annihilation 71

Reaction of FMN and glycerol 72

3.3.2 Formation of $FMNH^{\bullet}$ 72

Global target analysis 72

3.4 Conclusion and outlook 75

4 Detection of Magnetic Field Effects by Confocal Microscopy in flavin-lysozyme crystals 77

4.1 Experimental methods 78

4.1.1 Introduction to confocal microscopy 78

4.1.2 Apparatus 79

4.1.3 Data analysis 80

Spatially-resolved %MFE averaged temporally 81

%MFE averaged temporally and spatially 81

4.2 Results and discussion 83

4.2.1 Detection of magnetic field effects in solution 83

FMN-HEWL 83

Arabidopsis thaliana cryptochrome 1 (*At*Cry1) 84

4.2.2 Detection of magnetic field effects in crystals 86

Lysozyme crystal growth 86

MFE measurements 88

4.3 Conclusion and outlook 99

5 Isotropic and Anisotropic Magnetic Field Effects in Cryptochromes 101

5.1 Isotropic magnetic field effects in cryptochromes 102

5.1.1 Methods. 103

Materials 103

Apparatus 103

5.1.2 Results and discussion 104

Competition between fluorophores 104

Comparison of animal cryptochromes 111

5.2 Anisotropic magnetic field effects in cryptochrome crystals 115

5.2.1 Methods. 117

Crystal growth 117

MFE experiment 117

5.2.2 Results and discussion 118

5.3 Conclusion and outlook 120

Conclusion 122

Tables of Hyperfine Parameters 126

References 129

Introduction

Radical Pair Chemistry Under the Influence of Magnetic Fields

0.1 Magnetoreception

Many species within the animal kingdom rely on magnetic cues to navigate.[1] Night-migratory songbirds, such as European robins, are a prominent example and use the geomagnetic field, along with other navigational cues, to migrate over thousands of kilometres. This ability to detect magnetic fields – magnetoreception – has been the subject of scientific conjectures for several decades. Yet, the biophysical mechanism by which this information is detected is a much-debated question and remains unclear.[2] Two viable hypotheses, one based on magnetite crystals and the other on radical pairs, have emerged.

The first hypothesis postulates that magnetite crystals located in the bird's beak could interact with the Earth's magnetic field. The resulting field-induced alignment of the crystals (similar to a compass needle) would then trigger a neural response.[3,4] On the other hand, the second hypothesis, which was first proposed by Schulten *et al.* in 1978, involves magnetically sensitive spin-correlated radical pairs in cryptochrome flavoproteins immobilised in the retina.[5] More specifically, under blue-light illumination, the photoreduction of the flavin cofactor buried inside the protein is mediated by electron transfers along a chain of tryptophan residues. The resulting radical pair formed with the terminal, surface-exposed tryptophan is magnetosensitive and could, therefore, trigger a signalling cascade in the visual nervous system, essentially enabling the birds to see the field.[6]

Behavioural studies suggested that both hypotheses might in fact be involved in two complementary aspects of navigation.[1] Indeed, to navigate, animals need two distinct pieces of information: their location (map sense) and the direction they need to follow to reach their goal (compass sense). Magnetite crystals could be involved in the magnetic-map sense whereas cryptochromes could form the basis of the magnetic compass sense. However, recent developments, which suggest that the iron-rich structures found in the birds' beak are in fact not associated with the neural system, have weakened the magnetite

hypothesis.[7] On the other hand, a growing body of evidence supports a radical pair-based mechanism for the compass sense.

More specifically, following the discovery of the Emlen funnel, which allows the examination of a bird's behaviour and its response to an applied magnetic field in well-controlled conditions, multiple studies demonstrated that:[8]

- the compass sense exhibited by European robins was not sensitive to the polarity of the field but rather, to its inclination (angle between the field vector and the surface of the Earth);[9]
- the avian compass seems to operate best under blue or green light;[10]
- birds are disoriented under radio frequency fields.[11]

Further, Günther *et al.* recently observed that the expression levels of cryptochromes in European robins follow a seasonal pattern with increased expression during the migratory season.[12] As will be discussed below, and is examined in detail by Mouritsen and Hore, these findings are in line with a radical pair-based chemical compass.[13]

However, in spite of the substantial advances that have been made over the last few decades in the understanding of magnetoreception, hard evidence that the cryptochrome protein is the actual magnetoreceptor is lacking and several questions remain unanswered. In particular, although cryptochromes have been shown to be sensitive to the intensity of the field *in vitro*, a directionally dependent response to a magnetic field has yet to be measured. Such a directionally dependent magnetosensitivity, which is also referred to as an anisotropic magnetic field effect, is vital to function as a compass. To date, only a model system, a carotenoid-porphyrin-fullerene triad, has exhibited true compass behaviour at Earth-strength fields.[14] In an effort to prove the suitability of the cryptochrome protein as a chemical compass, this work explores several approaches for the measurement of anisotropic magnetic field effects in biologically relevant, flavin-containing systems.

0.2 Spin chemistry

Although, at first sight, it seems implausible that the interaction of a radical with the geomagnetic field (25-65 μT), which is several orders of magnitude smaller than the thermal energy, k_BT, could have any effect on the yield of a chemical reaction and determine an

animal's behaviour, it can be understood in light of the theoretical considerations detailed below.[15]

0.2.1 Electron and nuclear spins in a magnetic field

Spin is a quantum property of fundamental particles that is a form of intrinsic angular momentum. As such, it is defined by a vector $\mathbf{s}$ whose magnitude and projection onto an arbitrary axis (z) are quantised by the quantum numbers s and m_s, respectively:

$$\|\mathbf{s}\| = \hbar\sqrt{s(s+1)}, \tag{1}$$

$$s_z = m_s\hbar, \tag{2}$$

with $m_s = -s, -s+1, ..., s-1, s$. For an electron, the spin angular momentum quantum number is $s = 1/2$ and there are, therefore, two eigenstates $|\alpha\rangle = |s = 1/2, m_s = 1/2\rangle$ and $|\beta\rangle = |s = 1/2, m_s = -1/2\rangle$.

The most obvious physical manifestation of the electron spin is that the electron possesses a spin magnetic moment $\boldsymbol{\mu}_\mathrm{e}$ defined by:

$$\boldsymbol{\mu}_\mathrm{e} = -\frac{g_\mathrm{e}\mu_\mathrm{B}}{\hbar}\boldsymbol{s}, \tag{3}$$

where $\mu_\mathrm{B} = \frac{e\hbar}{2m_\mathrm{e}}$ is the Bohr magneton, which represents a unit of magnetic moment, and $g_\mathrm{e} = 2.0023$ is the free electron g-factor, which is a correction factor that accounts for the anomalous behaviour of the electron compared to the classical approach. Within a radical, the g-factor of the electron deviates from g_e. This is mainly due to spin-orbit coupling and, therefore, the g-factor depends on the local environment of the electron.

Analogously, the magnetic moment associated with a nuclear spin $\boldsymbol{I}$ is defined by:

$$\boldsymbol{\mu}_\mathrm{n} = \frac{g_\mathrm{n}\mu_\mathrm{n}}{\hbar}\boldsymbol{I} = \gamma_\mathrm{n}\boldsymbol{I}, \tag{4}$$

where g_n is the nuclear g-factor, μ_n is the nuclear magneton and γ_n is the nuclear gyromagnetic ratio.

Zeeman Interaction

The interaction of a spin magnetic moment with an external magnetic field, $\boldsymbol{B}$, is the Zeeman interaction. The corresponding Hamiltonian is given by:

$$\hat{\mathcal{H}}_{\mathrm{eZ}} = -\hat{\boldsymbol{\mu}}_{\mathrm{e}} \cdot \boldsymbol{B} = \frac{\mu_{\mathrm{B}}}{\hbar} \hat{\boldsymbol{s}} \cdot \boldsymbol{g} \cdot \boldsymbol{B} \tag{5}$$

where $\boldsymbol{g}$ is a tensor accounting for the anisotropy of the interaction between $\boldsymbol{s}$ and $\boldsymbol{B}$. In the case of a fast-tumbling molecule in solution, $\boldsymbol{g}$ becomes isotropic and is represented by a scalar:

$$\hat{\mathcal{H}}_{\mathrm{eZ}} = \frac{g\mu_{\mathrm{B}}}{\hbar} \hat{\boldsymbol{s}} \cdot \boldsymbol{B}. \tag{6}$$

For a field of magnitude B_0 aligned along the z-axis, the eigenvalues of the Zeeman Hamiltonian are:

$$E_{\mathrm{eZ}} = \pm \frac{1}{2} g\mu_{\mathrm{B}} B_0. \tag{7}$$

Thus, in the presence of a magnetic field, the degeneracy of the α and β states is lifted and they become energetically separated by the Zeeman splitting $\Delta E_{\mathrm{eZ}} = g\mu_{\mathrm{B}} B_0$.

Similarly, the Zeeman Hamiltonian resulting from the interaction of the magnetic field with a nuclear spin $\boldsymbol{I}$ is given by:

$$\hat{\mathcal{H}}_{\mathrm{nZ}} = -\gamma_{\mathrm{n}} \hat{\boldsymbol{I}} \cdot \boldsymbol{B}. \tag{8}$$

Because $\gamma_{\mathrm{n}} \ll \gamma_{\mathrm{e}}$, the contribution of the nuclear Zeeman Hamiltonian to the global Hamiltonian of the system is usually neglected.

Larmor precession

The spin is an angular momentum and its components' projection operators do not commute with one another. Thus, there is an inherent uncertainty on the s_x and s_y components if s_z is known, meaning that the spin vector can be thought of as being located somewhere on a cone around the z-axis whose side length and height are known (quantised by s and s_z, respectively). This is the basis of the vector model which is a classical, pictorial representation of a spin system and is often used to illustrate some of the intricacies of spin chemistry (see below).

The general behaviour of the spin vector can be elucidated by considering the time

evolution of the wavefunction of the system $|\psi\rangle$ under the Hamiltonian $\hat{\mathcal{H}}_{eZ}$, which is described by the time-dependent Schrödinger equation:

$$i\hbar\frac{\partial\psi}{\partial t} = \hat{\mathcal{H}}_{eZ}\psi, \tag{9}$$

from which the time evolution of the expectation value of an operator $\hat{\mathcal{O}}$ can be derived:

$$\frac{d\langle\hat{\mathcal{O}}\rangle}{dt} = \frac{i}{\hbar}\langle[\hat{\mathcal{H}}_{eZ}, \hat{\mathcal{O}}]\rangle. \tag{10}$$

Using Equation 10 for $\hat{s}_x$ and $\hat{s}_y$ yields:

$$\frac{d\langle\hat{s}_x\rangle}{dt} = -\frac{g\mu_\mathrm{B}}{\hbar}B_0\langle\hat{s}_y\rangle, \text{ and} \tag{11}$$

$$\frac{d\langle\hat{s}_y\rangle}{dt} = \frac{g\mu_\mathrm{B}}{\hbar}B_0\langle\hat{s}_x\rangle, \tag{12}$$

with solutions:

$$\langle\hat{s}_x\rangle = \frac{\hbar}{\sqrt{2}}\cos(\frac{g\mu_\mathrm{B}}{\hbar}B_0t + \theta), \text{ and} \tag{13}$$

$$\langle\hat{s}_y\rangle = \frac{\hbar}{\sqrt{2}}\sin(\frac{g\mu_\mathrm{B}}{\hbar}B_0t + \theta), \tag{14}$$

where θ is an arbitrary constant whose value is not determined. Thus, although the exact components of the spin vector $\boldsymbol{s}$ are unknown, its general behaviour consists of a precession movement around the magnetic field axis with a frequency, the so-called Larmor frequency, defined by:

$$\omega_\mathrm{L} = \frac{g\mu_\mathrm{B}}{\hbar}B_0. \tag{15}$$

0.2.2 Spin-correlated radical pairs

As mentioned in Section 0.1, the cryptochrome hypothesis, which has been proposed as a possible explanation for magnetoreception, is based on the reactivity of radical pairs, which contain two unpaired electrons. If both electron spins are randomly oriented with respect to one another, the radical pair is referred to as uncorrelated. For example, this is the case of the random encounter of two radicals in solution. On the other hand, when the two electron spins of a radical pair are mutually oriented in a specific way, it is described as spin-correlated. Such radical pairs are formed under conservation of spin angular momentum,

for instance following an electron transfer or bond homolysis. They play a crucial role in the radical pair mechanism and their behaviour is governed by the magnetic interactions detailed below.

Singlet and triplet states in a magnetic field

Coupled spins Based on Section 0.2.1, a system comprised of two electrons can exist in four states: $|\alpha\alpha\rangle$, $|\alpha\beta\rangle$, $|\beta\alpha\rangle$, and $|\beta\beta\rangle$, which constitute the so-called product basis. However, in the presence of strong inter-radical interactions, the product basis is not an eigenbasis of the system's Hamiltonian anymore and the coupled basis, in which the total spin angular momentum is considered, is more relevant. The total spin angular momentum, $\boldsymbol{S}$, is the vector sum of the individual spins and is defined by: $\boldsymbol{S} = \boldsymbol{s_1} + \boldsymbol{s_2}$. Similar to an individual spin, its length and projection onto an arbitrary axis (z) are quantised by the quantum numbers S and M_S, respectively:

$$\|\mathbf{S}\| = \hbar\sqrt{S(S+1)}, \tag{16}$$

$$S_z = M_S\hbar \tag{17}$$

The values taken by the overall spin quantum number can be derived using the Clebsch-Gordan series:

$$S = |s_1 - s_2|, |s_1 - s_2 + 1|, \ldots, |s_1 + s_2 - 1|, s_1 + s_2, \tag{18}$$

$$M_S = -S, -S+1, \ldots, S-1, S \tag{19}$$

Hence, for two electrons, $S = 0, 1$. For $S = 1$, there are three possibles states, which are known as the triplet states and are labelled T_+, T_0, and T_-, according to their respectives M_S values. In the case of $S = 0$, there is only one possibility, $M_S = 0$, which gives rise to the singlet state, labelled S. The vector representations of the singlet and triplet states

are shown in Figure 1. The coupled and product bases are related as follows:

$$
\begin{aligned}
|\mathrm{T}_+\rangle &= |\alpha\alpha\rangle\,, \\
|\mathrm{S}\rangle &= \frac{1}{\sqrt{2}}(|\alpha\beta\rangle - |\beta\alpha\rangle), \\
|\mathrm{T}_0\rangle &= \frac{1}{\sqrt{2}}(|\alpha\beta\rangle + |\beta\alpha\rangle), \\
|\mathrm{T}_-\rangle &= |\beta\beta\rangle\,.
\end{aligned}
\tag{20}
$$

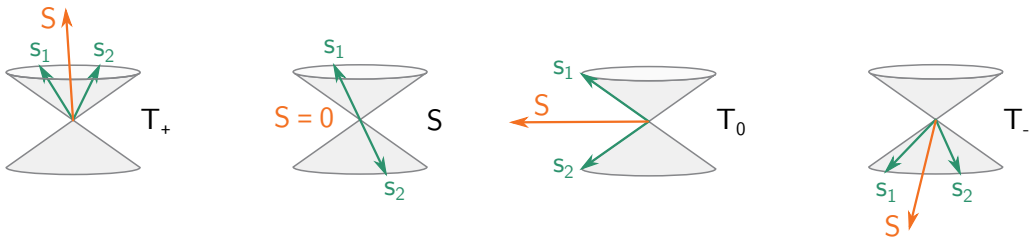


Figure 1: Representation of the singlet and triplet spin states of a radical pair by the vector model. The individual spins $\boldsymbol{s_1}$ and $\boldsymbol{s_2}$ of the two electrons precess about their quantisation axis (vertical in the Figure). Although the total spin angular momentum, $\boldsymbol{S}$, precesses around the quantisation axis as well, its precession cone is not depicted for clarity.

Zeeman interaction Similar to individual spins, the total spin of a radical pair can interact with an external magnetic field, $\boldsymbol{B}$, by its magnetic moment, hence lifting the degeneracy of the S-T_0 manifold and the $\mathrm{T}_\pm$ states. This is clearly visible in Figure 2, in which the effect of the Zeeman and exchange (see below) interactions are depicted.

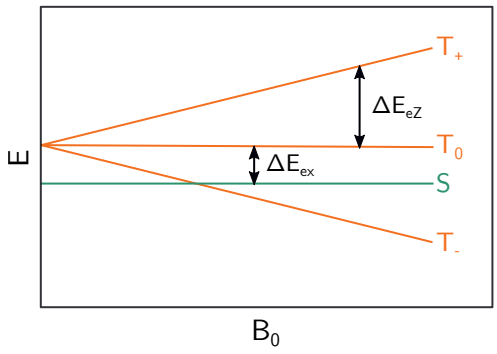


Figure 2: Energy diagram illustrating the impact of the Zeeman and exchange interactions on the singlet and triplet states of a radical pair.

Spin-spin interactions

Hyperfine interaction The interaction between an electron spin and nuclear spins is referred to as the hyperfine interaction. It comprises two different contributions: the dipolar coupling and the Fermi contact interaction. The dipolar contribution arises from the interaction between the electron magnetic moment and the local magnetic field generated by the nuclear magnetic moments. As the interaction depends on the relative orientations of the electron and nuclear magnetic moments, it is anisotropic. The Fermi contact interaction stems from the finite electron density at the nucleus and is isotropic. The hyperfine Hamiltonian is given by:

$$\hat{\mathcal{H}}_{\text{hfc}} = \hat{\boldsymbol{s}} \cdot \boldsymbol{A} \cdot \hat{\boldsymbol{I}}, \tag{21}$$

where $\hat{\boldsymbol{s}}$ and $\hat{\boldsymbol{I}}$ are the electron and nuclear spin angular momentum operators, respectively, and $\boldsymbol{A}$ is the hyperfine coupling tensor. In solution, the dipolar contribution to $\boldsymbol{A}$ averages out due to fast molecular tumbling and only the isotropic component, a, remains. The resulting Hamiltonian is given by:

$$\hat{\mathcal{H}}_{\text{hfc}} = a\, \hat{\boldsymbol{s}} \cdot \hat{\boldsymbol{I}} \tag{22}$$

with a defined by:

$$a = \frac{2\mu_0}{3} g\, \mu_{\text{B}}\, g_{\text{n}}\, \mu_{\text{n}}\, |\psi_0(0)|^2 \tag{23}$$

where μ_0 is the vacuum permeability and $|\psi_0(0)|^2$ is the overlap integral corresponding to the electron spin density at the nucleus.

Exchange interaction The exchange interaction is a purely quantum mechanical effect with no classical counterpart. It is a direct consequence of the Pauli principle which states that the wavefunctions describing fermions (such as electrons) must be antisymmetric with respect to particle exchange.

The overall wavefunction of the system can be expressed as a product of a spin wavefunction and a spatial wavefunction: $\Psi_{\text{RP}} = \psi_{\text{space}}\psi_{\text{spin}}$. The spin wavefunctions of the singlet and triplet states are antisymmetric and symmetric, respectively (see Equation 20). Therefore, to satisfy the Pauli principle, the singlet must be paired with a symmetric ψ_{space} while the triplet states are associated with an antisymmetric ψ_{space}. This difference

in spatial symmetry between the singlet and triplet states, in turn, affects the probability of close approach of the electrons and alters the electron-electron repulsion, giving rise to a splitting in energy, as depicted in Figure 2. The corresponding Hamiltonian is defined as:

$$\hat{\mathcal{H}}_{\mathrm{ex}} = -2J\hat{\boldsymbol{s_1}} \cdot \hat{\boldsymbol{s_2}}, \tag{24}$$

where $\hat{\boldsymbol{s_1}}$ and $\hat{\boldsymbol{s_2}}$ are the spin angular momentum operators of the two electron spins and J is the exchange coupling constant. The exchange interaction has a strong distance dependence and decrease exponentially with electron-electron separation. It is usually considered negligible for inter-radical distances larger than $\sim$1 nm. Importantly, the singlet and triplet states are eigenstates of $\hat{\mathcal{H}}_{\mathrm{ex}}$. Thus, after formation of the RP, the inter-radical distance is small and the exchange interaction is, therefore, quite strong and locks the RP into its initial spin state.

Dipolar interaction The dipolar interaction describes the interaction between the magnetic dipoles of two electron spins. The weak local magnetic field experienced by one electron due to the magnetic moment of the other lifts the degeneracy of the triplet states at zero-field. The corresponding Hamiltonian is given by:

$$\hat{\mathcal{H}}_{\mathrm{d}} = \hat{\boldsymbol{S}} \cdot \boldsymbol{D} \cdot \hat{\boldsymbol{S}}, \tag{25}$$

where $\hat{\boldsymbol{S}} = \hat{\boldsymbol{s_1}} + \hat{\boldsymbol{s_1}}$ and $\boldsymbol{D}$ is the dipolar coupling tensor describing the interaction. Rapid molecular motion can cause the anisotropic dipolar interaction to average out. Further, it is inversely proportional to r^3, where r is the distance between the radicals. Thus, it is weaker than the exchange interaction at small RP separations but becomes stronger at larger distances.

0.2.3 Magnetosensitivity of chemical reactions

Spin evolution of the radical pair

In the absence of relaxation (see below), the system evolves under the influence of its spin Hamiltonian:

$$\hat{\mathcal{H}} = \hat{\mathcal{H}}_{\mathrm{eZ}} + \hat{\mathcal{H}}_{\mathrm{hfc}} + \hat{\mathcal{H}}_{\mathrm{ex}} + \hat{\mathcal{H}}_{\mathrm{d}}. \tag{26}$$

Immediately after formation, the radicals comprising the radical pair are close enough that the exchange and dipolar interactions are dominant. The system is therefore locked into its initial spin state. When the radicals are sufficiently separated, the electron-electron interactions decrease significantly and the singlet and triplet states are no longer eigenstates of the system. Therefore, the radical pair is in a non-stationary state and undergoes time-dependent coherent mixing between the singlet and triplet states under the influence of the Zeeman and hyperfine Hamiltonians. This coherent singlet-triplet interconversion is central to the radical pair mechanism discussed below as it is magnetosensitive. Indeed, due to the Zeeman interaction, strong magnetic fields isolate the $T_{\pm}$ states from S and T_0, thereby decreasing the efficiency of singlet-triplet mixing.

The radical pair mechanism

The radical pair mechanism (RPM), whose very general principle is illustrated in Figure 3, describes how magnetic fields can influence the yields and kinetics of chemical reactions involving radical pairs as intermediates and give rise to magnetic field effects (MFEs), which arise if:

- a spin-correlated radical pair is formed in either a pure singlet or triplet state;
- magnetosensitive coherent singlet-triplet interconversion takes place, affecting the relative proportions of the singlet and triplet states;
- the radical pair undergoes spin-selective reactions such that the singlet and triplet states have different fates or different recombination rates.

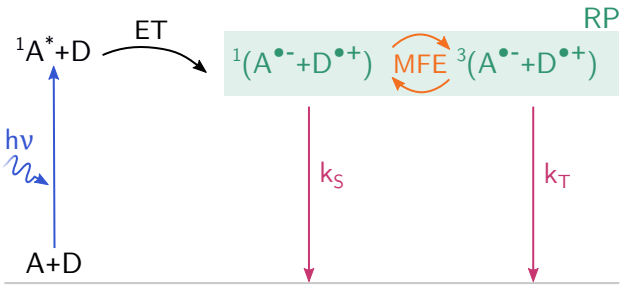


Figure 3: Simplified photoscheme illustrating the general principle of the radical pair mechanism. A spin-correlated radical pair comprised of an electron acceptor (A) and an electron donor (D) is formed via electron transfer. It then undergoes magnetosensitive interconversion between the singlet and triplet states whose different fates are represented by the different reaction rates.

As the radical pair is generated in a non-equilibrium state, small changes in any of the magnetic interactions described above can strongly influence the efficiency of spin mixing and, therefore, the outcome of the reaction. This can be better understood using the vector model introduced above. Based on the vector representations of the singlet and triplet states, it seems that $S - T_0$ mixing stems from spin precession dephasing. The precession frequency, as defined by Equation 15, is a function of the g-factor and the applied magnetic field. Thus, any differences in the g-factors and local fields of the two electrons would give rise to $S - T_0$ mixing. On the other hand, processes which lead to a change in the m_s value of either electron (a spin-flip) foster $S - T_\pm$ mixing. The main singlet-triplet interconversion mechanisms are discussed below.

Hyperfine mechanism In the high-field limit, the electron spins precess about the direction of the applied magnetic field and the magnetic moments of the neighbouring nuclei behave as a perturbation. Thus, the local field experienced by an electron due to its interaction with a nucleus I is given by: $B_{\text{loc}} = B_0 + am_I$. This, in turn, impacts the electron's Larmor frequency and drives spin-mixing, which occurs at a frequency corresponding to the difference in the Larmor frequencies of the two electrons.

Δg mechanism This mechanism arises when the two electrons are characterised by different g-factors. The mixing rate is governed by the difference in the Larmor frequencies: $\Delta\omega = \Delta g \mu_{\text{B}} B_0/\hbar$.

For effective spin-mixing to occur, transitions must take place within the radical pair lifetime, which is usually of the order of 10^{-8} s. For typical carbon-centered organic radical pairs, $\Delta g = 0.001$.[13] Therefore, to satisfy the prescribed condition for significant spin-mixing, magnetic fields of the order of 10^4 T must be applied, which is far higher than the geomagnetic field and the fields considered within the scope of this thesis.

Relaxation mechanism Additional incoherent spin mixing is driven by the relaxation of the spins, which is caused by random fluctuations of anisotropic interactions and comprises two contributions. Spin-lattice relaxation restores the thermal equilibrium and affects the z-component of the spins. It gives rise to 'spin-flips' and, therefore, to $S - T_\pm$ mixing. It is characterised by the spin-lattice relaxation time, T_1. Meanwhile, spin-spin relaxation

relaxes the transverse component of the spins, hence destroying phase coherences between the spins. It is characterised by the spin-spin relaxation time, T_2. The rates of relaxation depend on the rotational correlation times of the radicals, which characterise the tumbling of the molecules and are, broadly speaking, representative of the fluctuation in local field. For a typical organic radical in a non-viscous solution, relaxation times are of the order of 10^{-6}-10^{-5} s.[13] Hence, relaxation is usually not rapid enough to have a significant impact on the radical pair spin coherence.

Low field effect

From the considerations above, the hyperfine interaction seems to be the main driving force of the singlet-triplet interconversion for the systems examined in this thesis. So far, only the high-field regime was considered.

In the low-field region ($B_0 \lesssim a$), which is of relevance for magnetoreception, the interplay between the hyperfine and Zeeman contributions is more complex. In this case, the electron spins precess about the resultant of the external and hyperfine fields. As the hyperfine fields of the two radicals do not only differ in magnitude, but also in direction, the electron spins precess about different axes at different rates, hence giving rise to additional spin-mixing pathways compared to zero-field conditions. This increased inconversion is referred to as the low field effect (LFE).[16,17] Depending on the system under investigation and the experimental conditions, this low field feature can be very prominent or not visible at all.

The vector model provides a satisfactory, yet qualitative, insight into the origin of the LFE. Further understanding can be gained by examining the initial density matrix of a radical pair. Closely following previous theoretical studies, a simple radical pair is considered.[17] It is comprised of electrons A and B, and a proton H coupled to A via an isotropic hyperfine interaction a. The spin Hamiltonian of the system, in which all but crucial interactions have been removed for simplicity, is:

$$\hat{\mathcal{H}} = \hat{\mathcal{H}}_{\mathrm{eZ}} + \hat{\mathcal{H}}_{\mathrm{hfc}} \tag{27}$$

$$= \omega(\hat{s}_{Az} + \hat{s}_{Bz}) + a\hat{\boldsymbol{s}}_{\boldsymbol{A}} \cdot \hat{\boldsymbol{I}}_{\boldsymbol{H}}, \tag{28}$$

The eigenstates of $\hat{\mathcal{H}}$ and associated eigenvalues are:

$$\left.\begin{array}{ll}
|1\rangle = |\mathrm{T}_+\alpha\rangle & \epsilon_1 = \omega + \frac{a}{4} \\
|2\rangle = \frac{c_-}{2}(|\mathrm{T}_0\alpha\rangle - |\mathrm{S}\alpha\rangle) + \frac{c_+}{\sqrt{2}}|\mathrm{T}_+\beta\rangle & \epsilon_2 = \frac{\omega+\Omega}{2} - \frac{a}{4} \\
|3\rangle = \frac{1}{\sqrt{2}}(|\mathrm{T}_0\alpha\rangle + |\mathrm{S}\alpha\rangle) & \epsilon_3 = \frac{a}{4} \\
|4\rangle = \frac{1}{\sqrt{2}}(|\mathrm{T}_0\beta\rangle - |\mathrm{S}\beta\rangle) & \epsilon_4 = \frac{a}{4} \\
|5\rangle = \frac{c_+}{2}(|\mathrm{T}_0\beta\rangle + |\mathrm{S}\beta\rangle) + \frac{c_-}{\sqrt{2}}|\mathrm{T}_-\alpha\rangle & \epsilon_5 = -\frac{\omega-\Omega}{2} - \frac{a}{4} \\
|6\rangle = |\mathrm{T}_-\beta\rangle & \epsilon_6 = -\omega + \frac{a}{4}
\end{array}\right\} \epsilon = a/4 \text{ when } B_0 = 0 \tag{29}$$

$$\left.\begin{array}{ll}
|7\rangle = \frac{c_+}{2}(|\mathrm{T}_0\alpha\rangle - |\mathrm{S}\alpha\rangle) - \frac{c_-}{\sqrt{2}}|\mathrm{T}_+\beta\rangle & \epsilon_7 = \frac{\omega-\Omega}{2} - \frac{a}{4} \\
|8\rangle = \frac{c_-}{2}(|\mathrm{T}_0\beta\rangle + |\mathrm{S}\beta\rangle) - \frac{c_+}{\sqrt{2}}|\mathrm{T}_-\alpha\rangle & \epsilon_8 = -\frac{\omega+\Omega}{2} - \frac{a}{4}
\end{array}\right\} \epsilon = -3a/4 \text{ when } B_0 = 0$$

where α and β denote the spin states of the nucleus, $c_\pm = \sqrt{1 \pm \omega/b}$ and $\Omega = \sqrt{\omega^2 + a^2}$. The state of any quantum mechanical system can be entirely described by the density matrix $\rho = |\psi\rangle\langle\psi|$, where ψ is the wavefunction of the system. The diagonal elements of the density matrix, called populations, indicate the probabilities of finding the particle in a specific eigenstate. The off-diagonal elements represent the coherences between the eigenstates which give rise to singlet-triplet interconversion.

As mentioned above, the LFE stems from the existence of additional mixing pathways compared to zero-field conditions, which will be examined first. Assuming the model radical pair considered is created in the singlet state, under zero-field conditions, the density matrix of the system immediately after the formation of the radical pair is:

$$\rho = \frac{1}{2}\left(|\mathrm{S}\alpha\rangle\langle\mathrm{S}\alpha| + |\mathrm{S}\beta\rangle\langle\mathrm{S}\beta|\right) \tag{30}$$

$$= \begin{array}{c} \\ \langle 1| \\ \langle 2| \\ \langle 3| \\ \langle 4| \\ \langle 5| \\ \langle 6| \\ \hline \langle 7| \\ \langle 8| \end{array} \begin{array}{c} \begin{array}{cccccc|cc} |1\rangle & |2\rangle & |3\rangle & |4\rangle & |5\rangle & |6\rangle & |7\rangle & |8\rangle \end{array} \\ \left(\begin{array}{cccccc|cc} 0 & 0 & 0 & 0 & 0 & 0 & 0 & 0 \\ 0 & \frac{1}{4} & -\kappa & 0 & 0 & 0 & -\kappa & 0 \\ 0 & -\kappa & \frac{1}{8} & 0 & 0 & 0 & \frac{1}{8} & 0 \\ 0 & 0 & 0 & \frac{1}{4} & -\kappa & 0 & 0 & \kappa \\ 0 & 0 & 0 & -\kappa & \frac{1}{8} & 0 & 0 & -\frac{1}{8} \\ 0 & 0 & 0 & 0 & 0 & 0 & 0 & 0 \\ \hline 0 & -\kappa & \frac{1}{8} & 0 & 0 & 0 & \frac{1}{8} & 0 \\ 0 & 0 & 0 & \kappa & -\frac{1}{8} & 0 & 0 & \frac{1}{8} \end{array}\right) \end{array} \tag{31}$$

where $\kappa = \frac{1}{4\sqrt{2}}$. Only coherences between non-degenerate eigenstates are active and contribute to spin-mixing. At zero field, eigenstates $|1\rangle$ to $|6\rangle$ and $|7\rangle$ to $|8\rangle$ are degenerate with eigenvalues $a/4$ and $-3a/4$, respectively. Therefore, the coherences $|2\rangle \leftrightarrow |3\rangle$ and $|4\rangle \leftrightarrow |5\rangle$ are independent of time and do not contribute to spin mixing. On the other hand, the coherences $|2\rangle \leftrightarrow |7\rangle$, $|3\rangle \leftrightarrow |7\rangle$, $|4\rangle \leftrightarrow |8\rangle$ and $|5\rangle \leftrightarrow |8\rangle$ undergo periodic oscillations of frequency a. When the magnetic field is switched on, the zero-field degeneracies are lifted. In the low field regime, $\Omega \sim a$ and the newly non-degenerate states are split by approximately $\omega/2$, based on Equation 29. The application of a weak static field, therefore, engenders oscillations of frequency $\omega/2$, increasing the singlet-triplet interconversion and giving rise to the low field effect.

0.2.4 Requirements of a chemical compass

In light of the elements of spin chemistry discussed above, appreciable magnetic field effects can stem from the radical pair mechanism when the following conditions are met:

- at least one radical has nuclei with non-zero hyperfine couplings;
- the radical pair's lifetime is long enough for appreciable spin mixing to take place;
- the radical pair undergoes spin-selective reactions, hence allowing the magnetic field effect on spin mixing to be detected;

- spin relaxation is relatively slow with respect to the radical pair lifetime so that the spin-correlation of the electrons is preserved.

Further, in order to act as a compass, the radical pair must respond to the direction of the field. Directional information has been suggested to originate from anisotropic hyperfine couplings.[5,6] Indeed, if the hyperfine couplings of at least one of the two radicals are anisotropic, the extent of spin mixing will depend on the relative orientations of the radicals with respect to the external field. Thus, if the orientations of the radicals are fixed, then a change in the direction of the external field will affect the yield of the reaction, *i.e.* the system acts as a compass.

0.3 Flavin-based systems

In the putative magnetoreceptor cryptochrome, the highly conserved photolyase homology domain noncovalently binds a flavin cofactor. Flavins are a family of yellow compounds that are essential and ubiquitous cofactors in biology. Indeed, flavoproteins are known to be involved in a variety of processes including light-induced DNA repair, the entrainment of the circadian rythms and phototropism.[13,18,19]

0.3.1 Structure and general properties of flavins

As depicted in Figure 4, all flavins contain an isoalloxazine group but differ in their ribityl chain, $C_5H_{10}O_4R$', where R' can be:

- a hydrogen atom: riboflavin (RF) is the precursor of all biologically important flavins in biology. It is commonly known as vitamin B2;
- a phosphate group: flavin mononucleotide (FMN) is the most commonly used flavin for magnetoreception proof-of-principle studies;
- an adenine dinucleotide: flavin adenine dinucleotide (FAD) is the cofactor present in cryptochromes;

Flavin molecules are photosensitive and photodegrade quite easily. Lumichrome (in which the whole ribityl chain is replaced by a hydrogen atom) and lumiflavin (in which the whole ribityl chain is replaced by a methyl group) are the most common photodegradation

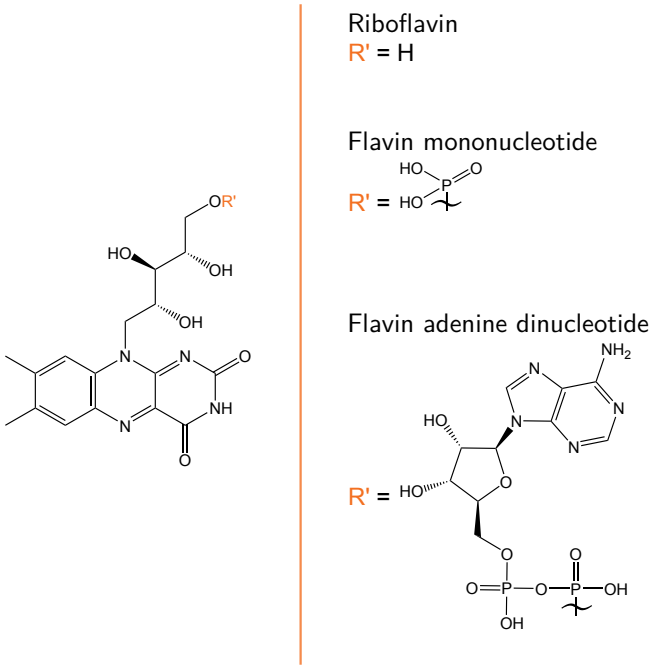


Figure 4: Chemical structures of the flavins mentioned in this work.

products.[20]

Flavins are well-known for their ability to participate in both one-electron and two-electron transfers and can exist in three different redox states: fully-oxidised, semiquinone, and fully reduced (see Figure 5).[18] A flavin molecule is usually in its fully oxidised form and can easily accept an electron from a suitable electron donor, hence forming the semiquinone radical, which can take part in the radical pair mechanism.

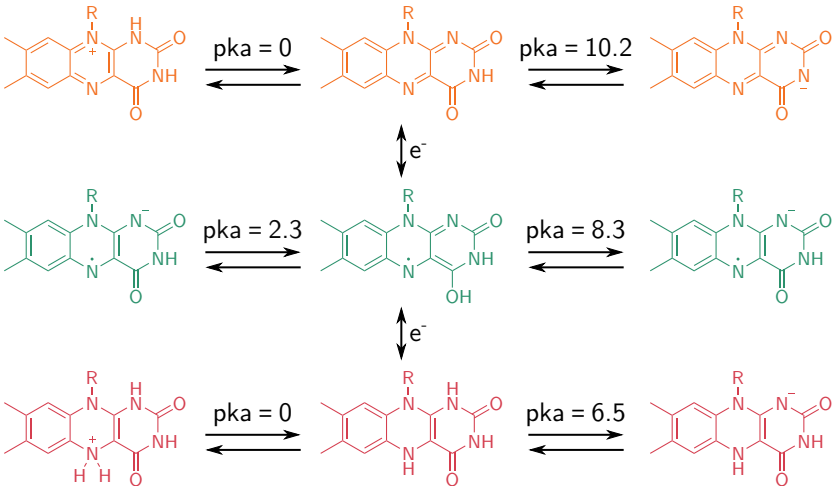


Figure 5: Redox and protonation states of flavins. Top: fully oxidised. Middle: semiquinone. Bottom: fully reduced.

The spectral properties of flavin derivatives are mostly determined by the isoalloxazine moiety and highly depend on the redox and protonation state of the chromophore. In their fully oxidised form, as shown in Figure 6, flavins exhibit UV and visible absorption. The bands at ∼375 nm and ∼445 nm correspond to the $S_0 \rightarrow S_1, \pi \rightarrow \pi^*$ and $S_0 \rightarrow S_2, n \rightarrow \pi^*$ transitions, respectively.[21] The exact positions of the two bands depend on the environment of the molecule.

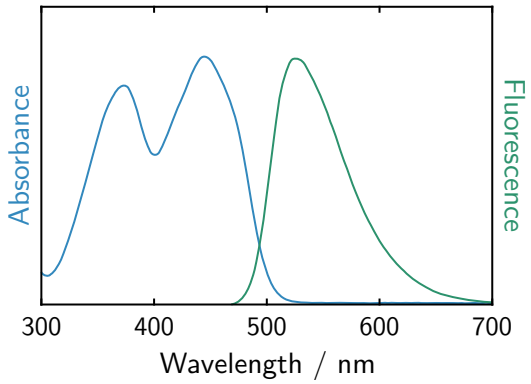


Figure 6: Absorption and fluorescence spectra of FMN in its oxidised form in water.

Flavins exhibit strong fluorescence at around ∼530 nm with a fluorescence quantum yield of $\phi = 0.26$ for FMN in water.[22]

Conversely, lumichrome has a drastically different absorption spectrum and does not absorb beyond 450 nm but has a similar fluorescence profile to that of the other flavins.[23]

In flavoproteins, and in particular in cryptochromes, the protein backbone surrounding the cofactor affects its photophysical properties. Thus, the 445 nm absorption peak exhibits a characteristic vibronic structure consisting of shoulders on both sides (see Chapter 5). Further, the fluorescence quantum yield of FAD in cryptochromes is dramatically smaller than in solutions of free flavin, $\phi \sim 10^{-3}$.[24]

0.3.2 Photocycles

MFEs in cryptochromes

As depicted in Figure 7, in cryptochromes, blue light photoexcitation of the flavin cofactor is followed by rapid, intramolecular electron transfer along a triad or tetrad of tryptophan residues.[25,26] The resulting radical pair, $^1[FAD^{\bullet -}\ TrpH^{\bullet +}]$, referred to as RP_1, is singlet-born and undergoes coherent, field-sensitive interconversion with the triplet state. As

direct recombination from the triplet state is spin-forbidden, only the singlet radical pair can recombine to the ground state. However, both radical pair spin states can, usually via non-spin-selective protonation or deprotonation of either one or both radical partners, yield a second longer-lived radical pair, RP_2. As detailed above, large magnetic fields hinder spin mixing and, consequently, increase the ground state population and decrease the concentrations of radicals. This change in concentrations can be detected optically, as discussed in the next section.

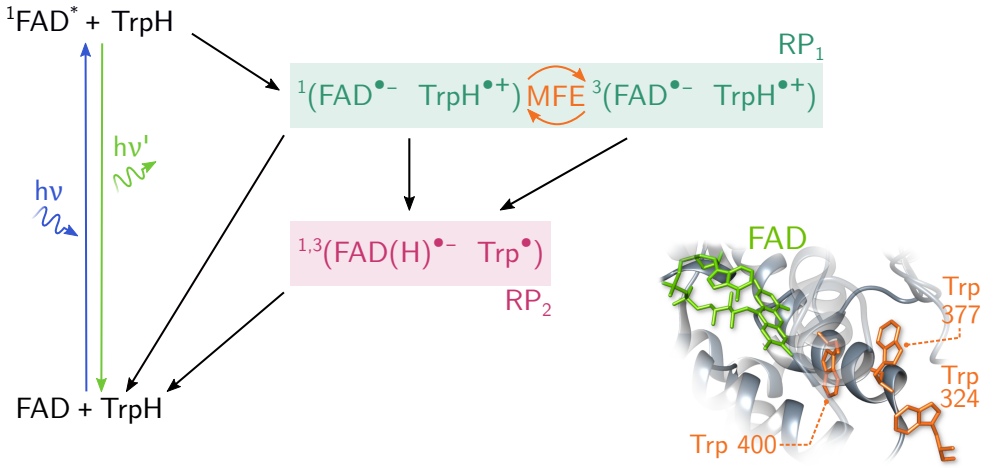


Figure 7: Photoscheme of the radical pair mechanism for the formation of intramolecular RPs in cryptochromes. The radical pair is formed in the singlet state following a cascade of electron transfers along a triad or tetrad of tryptophan residues and undergoes singlet-triplet mixing. Although only the singlet state may recombine directly to the ground state, a second longer-lived radical pair may be formed by protonation or deprotonation of either one or both radicals. The inset depicts the flavin cofactor and tryptophan residues in the cryptochrome from the plant *Arabidopsis thaliana* and is drawn from PDB entry 1U3D using Chimera.[27,28]

MFEs in intermolecular model systems

The most thoroughly investigated cryptochrome model system consists of FMN and hen egg-white lysozyme (HEWL), which is a small protein containing solvent-exposed tryptophans. It is ideal for proof-of-principle studies as it is readily available and has been shown to contain a flavin-tryptophan radical pair.[29] Additionally, owing to the slow diffusion of the protein and the attractive Coulomb interaction between the flavin and the lysozyme protein (see Chapter 4 for details), the FMN-HEWL radical pair exhibits relatively large MFEs compared to other intermolecular model systems and is, therefore, well suited for methodology development.[30]

The photocycle of FMN-HEWL, and that of other intermolecular radical pairs in gene-

ral, is similar to that of cryptochromes but exhibits some crucial differences due to its intermolecular nature. In this case, as shown in Figure 8, intersystem crossing to ^{3}FMN is faster than the electron transfer and immediately follows photoexcitation. Subsequent intermolecular electron transfer from tryptophan residues Trp 62 or Trp 123 on HEWL to the flavin cofactor creates the triplet-born radical pair ^{3}[FMNH$^\bullet$ TrpH$^{\bullet+}$].[29] This triplet RP first has to undergo coherent triplet-singlet interconversion before recombining to the ground state via geminate recombination within the solvent cage. However, both radical pair spin states can diffuse apart and escape the solvent cage. The resulting free radicals may then encounter other radicals and form freely diffusing RPs or F-pairs, in which spin correlation may be re-established by action of the exchange interaction.

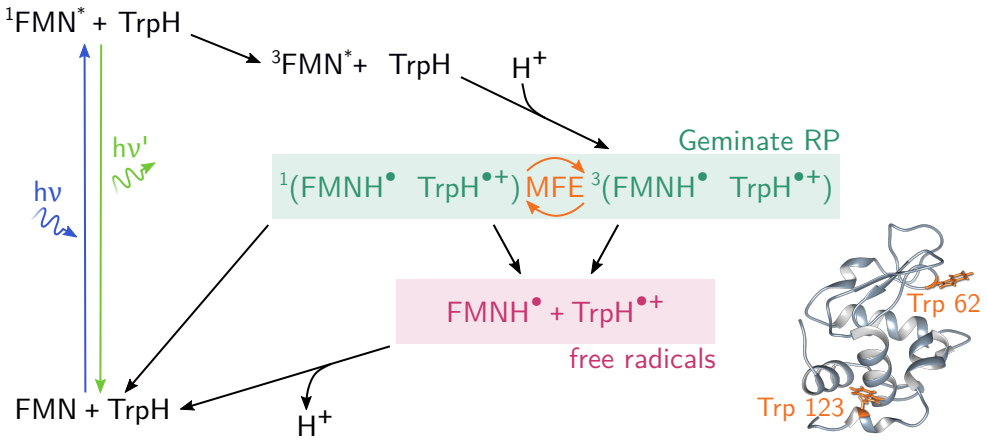


Figure 8: Photoscheme of the radical pair mechanism for the formation of intermolecular RPs in FMN-HEWL. Following photoexcitation, intersystem crossing is faster than the electron transfer and the radical pair is formed in the triplet state. Depending on the spin state of the radical pair, the two radicals can either recombine or diffuse apart and form free radicals. The inset shows the structure of HEWL and highlights the tryptophan residues participating in the reaction. It is drawn from PDB entry 1DPX using Chimera.[27,31] The protonation states of the radicals correspond to the case of pH=4.2, as in Chapter 4.[32,33]

As in cryptochromes, large magnetic fields hinder spin mixing but, in the case of a triplet-born radical pair, this results in a decrease in the ground state population and an increase in the free radicals concentrations. Thus, the magnetosensitivity of *intra*molecular radical pair in cryptochrome and the *inter*molecular radical pair in FMN-HEWL exhibit opposite trends.

The key similarities and differences between the FMN-HEWL model system and cryptochromes are listed in Table 1.

	FMN-HEWL	Cryptochrome
Flavin	FMN	FAD
Counter radical	Solvent-exposed tryptophan residues, most likely Trp 62 and Trp 123.[29]	The distal tryptophan of a triad or tetrad of tryptophan residues.[25]
Electron transfer	Intermolecular (slower than intersystem crossing)	Intramolecular (faster than intersystem crossing)
Initial RP	Triplet-born	Singlet-born
Spin-decoherence pathways	Modulation of anisotropic interactions due to molecular tumbling.	Modulation of the exchange interaction due to electron hopping in the tryptophan chain.[34]

Table 1: Comparison of the main properties of the radical pairs formed in FMN-HEWL and crypotochromes.

0.4 Optical detection of magnetic field effects

The resulting changes in the concentrations of the ground state and radicals due to a magnetic field is referred to as a magnetic field effect and can be monitored by optical techniques.[35]

0.4.1 Absorption-based techniques

Traditionally, MFEs have been investigated by absorption spectroscopy, which consists in passing light through a sample and comparing the incident light, I_0, to the transmitted light, I.[26,36–38] All chemical compounds absorb light in a specific wavelength range which is characteristic of the sample. The absorbance of a species, which corresponds to the quantity of light absorbed, is related to I_0 and I by the Beer-Lambert law:

$$A = -\log_{10} \frac{I}{I_0} = \epsilon \cdot l \cdot c, \tag{32}$$

where l is the path length of the light through the sample, ϵ is the molar absorption coefficient of the sample and c is the concentration.

Thus, absorption-based techniques allow to identify the species present in the sample and monitor their concentrations as each of them has a unique spectral signature. Further, temporal information can also be obtained by using time-resolved spectroscopies such as transient absorption (TA). TA is a pump-probe experiment in which two short pulses are sent to the sample one after the other. The first pulse, the pump, excites the sample and creates populations of transient species, which are then analysed by a weaker probe beam. The delay time between the pump and the probe can be varied, thus providing temporal resolution. The transient absorption, ΔA, can then be monitored as a function of pump-probe delay time and is given by:

$$\Delta A(\lambda, t) = A_p(\lambda, t) - A_{np}(\lambda, t), \tag{33}$$

where A_p and A_{np} are the absorbances of the excited sample (pumped) and of the sample in the ground state (not pumped), respectively. ΔA contains information on the dynamic processes that occur in the excited state and is, therefore, extremely relevant for the study of radical pair reactions. In general, transient absorption spectra contain contributions from various processes: the depletion of the ground-state (or ground-state bleach), stimulated emission, and absorbance of the transient species formed. The first two processes give rise to negative signals while the latter is positive (see Figure 9). Further, the effect of an applied magnetic field can be determined by measuring $\Delta\Delta A = \Delta A(t, B_0 \neq 0) - \Delta A(t, B_0 = 0)$, or the percentage MFE, $\%\text{MFE} = \Delta\Delta A / \Delta A(t, B_0 = 0)$.

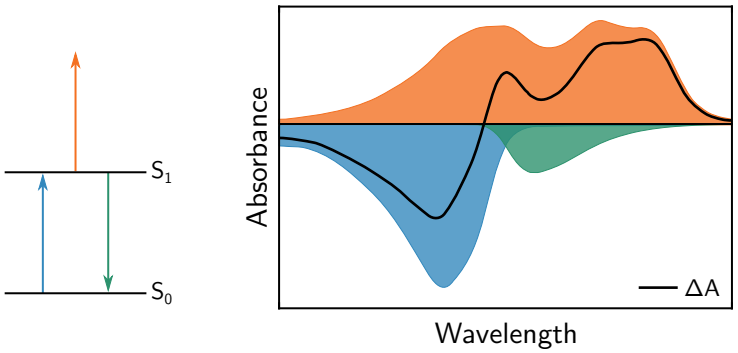


Figure 9: Example of a transient absorption spectrum. The different contributions of the ground state bleach (blue), stimulated emission (green) and absorption of transient species (orange) are highlighted.

This technique is very powerful for elucidating reaction mechanisms, but lacks sensitivity and can be difficult to interpret when different species absorb in the same region.

Other absorption-based techniques, such as cavity ring-down spectroscopy (CRDS), use optical cavities to increase the sensitivity by passing light through the sample multiple times, therefore significantly increasing the pathlength. Briefly, the probe light enters a cavity comprised of two highly reflective mirrors and is reflected back and forth. Every time the light is reflected by the rear mirror, a small fraction leaks out of the cavity onto a detector where it is recorded. Its attenuation over time can be expressed as an exponential decay, whose time constant is termed the ring-down time and can be used to extract time-resolved information on the absorption of the sample, as follows:

$$\ln(10)\Delta A = \frac{\tau_0 - \tau}{\tau_0 \tau}\left(\frac{L}{c}\right), \tag{34}$$

where τ and τ_0 are the ring-down times recorded with and without photoexcitation, respectively, L is the length of the cavity and c is the speed of light.[38]

0.4.2 Fluorescence-based techniques

Although cavity-based methods have been shown to improve significantly the detection sensitivity, they are highly sensitive to scattering. This has driven the development of fluorescence-based techniques for the measurement of MFEs.[39]

After formation of the flavin singlet excited state, the latter can relax back to the ground state by fluorescing. MFEs can be indirectly recorded by monitoring the fluorescence intensity under conditions of continuous photoexcitation. In this case, upon re-excitation, the magnetosensitivity carried by the ground state population is transferred to the singlet excited state and, in turn, to the fluorescence. The effect of the magnetic field on the fluorescence intensity I_f is given by:

$$\%\text{MFE} = \frac{I_f(B_0 \neq 0) - I_f(B_0 = 0)}{I_f(B_0 = 0)} = \frac{\Delta I_f}{I_f(B_0 = 0)}. \tag{35}$$

Fluorescence-based experiments have been proven to exhibit exceptional sensitivity and are of significant interest for exploring systems of low optical quality. As the fluorescence of a chromophore is shifted to the red compared to its absorption spectrum, the former can therefore be detected without collecting any residual scattered light from the excitation beam. Further, in most cases, the flavin singlet excited state is the only fluorescing species involved in the reaction, which makes the interpretation of the data significantly more

straightforward than with absorption-based techniques.

However, as steady-state conditions have to be employed, no time-resolved information can be accessed by fluorescence. Additionally, as the fluorescence quantum yield of cryptochromes is extremely small due to the competition with the electron transfer, the detection of their MFEs by fluorescence is extremely challenging.

Thus, absorption- and fluorescence-based MFEs detection methods are complementary and should be used in tandem to fully analyse and understand the magnetosensitivity of the different systems under investigation.

0.4.3 MARY curves

MFEs are usually measured as a function of the applied magnetic field strength and are presented as a magnetically altered reaction yield (MARY) curve. This representation provides a tool to compare the magnetic behaviours of different systems examined by different techniques. A schematic MARY curve for a triplet-born radical pair measured by fluorescence is shown in Figure 10. At low field, additional spin mixing pathways are allowed which, based on the photoscheme in Figure 8, increases the singlet yield, giving rise to a positive MFE. As the field increases, the Zeeman interaction becomes dominant and inhibits interconversion between the spin states, yielding a negative MFE.

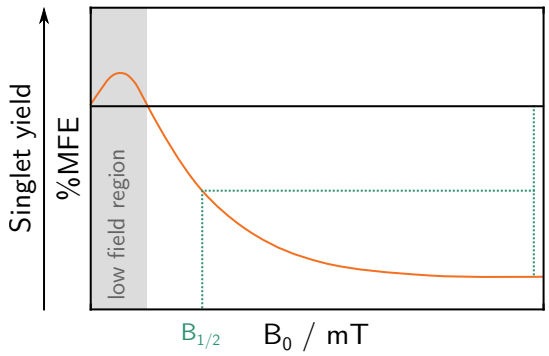


Figure 10: Illustration of a MARY curve measured by fluorescence for a triplet-born radical pair. The width of the curve is characterised by the $B_{1/2}$-value.

The magnitude and shape of a MARY curve are characteristic of the spin dynamics of the system. They are quantified by the position and magnitude of the LFE as well as the $B_{1/2}$-value, which is defined as the field at which the MFE reaches half of its saturation value.

Note that, as mentioned in the previous section, the nature of the radical pair investigated dictates its response to the field. For singlet/triplet-born radical pairs, an increase in the magnitude of the field gives rise to a decrease/increase in the radical concentrations as well as a corresponding increase/decrease in the ground state concentration. Additionally, for a given radical pair, the sign of the measured MARY curve ultimately depends on the species probed by the detection method employed. While fluorescence-based techniques are mostly sensitive to the evolution of the oxidised flavin's concentration (see Chapter 5 for a more detailed discussion), absorption-based experiments are able to examine both the radicals and the ground state flavin. For clarity, Table 2 summarises the different cases encountered in this work.

Detection method	Singlet-born RP	Triplet-born RP
Absorbance (radicals)	$\ominus$	$\oplus$
Absorbance (ground state)	$\oplus$	$\ominus$
Fluorescence	$\oplus$	$\ominus$

Table 2: Sign of the hyperfine-driven magnetic field effect at high field depending on the nature of the radical pair and the detection method employed.

0.4.4 Enhanced magnetic field effects

A recent work by Kattnig *et al.* demonstrated that the primary magnetic field effect observed in flavin-based systems under continuous photoexcitation could be amplified or attenuated, giving rise to so-called enhanced MFEs (EMFEs).[40] This behaviour has been observed in both intermolecular model systems and cryptochromes. It has been attributed to additional termination reactions that slowly return the two RP partners to their ground states and occur in addition to the recombination of the radicals. Concretely, this phenomenon manifests itself as biphasic kinetics, with a fast component – the prompt MFE – followed by a much slower phase corresponding to the enhancement. The exact nature of the slow component is determined by the relative rates of the removal of the flavin radical, k_F, and the counter radical, k_D. This is illustrated in Figure 11, in which the response of a RP to a single on/off magnetic field step is illustrated for three different scenarios.

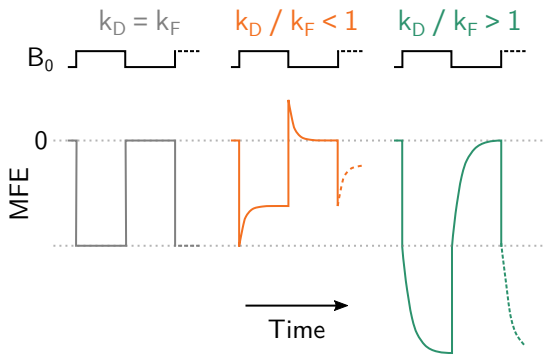


Figure 11: The prompt MFE can be enhanced or attenuated, depending on the ratio k_D/k_F, where k_F and k_D are the rates of the oxidation of the flavin radical and the reduction of its RP partner, respectively. Drawn for the case of a triplet-born radical pair. Adapted from Kattnig *et al.*[40]

Chapter 1

Isotopic labelling of the Radical Pair

Unequivocally demonstrating that animal magnetoreception originates from the reactivity of radical pairs is bound to be a long and complex entreprise. An elegant and direct way to address this question, akin to that proposed by Worster *et al.*, consists in selectively and carefully modifying some of the proteins' magnetic properties *in vivo*, and monitoring the impact on the birds' ability to navigate.[41] Of course, such a method is only relevant if the chosen modifications are specifically targeted at magnetic properties and are not otherwise affecting the cryptochrome's behaviour and its role in signal transduction.

As developed in the Introduction, radical pair based compass behaviour at low field stems from the existence of anisotropic hyperfine interactions. Hence, modifying these hyperfine interactions in cryptochromes would affect the proteins' response to the field. This can be achieved by isotopic enrichment of the radicals as different isotopologues have different gyromagnetic ratios and spin quantum numbers. This approach provides a selective and gentle way to disrupt the operation of the putative radical pair compass sensor and little else. If cryptochromes are indeed the magnetic sensors at the heart of animal magnetoreception, isotopic substitution of either of the radicals *in vivo* is expected to alter the birds' ability to navigate.

At first sight, the practical execution of such an experiment may seem overly complicated and unrealistic. However, Nature itself offers a way to generate birds with different FAD isotopologues. Indeed, animals are not able synthetise flavins and rely on the riboflavin in their diet as the sole source of all flavin derivatives so birds could, in principle, be fed isotopically labelled flavins.[42] This idea, which was briefly mentioned by Brocklehurst in an excellent review dedicated to magnetic isotope effects, would allow to compare the migratory behaviour of these birds to that of birds with a normal diet, and has the potential to unambiguously elucidate the origin of avian magnetoreception.[43]

The most promising element for this purpose is carbon as ^{12}C, whose natural abundance is 98.8%, has no nuclear spin whereas ^{13}C has a spin-1/2 and may give rise to

sizeable additional hyperfine interactions. In principle, nitrogen and hydrogen could also be considered. Indeed, both of the naturally occurring nitrogen isotopes are magnetic but have different spin quantum numbers ($I = 1$ for ^{14}N and $I = 1/2$ for ^{15}N). However, because the gyromagnetic ratios of ^{14}N and ^{15}N are very similar ($\left|\gamma(^{15}\mathrm{N})/\gamma(^{14}\mathrm{N})\right| = 1.4$[44]), the impact of nitrogen isotopic substitution on the hyperfine interaction is expected to be relatively small. Conversely, MFEs have been shown to be markedly affected by deuterium enrichment as the gyromagnetic ratios of hydrogen and deuterium are significantly different ($\left|\gamma(^{1}\mathrm{H})/\gamma(^{2}\mathrm{H})\right| = 6.5$[44]).[14,45] Consequently, the hyperfine interactions are expected to be smaller in the case of deuteration. However, in the case of a flavin radical, the largest and most anisotropic hyperfine couplings are those of the nitrogen atoms (see below), which would be left undisturbed by the deuterium enrichment, rendering this isotopic labelling ineffective.

The hyperfine couplings of a flavin with the side chain truncated after the first carbon were calculated by DFT and are listed in the Appendix. For each magnetic nucleus, the isotropic hyperfine coupling is defined by $a_{\mathrm{iso}} = (a_X + a_Y + a_Z)/3$, where $a_{X,Y,Z}$ are the principal values of the hyperfine tensor. The anisotropic component of the tensor is given by $a_{\mathrm{aniso}} = |a_k - a_{\mathrm{iso}}|$, in which k is the primary direction of the hyperfine tensor that maximises a_{aniso}.[46,47] The isotropic and anisotropic components of the hyperfine couplings of the isotopologues considered are depicted in Figure 1.1. Qualitatively, isotopologues exhibiting many strong isotropic and anisotropic hyperfine couplings are more likely to induce significant changes in the magnetic sensitivity of the radical pair. Based on Figure 1.1, ^{13}C-enrichment obviously increases the amount of magnetic nuclei in the molecule. Most importantly, as clearly seen in Figure 1.2, it yields large hyperfine couplings with highly anisotropic tensors (for C6 and C8, in particular). Thus, the effect of ^{13}C-enrichment on the RP spin dynamics could be manifold as it might impact the frequency of singlet-triplet mixing as well as spin decoherence processes.

Before implementing such a complex and large-scale zoological experiment, preliminary *in vitro* tests are crucial to assess the chances of success of the *in vivo* experiment. As FAD isotopologues have yet to be successfully incorporated into cryptochromes, these proof-of-principle studies were conducted on model systems. The aim is to characterise the impact of isotopic substitution on flavin-based magnetic field effects. The low-field region is, of course, of particular interest in order to mimic as well as possible the geomagnetic field involved in the real-scale *in vivo* experiment.

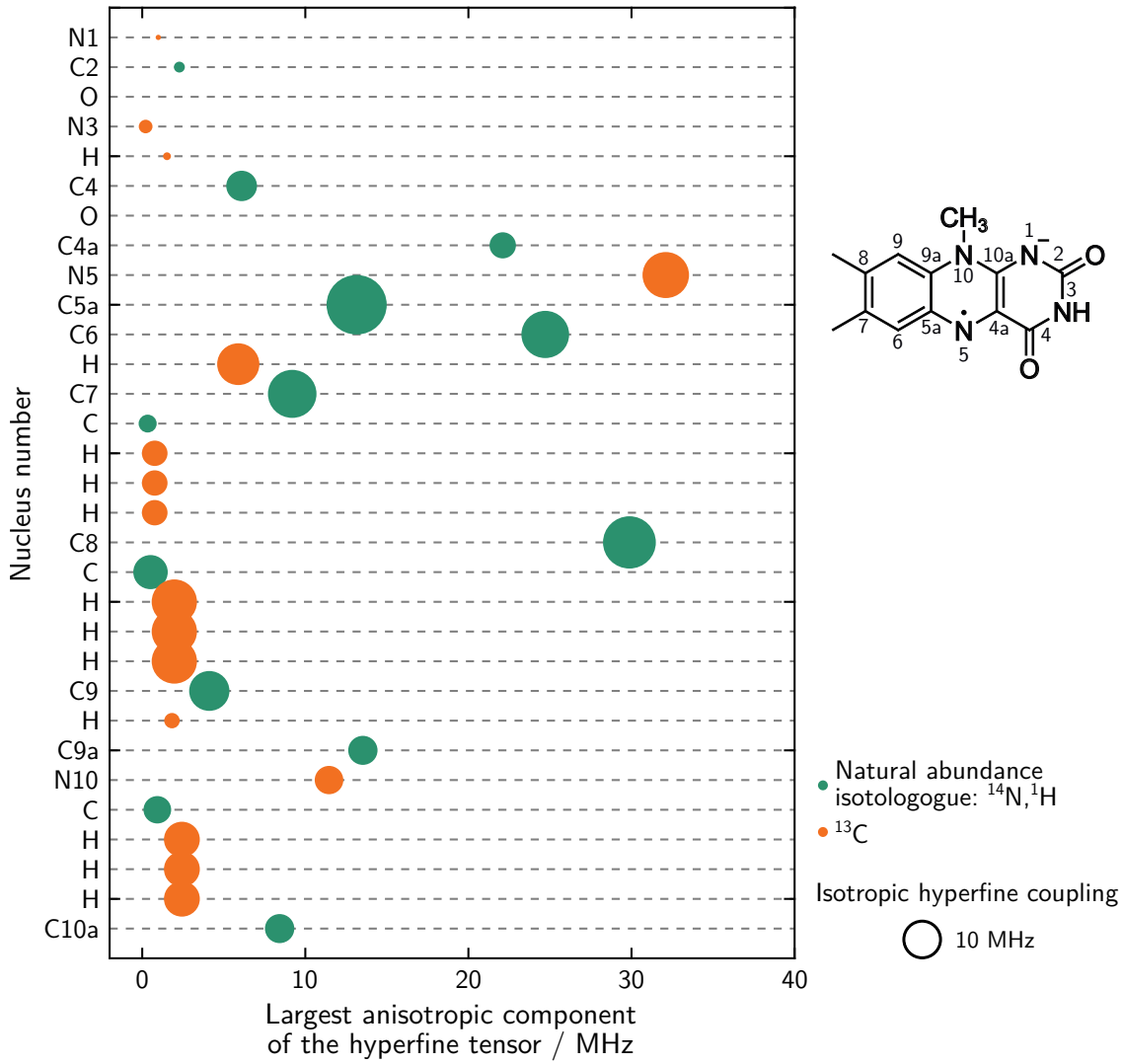
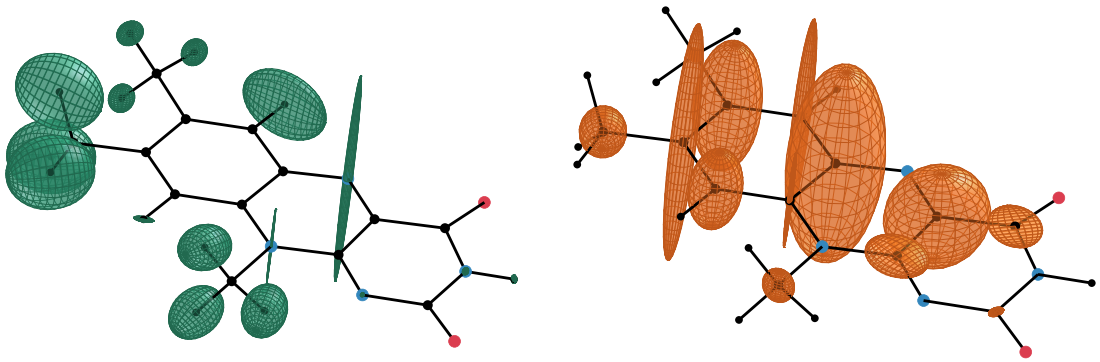


Figure 1.1: Comparison of the isotropic and anisotropic hyperfine couplings of different isotopologues of a flavin anion radical. The hyperfine tensors, which are listed in the Appendix, were calculated using Orca at the B3LYP/EPR II level of theory for a flavin radical with a ribityl side chain truncated after the first carbon.[48] The atom numbering scheme used is shown in the top-right corner.

Although LFEs are well-documented in systems forming exciplexes in organic solvents and in the carotenoid-porphyrin-fullerene triad compass, evidence of chemical reactions sensitive to magnetic fields of the order of a few Gauss or lower in aqueous environments is much rarer.[14,45] Only a few systems have been shown to exhibit LFEs in these conditions. Relatively small LFEs were first reported in a plant cryptochrome and closely-related *E. coli* photolyase by Maeda *et al.*[34] A couple of years later, Beardmore and co-workers measured a LFE on the intramolecular reaction of FAD at low pH.[49] It was only in 2016 that the first intermolecular LFE in aqueous solutions was detected in FMN and ascorbic



(a) Natural abundance isotopologue (^{1}H,^{14}N). (b) Effect of ^{13}C-enrichment.

Figure 1.2: Visualisation of the calculated (B3LYP/EPRII) hyperfine couplings of different flavin isotopologues.

acid by Kattnig *et al.*[40] This system exhibits a relatively strong LFE (∼15 % relative to the high-field effect) which was the focus of a subsequent paper.[50] However, most importantly, to date, flavin-tryptophan intermolecular radical pairs have never be shown to exhibit a LFE.

1.1 Fluorescence-detection of magnetic field effects

The changes in the size and shape of a LFE resulting from isotopic substitution are expected to be relatively small and a very sensitive technique is, therefore, required for their detection. Fluorescence spectroscopy is particularly sensitive but, until recently, it was restricted to the measurement of MFE via the delayed fluorescence of products formed from RPs in aromatic hydrocarbons or systems forming exciplexes.[45,51] Evans *et al.* introduced the prompt fluorescence magnetically altered reaction yield (PF MARY) experiment which, as the name suggests, is based on the measurement of the magnetosensitive prompt fluorescence of the flavin excited state and has proven to be very suitable for the measurement of MFEs in model systems, including LFEs in FMN-ascorbic acid.[39,50]

1.1.1 Low-volume PF MARY

The general operation of PF MARY is depicted in Figure 1.3. As discussed in the Introduction, the sample is illuminated continuously in order for the fluorescence to carry the magnetic sensitivity developed during spin-mixing. In parallel, the magnetic field is switched on and off alternately. To ensure that the field reaches its desired value for each

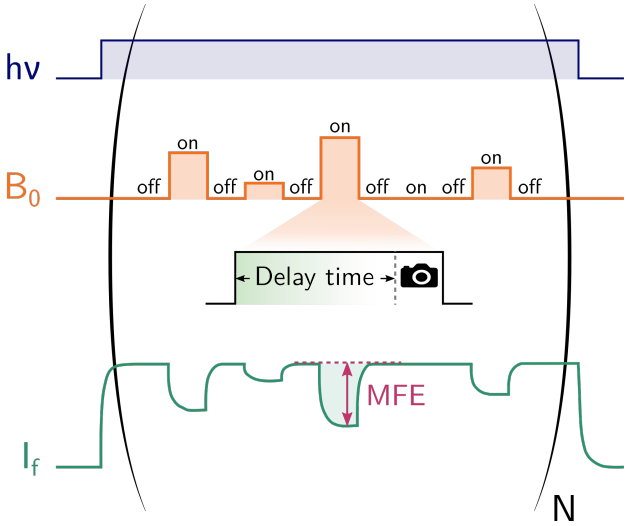


Figure 1.3: Principle of magnetic field-synchronised fluorescence measurements. Following blue-light illumination, the sample's fluorescence intensity is modulated by an applied magnetic field. Here, the case of a triplet-born radical pair is depicted: the fluorescence decreases when the field increases. A delay time is introduced between switching the field and recording the fluorescence to allow the field to reach its desired value. The magnetic field is stepped between 0 and 20 mT in random order. For each field value, N fluorescence measurements are averaged. The MFE is defined as the fractional field-induced change in the fluorescence intensity with respect to the adjacent field-off fluorescence measurements.

measurement, a delay time between setting the magnetic field and recording the sample fluorescence was introduced.

Original experimental apparatus

The original experimental arrangement of PF MARY is detailed in a publication by Evans *et al.*[39] Briefly, using a syringe pump, samples were flowed through a sample cell so as to minimise photodegradation. The sample cell was held by a pair of Helmholtz coils generating static magnetic fields of up to 12 mT with a rise time of ~ 15 ms. A continuous wave diode laser was used to photoexcite the sample and the response of the system's fluorescence was measured with the applied magnetic field switching alternately on and off. The fluorescence was focussed by an achromatic doublet pair onto an optical fibre coupled to a spectrograph and a charge-coupled device (CCD) camera. The collection efficiency of the fluorescence was marginally improved using a concave mirror at the rear of the optical cell. A long-pass filter was employed to block the scattered light coming from the diode laser. All studies were conducted at room temperature with 300 averages at each field point in a random order.

Improvement to the apparatus

Flavin isotopologues are not available commercially and can only be obtained in limited amount from Prof. Schleicher's lab in Freiburg, Germany. Thus, although the original PF MARY experiment produced data of excellent quality, several improvements were necessary in order to study such precious samples. For this purpose, the experiment was entirely deconstructed and rebuilt after each of its components had been carefully assessed and optimised. The new experimental apparatus is presented in Figure 1.4.

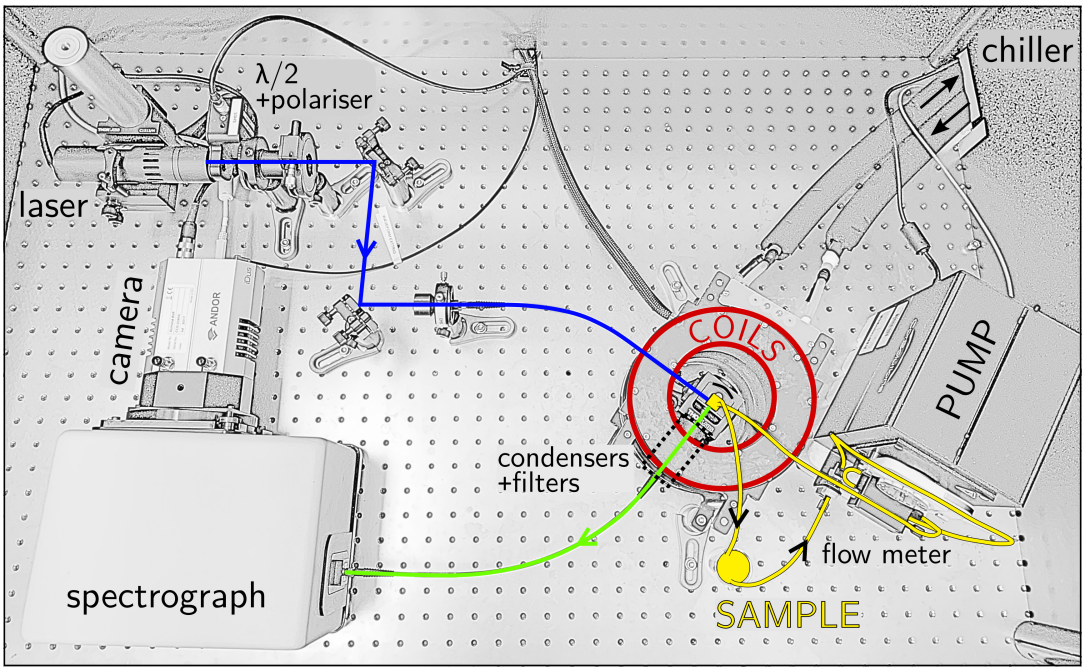


Figure 1.4: Apparatus of the re-designed PF MARY experiment, see details in the main text.

Optical system The general concept of the experiment was kept essentially the same but its collection efficiency was improved by modifying the sample holder and the coils. Previously, as the coils were also serving as sample holder, the doublet pair could not be placed close enough to the sample. Hence, the solid angle of detection was quite narrow and could only detect less than 3% of the emitted fluorescence. To alleviate this problem, new coils were designed. As they were larger, their rise time was longer (∼55 ms), but it allowed a cuvette holder (Thorlabs, CVH100) to be placed at their centre. This new feature makes possible the use of a variety of cuvettes such as temperature-controlled cuvettes which find application in the study of biological samples for instance. For normal operation of the experiment, the cuvette used is a flow cell (Hellma analytics, QS 176-751-

85-40). The fluorescence is then detected via a pair of carefully selected and positioned condensers of appropriate focal length (ACL12708U-A,Thorlabs) mounted in a lens tube. With this configuration, the first condenser is fully against the cuvette, which brings the collection efficiency to 20%. As before, a concave mirror was placed at the rear of the cuvette to further increase the collection efficiency. The second condenser focuses the light into a fibre coupled to a new high-throughput spectrograph (Holospec, Andor) and a CCD camera (iDus DU420A-BVF, Andor). Finally, a half-wave plate and a polariser were positioned after the laser in order to accurately control the excitation power. In some cases, a neutral density filter had to be introduced between the condensers to attenuate the fluorescence and prevent the saturation of the camera.

Flow system Flavins solutions are extremely susceptible to photodegradation and need to be flowed so as to minimise this phenomenon. The original experiment was mainly dedicated to the study of inexpensive model systems which are available in large quantities and can be flowed to waste, either with a syringe pump or by gravity. Hence, for each experiment, several tens of milliliters of sample were flowed and the dead volume of the flow system was quite large ($\sim$7 mL). Given the quantities of isotopologues accessible, much smaller volumes had to be used.

Several flow systems and pumps were tested and the best results (*i.e.* a smooth and stable flow) were obtained with a modified PeriWave peristaltic pump (CorSolutions). The dead volume of the pump (initially $\sim$2 mL) was halved by shortening the dampening tubing and removing non essential downstream tubings. The final dead volume of the overall flow system is $\sim$1.75 mL.

Peristaltic pumps are, by nature, introducing pulsations in the fluid flow and, in turn, in the fluorescence background. As the new optical system made the experiment particularly sensitive, the resulting short-frequency pulses in the fluorescence intensity can give rise to artefacts on the MFE. To mitigate the impact of the flow system on the signal, the pump-induced pulsations were smoothed by connecting the pump to the sample cell via a soft-walled PVC tubing (internal diameter 1.14 mm).

Gas bubbles are an unfortunate and sadly common occurence in all flow systems. They are such an inconvenience that entire reviews are dedicated to them (see, for instance, the excellent work of Pereiro and co-authors[52]). Briefly, in the specific case of the PF MARY

experiment, the problem was mostly circumvented by sonicating non-protein samples for a few minutes prior to the experiment in order to remove most of the microscopic bubbles present in the solution and by filling the flow system very slowly so as to minimise air pockets.

Program The program controlling the experiment was entirely re-written in LabView in collaboration with Dr Marcin Konowalczyk. A digital delay generator was included to allow optimal control of the delay time. Additionally to allowing the field to reach its desired value, the delay time also plays a crucial role in the resulting magnitude of the detected MFE. As Kattnig *et al.* demonstrated, the initial MFE can be amplified or attenuated over time due to slow recombination reactions of the radical pair partners, hence giving rise to enhanced MFEs.[40] An extremely accurate control of the delay time is therefore necessary for the experiment to be reliable.

Assessment of the performance of the new design Unfortunately, a direct and quantitative comparison of the performances of the original and new PF MARY setups is not possible due to several reasons listed below:

- Difference in field coils. As the new coils are larger, their rise time is longer than that of the previous set of coils and cannot be lowered to the values employed previously. In FMN-HEWL, when the field has reached its full magnitude, larger delay times lead to an increase in the MFE.[40]

- Difference in excitation light. The original apparatus comprised a 350 mW 405 nm laser. In the new setup, a 450 nm laser (Power Technology, 450 nm, 70 mW) is employed and the excitation power is usually attenuated to 15 mW . Although the difference in excitation wavelength is unlikely to have a significant impact, larger excitation powers are known to give rise to significantly larger MFEs. For instance, increasing the laser power from 15 mW to 350 mW has been reported to increase the absolute magnitude of the MFE by a factor of 15 for a solution of 10 μM FMN and 0.4 mM HEWL.[53]

However, a more qualitative comparison is possible. FMN-HEWL is a system that is typically used as a standard for PF MARY experiments. Figure 1.5 shows a typical MARY

curve recorded using the new apparatus with an excitation power of 10 mW, 50 averages and 8 mL of an FMN-HEWL solution. In order to obtain data of such quality with the previous experimental setup, at least 50 mL of sample needed to be excited at 350 mW and 300 averages were required, which is a testament to the quality of the re-designed experimental apparatus.

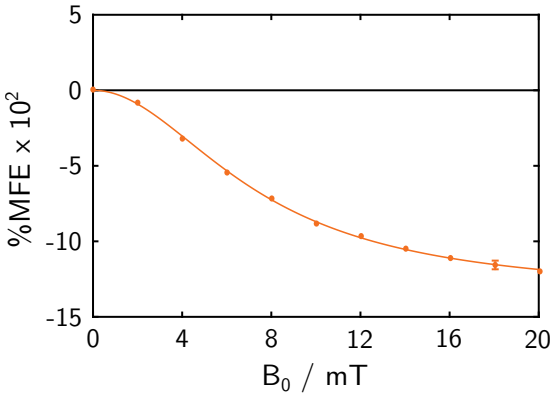


Figure 1.5: MARY curve of a solution of 10 μM FMN and 0.5 mM HEWL measured with the new PF MARY apparatus. A representative error bar is depicted at B_0=18 mT.

1.2 Effect of ^{13}C isotopic substitution on MFEs

As discussed above, based on Figure 1.1, substituting all the carbon atoms with ^{13}C would dramatically change the hyperfine couplings of the flavin radical and is, therefore, expected to strongly affect the interaction of the radical pair with an applied magnetic field. A considerable number of chemical reactions have been shown to exhibit magnetic isotope effects and their connection to MFEs was detailed by Brocklehurst.[43,45,54–57] Yet, much less is known about their impact on flavin-containing systems and low field effects. Hence, before moving to the study of the flavin-tryptophan radical pair of interest, it is worth investigating and understanding how isotopic substitutions affect LFEs in a flavin-based system whose LFE is well characterised first.

1.2.1 Isotopic enrichment of FMN-ascorbic acid

Methods

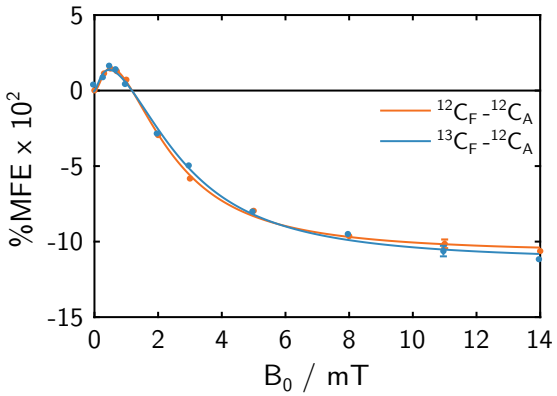
Materials Solutions of 10 μM FMN and 500 μM ascorbic acid were prepared in ultrapure water. The ^{12}C isotopologues were obtained from Sigma Aldrich and used without further purification. ^{13}C-ascorbic acid, in which all the carbon atoms are substituted with ^{13}C, was purchased from Omicron Biochemicals, Inc. ^{13}C-FMN, in which all the carbons are ^{13}C, was kindly donated by Prof. Erik Schleicher (University of Freiburg, Germany). UV-vis spectroscopy was used to confirm that the flavin concentration was the same in all the isotopomer combinations.

Magnetic field effects MFE measurements were carried out using the improved PF MARY apparatus described in the previous section. As the magnetosensitivity of the system under investigation is quite low compared to other model systems, it requires a more powerful excitation. Consequently, the laser usually employed in the experiment was replaced by a 405 nm laser operating at 175 mW. To further increase the signal-to-noise, the delay time was lengthened and set to 180 ms. The MARY curve was averaged over 100 field cycles.

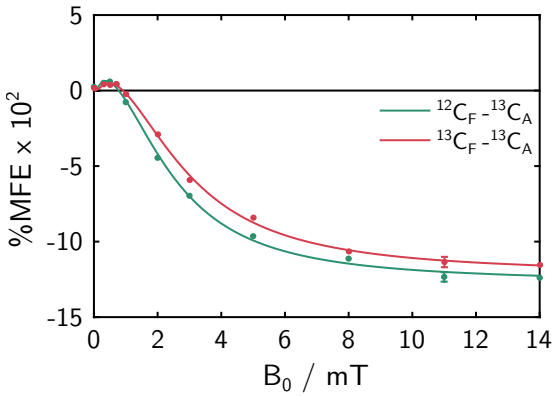
Results and discussion

The MARY curves of the four FMN-ascorbic acid pairs of isotopomers are presented in Figure 1.6. For clarity, and in order to highlight the effect of a single substitution on the field effect, the four curves are presented two by two. Note that, for brevity, the labels of the different isotopomers have been shortened. From now on, the four combinations will be referred to by their isotopic composition, with that of the flavin radical first. Thus, $^{13}C_F$-$^{12}C_A$ corresponds to the radical pair [^{13}C-FMN$^{\bullet-}$ ^{12}C-Asc$^{\bullet-}$].

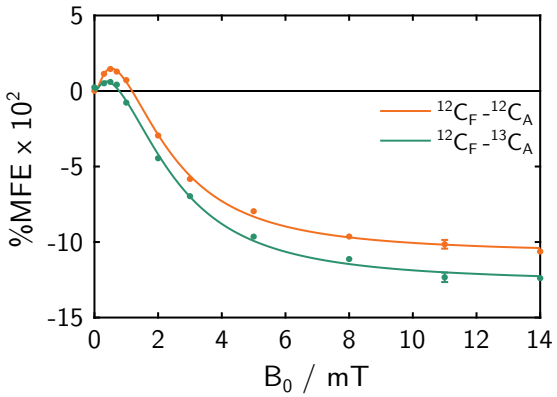
The four curves have broadly similar features: they all exhibit a low-field effect and have a negative MFE at high-field, which is characteristic of a triplet-born radical pair (see Introduction) and is consistent with previous work.[50] It is also clear that the four combinations of isotopologues exhibit different magnetosensitivities, showing that the field effect is indeed strongly dependent on the hyperfine couplings of the system.



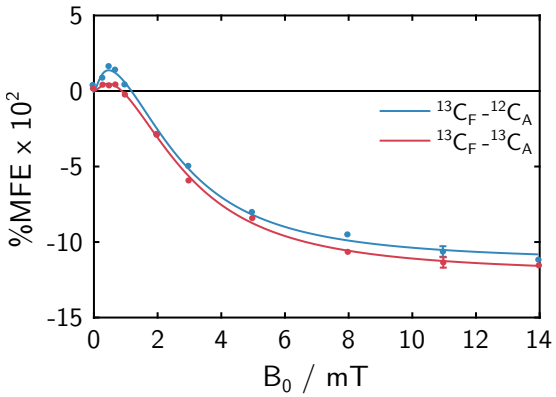
(a) Effect of ^{13}C enrichment of the flavin radical on the MFE of FMN/^{12}C-ascorbic acid



(b) Effect of ^{13}C enrichment of the flavin radical on the MFE of FMN/^{13}C-ascorbic acid



(c) Effect of ^{13}C enrichment of ascorbyl radical on the MFE of ^{12}C-FMN/ascorbic acid



(d) Effect of ^{13}C enrichment of ascorbyl radical on the MFE of ^{13}C-FMN/ascorbic acid

Figure 1.6: MFE on the reaction of the [FMN$^{\bullet-}$ Asc $^{\bullet-}$] radical pair for four combinations of isotopomers. For brevity, the labels of the isotopologues have been shortened and only indicate the isotopic nature of the radicals, with the flavin radical mentioned first, followed by the ascorbyl radical. A representative error bar is displayed at B_0=11 mT. The lines are multi-Lorentzian fits to the data.

Regarding the original aim of this chapter, the experiment that is the most relevant to identify whether ^{13}C-enrichment of the flavin could be used to alter a bird's magnetoreception is presented Figure 1.6a. Unfortunately, in the case of the FMN-ascorbic acid system, it seems that substituting all carbons with ^{13}C in the flavin has close to no effect on the magnetosensitivity of the RP. Within error (representative error bars are depicted at B_0=11 mT), the MARY curves of $^{12}C_F$-$^{12}C_A$ and $^{13}C_F$-$^{12}C_A$ are essentially identical. Interestingly, it seems that it is the isotopic nature of the ascorbyl radical that has the largest impact on the overall shape of the MARY curve. This is particularly visible in the low-field region where interchanging the ascorbic acid isotopologues dramatically affects

the amplitude of the LFE. To facilitate a more quantitative assessment of the LFE and the shape of the MARY curve, it is common practice to parametrise the latter using the following variables (see Introduction):

- $B_{1/2}$, the field at which the MFE reaches half of its saturation value;
- Γ_{LFE}, the depth of the LFE.

In order to properly estimate the values of these parameters, the following function, a sum of two Lorentzians, was fitted to the data:

$$\mathcal{L}_2(B_0) = p_1 \left(\frac{p_2}{B_0^2 + p_2} - 1 \right) - p_3 \left(\frac{p_4}{B_0^2 + p_4} - 1 \right) \tag{1.1}$$

The first Lorentzian mostly describes the high-field region whereas the second aims to replicate the low-field feature. More specifically, p_1 and p_3 determine the saturation value of the field effect at high field; p_2 controls the width of the MARY curve and is, thefore, related to $B_{1/2}$; and p_4 is correlated to the depth of the LFE. The experimental values of Γ_{LFE} and $B_{1/2}$ for the four pairs of isotopologues, which were obtained by fitting the data with Equation 1.1, are listed in Table 1.1.

Radical pair	$^{12}C_F$ - $^{12}C_A$	$^{12}C_F$ - $^{13}C_A$	$^{13}C_F$ - $^{12}C_A$	$^{13}C_F$ - $^{13}C_A$
$\Gamma_{LFE} \times 10^2$	1.49	0.63	1.44	0.48
$a_{FMN^{\bullet-}}$ / mT	1.24	1.24	1.79	1.79
$a_{Asc^{\bullet-}}$ / mT	0.34	0.76	0.34	0.76
$a_{FMN^{\bullet-}}/a_{Asc^{\bullet-}}$	3.64	1.63	5.26	2.35
$B_{1/2}^{exp}$ / mT	2.89 ± 0.41	2.74 ± 0.42	3.18 ± 0.66	3.21 ± 0.44
$B_{1/2}^{theo}$ / mT	2.09	2.11	3.12	2.97

Table 1.1: Empirical and calculated MFE parameters for FMN-ascorbic radical pairs. The hyperfine couplings were obtained by DFT using B3LYP/EPRII in Orca and are listed in the Appendix.[48] $B_{1/2}^{theo}$ was calculated from the hyperfine couplings using Equation 1.2.

The qualitative observations made above based on the plots shown in Figure 1.6 are confirmed by the empirical values of $B_{1/2}$ and Γ_{LFE} obtained from the fitting procedure: radical pairs comprising ^{13}C-enriched ascorbic acid exhibit LFEs that are two to three times smaller than for their ^{12}C counterparts. On the other hand, the isotopic nature of

the flavin radical seems to have a more appreciable impact on the width of the MARY curves. Even though all the experimental $B_{1/2}$-values are quite similar within error, RPs containing ^{13}C-FMN are marginally wider.

Weller and co-workers devised a simple equation to predict the width of the MARY curve based on the hyperfine couplings of the radical pair partners:[58]

$$B_{1/2} = 2\frac{a_1^2 + a_2^2}{a_1 + a_2}. \tag{1.2}$$

The effective hyperfine coupling constant, a_i, for radical i=1,2 is defined as:

$$a_i = \sqrt{\sum_j a_{ij}^2 I_{ij}(I_{ij}+1)} \tag{1.3}$$

where, for each magnetic nucleus j in radical i, a_{ij} and I_{ij} denote the hyperfine coupling constant and nuclear spin quantum number, respectively. The Weller equation is a good approximation when there is little spin dephasing, so for radical pairs of intermediate lifetime.[58] Here, the $B_{1/2}$-values calculated using Equation 1.2, which are also listed in Table 1.1, are in relatively good agreement with the experimental values. The slightly larger $B_{1/2}$-values observed for ^{13}C-FMN stem from the larger hyperfine couplings of the flavin radical when it is enriched in ^{13}C.

In 2007, following initial empirical observations made by Stass *et al.*, who suggested that large LFEs are expected when the hyperfine interactions occur mostly in one of the two radical pair partners, Rodgers and co-workers proposed that a large discrepancy (at least a factor a five) between the hyperfine couplings of the two radical pair partners is required for a substancial LFE to exist.[45,59] The experimental results presented here are in relatively good agreement with this theory as the depth of the LFE appears to be correlated to the relative magnitude of the hyperfine couplings of the radical pair partners. In the case of $^{12}C_F$-$^{12}C_A$ and $^{13}C_F$-$^{12}C_A$, the distribution of the hyperfine couplings is very asymmetric and gives rise to large LFEs. ^{13}C-enrichment of the ascorbyl radical dramatically reduces the difference in hyperfine couplings between the two radicals, therefore reducing the LFE. However, the results presented here demonstrate that Rodgers' hypothesis could be slightly nuanced. While it is true that a large discrepancy between the hyperfine couplings of the two radicals certainly seems to encourage the development of a large low field effect, it appears that the discrepancy between the two hyperfine couplings might not actually need

to be as large as initially thought for the RP to exhibit a significant LFE.

1.2.2 Isotopic enrichment of FMN-HEWL

Methods

Materials Solutions of 10 μM FMN and 500 μM HEWL were prepared in ultrapure water. HEWL and ^{12}C-FMN were obtained from Sigma Aldrich and used without further purification. ^{13}C-FMN, in which all the carbons are ^{13}C, was kindly donated by Prof. Erik Schleicher (University of Freiburg, Germany). UV-vis spectroscopy was used to confirm that the flavin concentration was the same for the two isotopomer combinations.

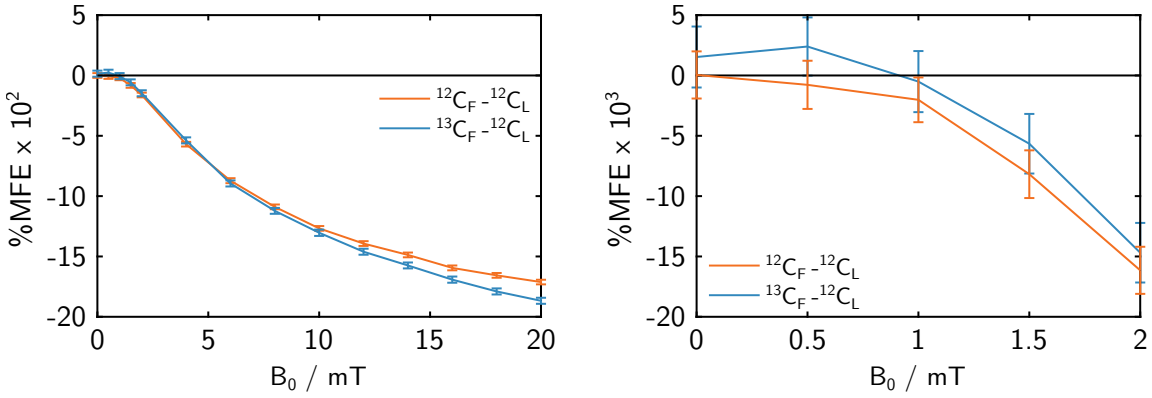
Magnetic field effects MFE measurements were carried out using the PF MARY apparatus described in the previous section. The sample was excited using a 450 nm laser operating at 15 mW. The MARY curve was averaged over 100 field cycles.

Results and discussion

The MARY curves of the two pairs of FMN-HEWL isotopomers are presented in Figure 1.7a. As above, for brevity, the labels of the different isotopomers have been shortened and only mention the isotopic composition of the radicals, with that of the flavin radical first. The low-field region is highlighted in Figure 1.7b.

Qualitatively, it is obvious that the two curves are extremely similar and almost identical within error, in particular in the low-field region. As before, the relevant MFE parameters were extracted using multi-Lorentzian fitting. Their values are reported in Table 1.2.

Interestingly, the $B_{1/2}$-values, both empirical and calculated, are larger than for the FMN-ascorbic acid radical pair, which is consistent with previous findings.[50] This can be partly explained by the much larger effective hyperfine coupling of the counter radical which, based on Equation 1.2, leads to an increase in $B_{1/2}$. However, this reason cannot explain the discrepancy between the experimental and calculated $B_{1/2}$-values. As mentioned above, the Weller formula is particularly relevant for RP of intermediate lifetimes, but it neglects spin dephasing stemming from stochastic modulations of the RP magnetic



(a) Full magnetic field range

(b) Low-field region

Figure 1.7: Effect of ^{13}C-enrichment of the flavin radical on the MFE of FMN-HEWL determined using PF MARY. For brevity, the labels of the isotopologues have been shortened and only indicate the isotopic nature of the radicals, with the flavin radical mentioned first, followed by HEWL.

Radical pair	$^{12}C_F$-$^{12}C_L$	$^{13}C_F$-$^{12}C_L$
$\Gamma_{LFE} \times 10^2$	–	0.15
$a_{FMNH\bullet}$ / mT	1.25	1.69
$a_{Trp\bullet}$ / mT	2.22	2.22
$a_{FMNH\bullet}/a_{Trp\bullet}$	0.54	0.74
$B_{1/2}^{exp}$ / mT	6.39 ± 0.49	7.16 ± 0.54
$B_{1/2}^{theo}$ / mT	3.74	3.98

Table 1.2: Empirical and calculated MFE parameters for FMN-HEWL radical pairs. The hyperfine couplings were obtained by DFT using B3LYP/EPRII in Orca and are listed in the Appendix.[48] $B_{1/2}$ was calculated from the hyperfine couplings using Equation 1.2.

interactions. As highlighted by Maeda *et al.*, spin dephasing is becoming more pronounced with increasing radical pair lifetime and tends to broaden MARY curves.[60] In the case of FMN-HEWL, the attractive Coulomb interaction between the two RP partners, as well as the slowly-diffusing nature of the protein, tend to oppose the diffusive separation of the geminate RP, hence leading to an increased spin dephasing contribution and a broader MARY curve.

Figure 1.7b shows that no clear LFE can be observed for either of the two isotopologues considered. More specifically, the $^{12}C_F$-$^{12}C_L$ curve could not be fitted with anything

else than a single Lorentzian. Technically, a double Lorentzian with a very small LFE component could be used for $^{13}C_F$-$^{12}C_L$. However, a closer examination of the LFE (see Figure 1.8) confirmed that, in spite of the discrepancy between the hyperfine couplings of the two radicals (see Table 1.2), neither isotopologue exhibits a LFE. This can be explained by the fact that both radicals have relatively large hyperfine couplings.

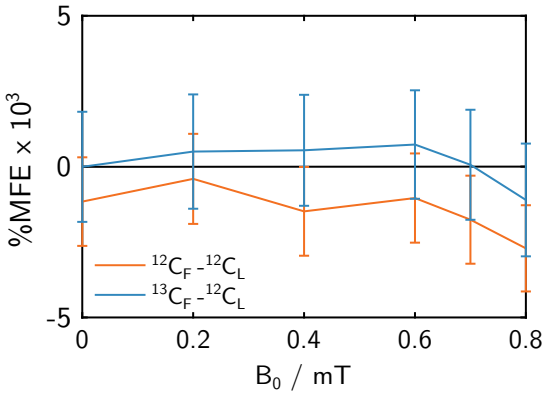


Figure 1.8: Effect of ^{13}C-enrichment of the flavin radical on the LFE of FMN-HEWL determined using PF MARY. For brevity, the labels of the isotopologues have been shortened and only indicate the isotopic nature of the radicals, with the flavin radical mentioned first, followed by HEWL.

1.3 Conclusion and outlook

Buchachenko once described magnetic isotope effects as an 'aristocratic' tool for mechanistic chemistry and it is true that using isotopic enrichment would be an extremely elegant way to unequivocally prove that cryptochromes are indeed at the heart of animal magnetoreception.[54] The preliminary work presented in this chapter, which was facilitated by the technical improvements made on the PF MARY experiment, falls within this larger project and aims to assess the viability of this idea.

A systematic study of the impact of isotopic substitution on flavin-based radical pairs and, more specifically, on their low field effects, was conducted. Using the FMN-ascorbic acid system as a reference, the importance of an asymmetric distribution of the hyperfine couplings of the radical pair partners was highlighted, in agreement with Stass and Rodgers.[45,59] Purposely decreasing this discrepancy between the flavin and ascorbyl radicals by ^{13}C-enrichment of the ascorbyl radical dramatically diminished the LFE amplitude.

Although the potential impact of isotopic subsitution on LFEs was clearly demonstrated by the FMN-ascorbic acid data, the lack of similar results in FMN-HEWL, which is a good

cryptochrome model system, does not allow, at this stage, to acertain the viability of the proposed *in vivo* experiment. Indeed, no LFE could be detected in FMN-HEWL and ^{13}C-enrichment had very little impact on the magnetosensitivity of the system. Given that both radicals exhibit relatively large hyperfine couplings, this gives credence to the hypothesis that LFEs are fostered when the hyperfine interactions occur mostly on one of the radicals.

Owing to their entirely different singlet-triplet dephasing and relaxation pathways, cryptochromes have been shown to exhibit appreciable LFEs which, in principle, could very well be affected by isotopic enrichment.[34] Thus, further proof-of-principle experiments conducted on cryptochromes will most certainly be required once isotopically labelled flavins can be successfully incorporated into the proteins. Further, the behaviour of anisotropic MFEs cannot necessarily be extrapolated from that of isotropic MFEs. Thus, conclusions regarding the impact of isotopic labelling on the isotropic MFEs of cryptochromes will eventually need to be substantiated by studies conducted on anisotropic MFEs. As mentioned above, to date, anisotropic MFEs have never been measured in flavin-based systems. Several strategies for the detection of such effects *in vitro* are explored in the following chapters.

Chapter 2

Encapsulating Flavins in Solid Matrices: Films, Gels and Viscous Solutions

As discussed in Chapter 1, it is clear that additional experiments are required before implementing the proposed *in vivo* experiment aiming to unambiguously establish cryptochromes as the primary magnetic sensor behind the avian compass sense. In particular, the impact of isotopic enrichment on anisotropic magnetic field effects needs to be examined first, which implies that such effects have to be detectable to start with.

So far, anisotropic magnetic field effects in systems subject to the radical pair mechanism have only ever been reported once in an artificial radical pair model system in non-biologically-relevant conditions (*i.e.* non-aqueous solvent and cryogenic temperatures).[14] The absence of similar results for other systems and, in particular, flavin-based radical pairs, is a testament to the experimental challenge that measuring such effects represents. This is due to the fact that anisotropic responses to the field are not only expected to be small but that several conditions also need to be met in order to detect them.[13] If the radical pair partners are randomly oriented within a sample or undergo significant molecular tumbling, the anisotropic components of the magnetic interactions governing the MFE (see Section 0.2.2) will interfere destructively or be averaged out and the overall magnetic field effect detected will be isotropic. On the other hand, anisotropic MFEs can be observed if the radicals have a preferential orientation and maintain it over time (see below for a more detailed discussion). Thus, the radicals, and in particular the flavin, which has the largest anisotropic hyperfine couplings, need to be at least partially ordered and immobilised to be a source of directional information.[47] *In vivo*, it has been suggested that cryptochromes could bind to interaction partners associated with cell membranes.[6] Although membranes are not fully rigid structures, their range of motion is limited and their dynamics are relatively slow compared to the RP spin dynamics. Cryptochromes could, therefore, be organised in an aligned and rigid enough manner for the ordering and motional constraints to be satisfied.[13,61] *In vitro*, cryptochromes are usually studied in relatively non-viscous

aqueous buffers at $\sim 5°C$.[34] Thus, for anisotropic MFEs to be experimentally detected, a method to effectively generate an immobilised and aligned population of radicals in cryptochrome samples must be devised. Evidently, the chosen immobilisation strategy must not impair the integrity nor the spin- and photochemistry of the system under investigation.

In this chapter, a variety of immobilisation strategies are discussed as potential ways to hinder the rotational diffusion of radicals in flavin-based systems for the measurement of anisotropic MFEs. The different media under investigation are first characterised optically to ensure that the flavins' photophysical properties are not altered in this new environment. The degree of immobilisation of the flavin is then assessed by fluorescence anisotropy. Lastly, the suitability of the different immobilisation methods for the measurement of anisotropic MFEs in flavin-containing systems and biologically relevant conditions is discussed.

2.1 Immobilisation strategies

Generally, a population of immobilised and oriented flavin radicals can be generated by two methods:

- photoselection, which uses polarised light to illuminate an immobilised and isotropic sample and preferentially excite molecules aligned along the light polarisation direction;
- direct molecular alignement, which can for instance be achieved using single crystals or liquid crystals.

Although direct molecular alignment seems ideal, it is not very versatile as not all molecules can be crystallised or incorporated into a liquid crystal; and the experimental procedures involved can be quite complex. This immobilisation strategy is extensively discussed in Chapters 4 and 5. The plethora of alternative methods that have been developed over the years to immobilise molecules and proteins are explored in this chapter. Broadly speaking, these techniques fall into three categories:[62]

- Covalent attachment to a support. It is usually quite effective and stable, and may yield oriented immobilisation. However, covalent bonding might affect the tertiary structure of the protein and has been reported to sometimes worsen enzymatic per-

formance. This strategy was, for instance, very recently employed by Zeng *et al.*, who successfully attached cryptochromes to a gold coated slide.[63]

- Adsorption. Although adsorption onto a surface is a gentle method that would preserve the integrity of the system, it only provides a weak bond between the adsorbate and adsorbent and does not constitute a reliable way to keep the proteins on the carrier.

- Physical entrapment. It involves the inclusion of the system within a viscous solution, a polymer network, such as an organic polymer or a silica sol-gel, or a membrane. Assuming the solid matrix used to entrap the system is properly optimised such that the rotational diffusion is sufficiently hindered, this strategy is quite an attractive option, which is why it was explored first.

2.2 Rigid matrices considered for the physical entrapment of flavin-based systems

Over the last few decades, a wide variety of confining environments have been investigated as vehicles to entrap molecules and proteins. Within the scope of this study, all the media taken into consideration have to be aqueous as the aim is to identify a suitable way to immobilise biologically relevant systems, which precludes the use of organic solvents.

Silica sol-gels have been extensively studied and have been successively employed to immobilise enzymes while still allowing them to function normally.[64] They were found to often enhance the thermostability, mechanical resistance, solvent tolerance and storage stability of the entrapped enzymes. Yet, their synthesis can involve harsh conditions which can cause the denaturation of proteins. Further, their pore sizes are highly variable and range from a few nanometers to tens of nanometers. Most importantly, FAD and the flavoprotein glucose oxidase were successively embedded in a sol-gel matrix by Hartnett *et al.*[64] However, even if their rotational mobility was hindered, the rotational correlation time of glucose oxidase in the gel was found to be of the order of tens of nanoseconds. As cryptochromes are smaller than glucose oxidase (molecular weight of $\sim 60\,\mathrm{kDa}$ compared to 80), their rotational correlation time within a sol-gel matrix would likely be smaller than that of glucose oxidase and would, therefore, be too short compared to the timescale of spin-mixing (see Section 2.5). Further, it is worth mentioning that the preparation of

sol-gels involves quite harmful chemicals that many of the spectroscopy labs investigating MFEs are not equipped to handle. For these reasons, sol-gels were not considered further.

Other gels, such as gelatin, methyl cellulose and agarose have also been employed to encapsulate dyes. Gelatin films were for instance used by Rafferty and Clayton to investigate reaction centers and D'Agustino and co-workers estimated the pore size of gelatin gels to be of the order of 10 nm.[65,66] Although fewer studies have considered the use of methyl cellulose as an immobilising medium, Penzer and Radda explored the photochemistry of FMN and FAD in transparent films of methyl cellulose and reported an appreciable decrease in the rotational mobility of the embedded dyes.[67] Recently, Rostas *et al.* demonstrated the ability of an agarose matrix to trap photogenerated FMN radicals.[68] Even though they concluded that, while the translational diffusion of the fluorophore was hindered, its rotational mobility was mostly preserved, it is reasonable to expect that proteins might be affected differently.

Beyond agarose, polysaccharides have been conclusively proven to stabilise proteins and provide means to immobilise them.[69] More specifically, disaccharide glasses containing trehalose and sucrose have been found by Wright, Dashnau and co-workers to be a suitable medium for the incorporation of proteins without dramatically altering their photochemistry.[70,71]

Polymer films provide an additional way of easily immobilising molecules.[72] PVA is especially interesting for this purpose as it is soluble in water and forms a clear film after drying. It has been been extensively employed for the encapsulation of flavin molecules by Drabent, Grajek and co-workers.[73,74]

Finally, beyond gels and films, viscous solutions such as glycerol/water mixtures are also particularly interesting as they are known for their ability to form nicely transparent glasses at low temperatures. Penzer and Radda also reported the significant immobilisation of FMN molecules in aqueous glycerol solutions.[67,71]

The following matrices were, therefore, considered: gelatin, agarose and methyl cellulose gels, sugar glasses, PVA films and aqueous glycerol solutions. In the following sections, their suitability for the measurement of anisotropic MFEs in flavin-containing systems will be assessed based on:

1. whether they provide a suitable environment for proteins (especially regarding tem-

perature as cryptochromes cannot tolerate temperatures above ~ 15°C);

2. their ability to maintain the integrity of the radical pair as well as its photochemical properties;

3. the degree of immobilisation they provide;

4. their ability to exhibit a magnetic field effect.

2.3 Experimental protocols

As the supply of cryptochromes is relatively limited, comparative studies of the ability of the various media mentioned above to efficiently encapsulate flavin-based systems were carried out using FMN. All the chemicals were obtained from Sigma Aldrich and used without further purification. The different samples were prepared as follows, using protocols adapted from the studies mentioned above:

- Gelatin solutions (10% by weight) were obtained by dissolving gelatin powder in ultrapure water under constant stirring at ∼90°C.[65,66] The homogeneous solution obtained was left to cool down to ∼40°C before the flavin was added. It was then immediately poured into a disposable cuvette and was left to set at ∼4°C for about half an hour.

- Agarose gels were prepared in a similar fashion to gelatin gels with a concentration of 3% by weight.[68] However, as agarose tends to clump, the powder was first left to hydrate in water without any stirring for about half an hour. It was then dissolved under vigorous stirring at ∼90°C. Ultra-low gelling temperature agarose was employed such that the flavin could be added at a temperature of 16°C.

- Methyl cellulose samples were obtained by dissolving 0.225 g of powder into 10 mL of ultrapure water.[67] The powder was first dispersed into about half of the water under gentle stirring at ∼90°C. The rest of the water was then added cold together with the flavin and the sample was placed into an ice bath to promote gelling. The resulting gel was poured into a disposable cuvette and left to set at ∼4°C for a couple of days.

- Sugar glasses were made by dissolving 600 mg of sucrose and 600 mg of trehalose into 1 mL of water under constant stirring at ∼90°C.[70,71] The flavin was added once the

sugar mixture had reached ∼60°C. The resulting solution was then poured into a disposable cuvette which was left to dry in an oven at ∼60°C for about four days.

- PVA films (10% w/w) were obtained by dissolving PVA into ultrapure water under constant stirring at ∼90°C.[74] The solution was left to cool down before the flavin was added. A milliliter of the resulting solution was then poured into a Petri dish and left to dry at room temperature for about four days. The film could then be peeled off the dish and used as such.

- Water/glycerol solutions were prepared at concentrations of 75% and 95% glycerol (v/v).

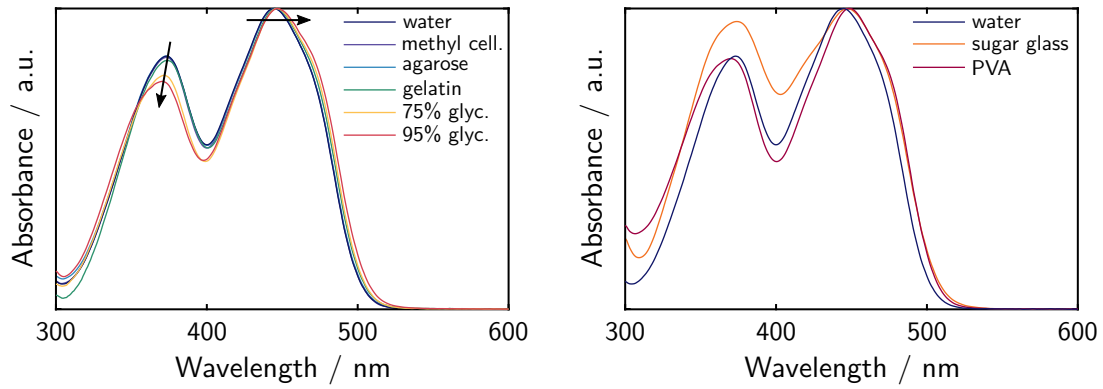
In the original works of Wright and Penzer that describe the preparation of sugar glasses and methyl cellulose gels, respectively, the samples were spread onto a glass plate.[67,70] In general, thin films tend to dry unevenly and are quite difficult to prepare in a reproducible way. Thus, the film's thickness may vary significantly from one film to another. The protocols proposed here, in which the initial solution is poured into a cuvette and left to dry over longer periods of time, were found to yield more reproducible samples without otherwise affecting their characteristics. The use of cuvettes also makes the samples easier to manipulate and investigate by optical spectroscopy. Using a similar method for PVA, however, was unsuccessful.

In most cases, the flavin concentration was kept relatively low ($\sim 20\,\mu$M) to prevent self-quenching and the inner filter effect. The flavin concentration of the solution used for the preparation of PVA films was $150\,\mu$M, so that the absorbance of the thin film was high enough to be detectable.

Only gelatin gels, sugar glasses and PVA films require the radical pair to be incorporated at a relatively high temperature. While it means that they cannot be used to immobilise cryptochromes, they are still relevant for the encapsulation of model systems. Indeed, while the ultimate goal of this study concerns cryptochromes, it would be unreasonable to neglect model systems as, at this stage, any measurement of an anisotropic MFE would already constitute a significant step forward.

2.4 Photophysical characterisation

As mentioned in the Introduction, flavins exhibit absorption bands centered around 375 and 450 nm and fluoresce at about 530 nm. Although the exact positions of the absorption and emission peaks are dependent on the interactions between the fluorophore and its environment, more dramatic differences could be indicative of significant changes in the structure of the flavin. Thus, UV-visible absorption and fluorescence spectra were recorded to ensure that the photophysical behaviour of the fluorophore was mostly maintained in the different confining environments considered. The absorption spectra are presented in Figure 2.1 and were normalised at the maximum of the absorption band corresponding to the $S_0 \rightarrow S_1$ transition to account for differences in path length between the different samples. For this reason, the discussion below will only be based on the relative magnitude of the two absorption bands.



(a) Gels and viscous solutions. The flavin concentration was $\sim 20\,\mu$M.

(b) Sugar glasses and PVA. The flavin concentration before drying was $\sim 20\,\mu$M for sugar glasses and $\sim 150\,\mu$M for PVA films.

Figure 2.1: Absorption spectra of FMN in the confining media under investigation. The spectra were normalised to account for the difference in path length and optical quality between the different samples.

The global shape of the absorption spectrum of FMN seems to be preserved in all the confining environments. They all clearly exhibit the two absorption bands characteristic of flavins, which suggests that FMN is able to maintain its integrity in these environments.

The 450 nm band, corresponding to the $S_0 \rightarrow S_1$ transition, is hardly affected and only undergoes a slight red-shift compared to water. This bathochromic shift increases following the order: agarose/methyl cellulose→gelatin→75% glycerol→95% glycerol/sugar glass→PVA film. Conversely, the 375 nm band, associated with the transition to the second singlet excited state S_2, exhibits a hypsochromic shift as well as a relative decrease in

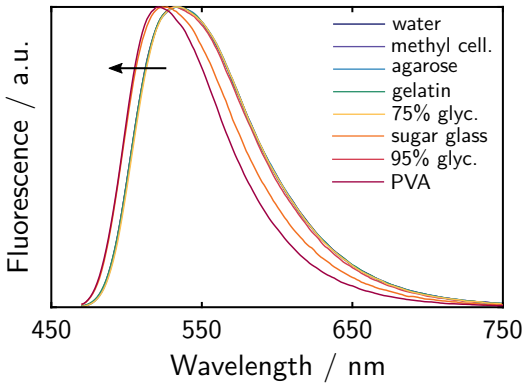


Figure 2.2: Fluorescence spectra of FMN in the different confining media under investigation. The samples were excited at 450 nm. The spectra were normalised to account for the difference in path length and optical quality between the different samples.

absorbance from water to gels, and again to glycerol solutions compared to the visible band. Note that for inhomogeneous samples, such as PVA films, whose thicknesses are difficult to control, and sugar glasses, which dry unevenly, imperfect background corrections can be observed. It is particularly true at lower wavelengths where scattering and the matrices' own absorption are more prominent. As a result, the position and intensity of the near-UV band for these samples cannot be interpreted.

The impact of the rigid matrices can also be seen on the fluorescence spectra recorded following photoexcitation at 450 nm (see Figure 2.2). While most of the samples' fluorescence spectra are almost identical to that of FMN in water, the spectra of PVA and sugar glasses are significantly blue-shifted.

The observed shifts in the positions of the absorption bands and fluorescence spectra can be partly explained by the relative polarities of the different matrices. As reported previously, the dipole moment of S_2 is larger than that of S_0.[75,76] Therefore, in a less polar environment, the excited state is less stabilised than the ground state, which gives rise to a hypsochromic shift, as observed in glycerol solutions (glycerol's dipole moment is μ_g=2.56 D) compared to water (μ_w=2.95 D).[77] The decrease in absorbance of the UV band compared to the visible one has previously been attributed to the $n \rightarrow \pi$ character of the transition which favours polar solvents.[21,78]

The case of the visible band is more complex. S_1 is also more dipolar than the ground state, albeit only sightly.[75,76] Following the previous reasoning, it is expected to exhibit a hypsochromic shift instead of the slight bathochromic shift observed experimentally. While this surprising red-shift is visible in the data presented in several studies, no attempts at

a physical interpretation have so far been provided anywhere in the literature.[79,80] Given that their respective works investigated the spectroscopic behaviour of flavins in reverse micelles and hydrophilic matrices, one hypothesis could be that this red-shift originates from structural changes experienced by S_1 in confining environments (such as, for instance, a change in the planarity of the molecule[80]), which would suggest that PVA, sugar glasses and glycerol solutions are more rigid environments than gels. In particular, PVA and glycerol solutions seem to be especially immobilising as the 450 nm band in the absorption spectrum exhibits a shoulder at slightly higher wavelengths, which is similar to the vibronic structure of flavins bound to proteins.[81]

The reason why the fluorescence does not follow the same trend as the visible absorption band from which it originates is the existence of solvent relaxation taking place once the excited state is created. One of the main sources of solvent relaxation is the reorientation of solvent molecules to stabilise the excited state dipole moment, which is expected to be more efficient in polar environments. Following this logic, the fluorescence spectra of the less polar environments are expected to be blue-shifted compared to that of water. This effect appears to be smaller for the fluorescence than for the 375 nm absorption band. This can be explained by the much smaller difference between the dipole moments of the excited and ground states, making the transition less sensitive to the polarity of the solvent.[75,76]

2.5 Determination of the degree of immobilisation

As discussed above, a critical requirement for a cryptochrome-based compass is that the radical pair partners must be immobilised and aligned to some extent. This, of course, has to be the case over the timescale of magnetosensitive processes, *i.e.* tens of ns for the magnetic fields considered in this work. However, this estimation does not take into account some more trivial and yet crucial practical considerations. Indeed, photoselection only ensures that the excited molecules are aligned immediately after excitation but the system is then able to evolve freely in its environment. Therefore, to ensure that the radicals are still aligned when singlet-triplet interconversion takes place, they also need to be immobilised over the timescale of their formation. In intramolecular systems, the electron transfer occurs immediately after photoexcitation on the sub-ns timescale and the timescale of the creation of the RP can be neglected.[38] Appreciable MFEs have been observed in cryptochromes $\sim$100 ns after photoexcitation, which corresponds to the time needed for

the MFE to develop over a few cycles of singlet-triplet interconversion.[82] In intermolecular systems, the electron transfer is limited by diffusion and its rate will, therefore, depend on the concentrations of the RP partners and their local environment.[83] In water, this process takes place over at a few 100 ns (as reported for the FMN-tryptophan RP for concentrations of the order of 100 μM[53]). In immobilising media, the electron transfer will most likely happen over much longer timescales. Thus, in order for anisotropic MFEs to be detected optically following photoselection of an isotropic sample, the rotational correlation time of the system should be at the very least of the order of $\sim$100 ns for cryptochromes and probably significantly longer for intermolecular radical pairs.

Fluorescence anisotropy assesses the degree of linear polarisation of fluorescence emission following photoselection. As will be explained in details in the following paragraphs, it enables the determination of the rotational correlation time of the fluorophores and can, therefore, be used to quantify the degree of immobilisation of the flavin molecules within different rigid matrices.

2.5.1 Introduction to fluorescence anisotropy

The theory of fluorescence anisotropy has been described in detail by Lakowicz.[84] A brief overview of the most important concepts is given here.

Fluorescence anisotropy (r) quantifies the extent of linear polarisation of the light emitted by a fluorophore excited with polarised light. It is based on the existence of transition dipole moments for absorption and emission that lie along specific directions within the fluorophore and is given by:

$$r = \frac{I_{\parallel} - I_{\perp}}{I_{\parallel} + 2I_{\perp}}, \tag{2.1}$$

where $I_{\parallel}$ and $I_{\perp}$ refer to the fluorescence intensities measured with a linear polariser for emission parallel and perperpendicular, respectively, to the electric vector of the incident light. r represents the difference between $I_{\parallel}$ and $I_{\perp}$ with respect to the total fluorescence intensity $I_{\mathrm{T}} = I_{\parallel} + 2I_{\perp}$.

Individual molecule The case of a single molecule is illustrated in Figure 2.3, in which the flavin is excited by z-polarised light. The transition dipole moment (assumed to be the same for excitation and emission for simplicity) is represented by the orange arrow and its

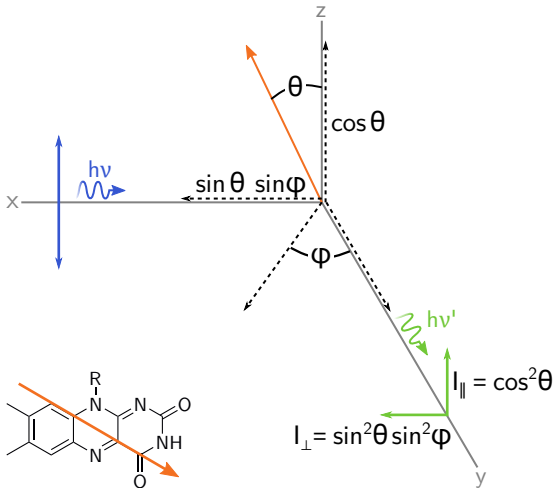


Figure 2.3: Principle of fluorescence anisotropy. A fluorophore is excited with z-polarised light. Its transition dipole moment is placed at the origin of the laboratory frame and is represented by the orange arrow. Its rough orientation in a flavin molecule is shown in the bottom-left corner.[85] The fluorophore is excited along the x-axis ($h\nu$) and its fluorescence ($h\nu'$) is measured through a polariser whose principal axis is either parallel or perpendicular to the electrical vector of the incident light. Adapted from Lakowicz.[84]

projections onto the different axes are highlighted. As the intensity of the emitted light polarised along an axis is proportional to the square of the projection of the transition moment onto the axis, $I_{\parallel}$ and $I_{\perp}$ are given by:

$$I_{\parallel}(\theta, \phi) = \cos^2(\theta) \tag{2.2}$$

$$I_{\perp}(\theta, \phi) = \sin^2(\theta)\sin^2(\phi) \tag{2.3}$$

Photoselection of a collection of randomly oriented fluorophores When an immobilised sample with randomly oriented fluorophores is excited by z-polarised light, the probability of absorption is proportional to $\cos^2(\theta)$, where θ is the angle between the electric vector of the incident light and the transition dipole moment. Hence, for a given θ, all molecules are excited with the same probability, independently from ϕ, whose contribution can be averaged as follows: $\langle \sin^2 \phi \rangle = 1/2$. The overall fluorescence anisotropy becomes:

$$r = \frac{3\langle \cos^2(\theta) \rangle - 1}{2}. \tag{2.4}$$

Further, the number of molecules whose transition dipole moments are oriented at an angle comprised between θ and $\theta + d\theta$ with respect to the electric vector is proportional

to $\sin(\theta)d\theta$. Thus, the distribution of photoselected molecules is:

$$f(\theta)d\theta = \cos^2(\theta)\sin(\theta)d\theta \tag{2.5}$$

and

$$\left\langle \cos^2(\theta) \right\rangle = \frac{\int_0^{\pi/2} \cos^2(\theta)\, f(\theta)\, d\theta}{\int_0^{\pi/2} f(\theta)\, d\theta} = \frac{3}{5}. \tag{2.6}$$

The anisotropy of a photoselected sample containing fluorophores with colinear absorption and emission transition dipole moments (which is a good assumption in flavins[76,85]) and undergoing no depolarisation can be determined by combining Equations 2.4 and 2.6, which yields 0.4. Thus, the fluorescence anisotropy of FMN embedded into the different immobilising matrices considered can be 0.4 at most.

Temporal evolution Although many factors can give rise to depolarisation, the most prominent is rotational diffusion of the fluorophores. In the ideal case of a spherical fluorophore,

$$r(t) = r_0 e^{-t/\tau_c} \tag{2.7}$$

where r_0 is the anisotropy at $t = 0$ and τ_c is the rotational correlation time. Concretely, the actual anisotropy decay is rarely a single exponential and usually has multiple components. Measuring the fluorescence anisotropy of flavins embedded inside the different matrices under invesgation allows to estimate their relative degree of immobilisation and, therefore, determine which one is the most suitable for the measurement of anisotropic MFEs.

Fluorescence anisotropy measurements In fluorescence spectrometers, the emission is recorded through a monochromator whose transmission efficiencies for vertically and horizontally polarised lights are usually different. With vertically polarised excitation, the measured vertically and horizontally polarised intensities are:

$$I_{VV} \propto S_V I_{\parallel} \tag{2.8}$$

$$I_{VH} \propto S_H I_{\perp} \tag{2.9}$$

where S_V and S_H are the spectrometer's emission channel sensivities for the vertically and horizontally polarised components, respectively. In order to measure the actual $I_{\parallel}$ and $I_{\perp}$,

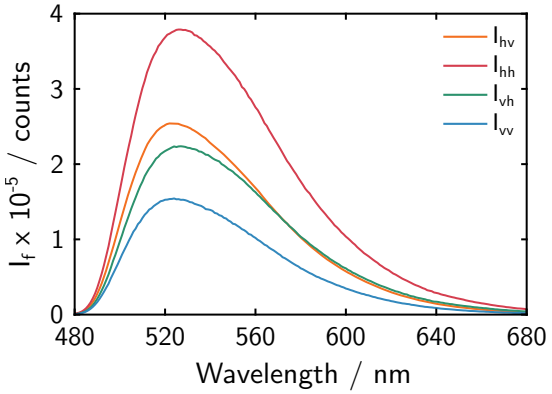
a correction factor, the G factor, is introduced. It represents the ratio of the detection sensitivities for vertically and horizontally polarised light: $G = S_V/S_H$. Its value can be determined by using horizontally polarised excitation as, in this case, the measured vertical and horizontal components are both proportional to $I_\perp$:

$$\frac{I_{HV}}{I_{HH}} = \frac{S_V I_\perp}{S_H I_\perp} = G \tag{2.10}$$

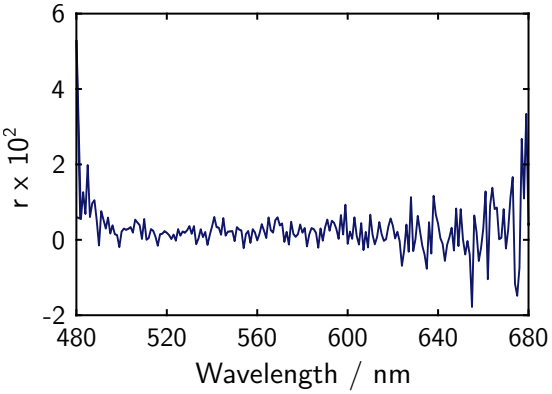
Taking into account the difference in detection sensitivities, the fluorescence anisotropy is now given by:

$$r = \frac{I_{VV} - G I_{VH}}{I_{VV} + 2G I_{VH}}. \tag{2.11}$$

An illustrative measurement of the fluorescence anisotropy of FMN in water is presented in Figure 2.4. Given the very low viscosity of water and the small size of the fluorophore, the latter is able to tumble freely in solution and its fluorescence anisotropy is about zero. Note that the emission anisotropy is wavelength independent since the emission is always due to the transition from the first singlet state.



(a) Vertically and horizontally polarised components of the fluorescence following excitation with vertical (I_{VV} and I_{VH}) and horizontal (I_{HV} and I_{HH}) polarised light.



(b) Steady-state fluorescence anisotropy.

Figure 2.4: Fluorescence anisotropy measurement of a 10 μM FMN solution in water following excitation at 450 nm.

2.5.2 Steady-state anisotropy measurements

For each immobilising medium considered, five identical samples were prepared as described above. Their fluorescence anisotropies were measured with a fluorescence spectrometer FS5 from Edinburgh Instruments fitted with two polariser assemblies (extension FS5-POL), one

in the excitation beam path and the other in the emission beam path. The 450 nm excitation was provided by a xenon arc lamp and a 455 nm long-pass filter was positioned in the detection path to prevent any scattered light from reaching the detector. The PVA films were measured using a solid sample holder which allowed to position the films at an angle of ∼30° with respect to the incident beam so as to minimise stray light.[84] The steady-state anisotropies of the different immobilising media are given in Figure 2.5. Each anisotropy value corresponds to the average of five measurements and the uncertainty on each value is given by the standard deviation.

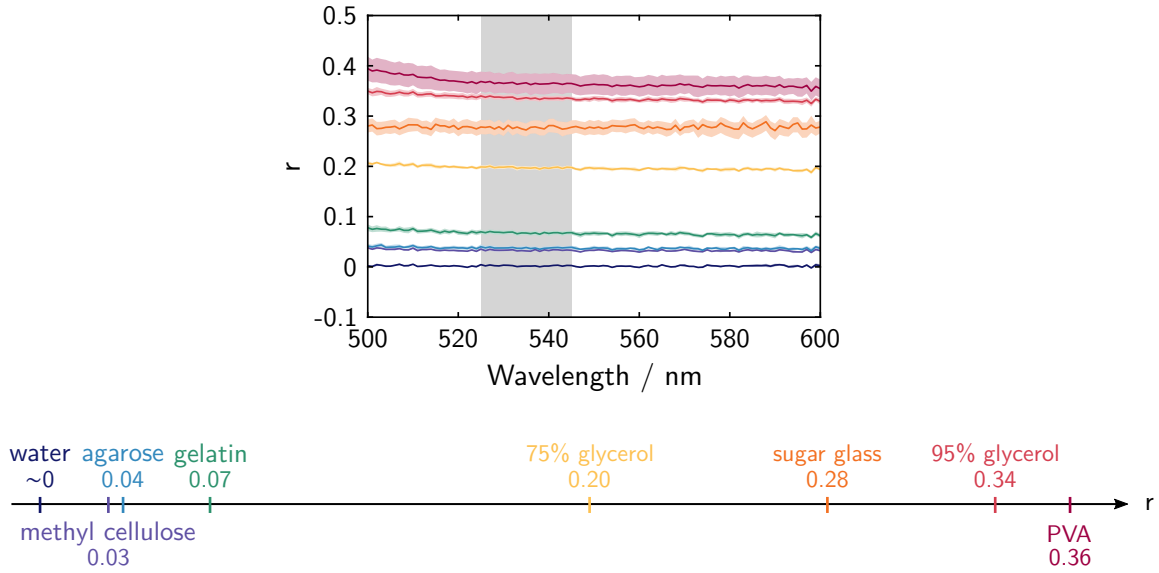


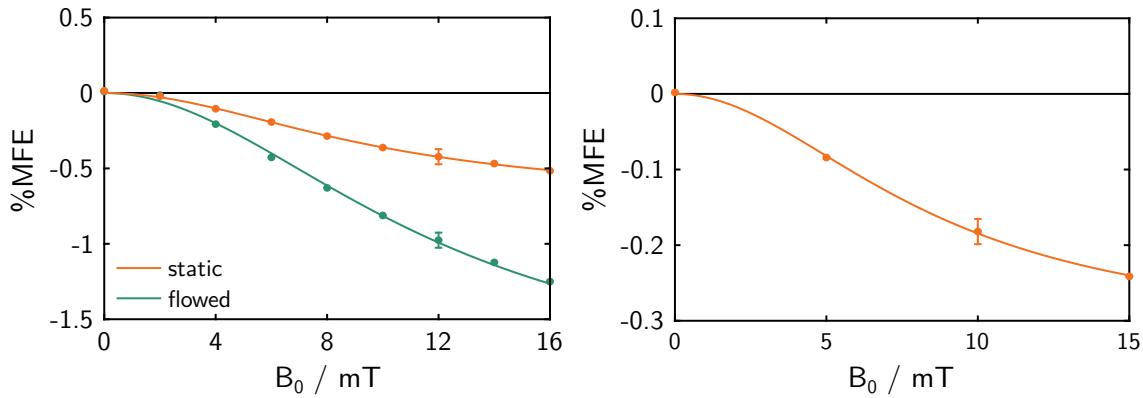
Figure 2.5: Steady-state anisotropies of the different media under investigation. Each anisotropy value corresponds to the average of five measurements over the wavelength range 525–545 nm represented by the grey shaded area.

Unsurprisingly, the rotational diffusion of flavin molecules in the gels, which have a very high water content, is barely hindered. On the other hand, sugar glasses, glycerol solutions and PVA seem to be quite promising. In particular, the steady-state anisotropy in PVA is very close to the theoretical limit for fully immobilised fluorophores.

Interestingly, it seems that the degree of immobilisation provided by the different media is somewhat correlated with the red-shift of the 450 nm absorption band, which supports the assumption that this bathochromic shift stems from the more confining microenvironment of the flavins.

2.6 Magnetic field effects

Before looking in more detail at the ability of the confining environments to hinder the rotational diffusion of the radicals, it is crucial to check that the last prerequisite for these matrices is met and that encapsulating the system does not inhibit its capacity to develop magnetic field effects. This was tested by measuring the MARY curve of an FMN-tryptophan radical pair embedded in the different media under investigation. As some of the matrices are inhomogeneous and highly scattering, the prompt fluorescence MARY experiment was employed. Out of all the rigid matrices considered, PVA is the only one in which no MFE could be measured even though its absorption and fluorescence spectra showed that the flavin seems to have maintained its integrity within the film. All other samples exhibited appreciable MFEs



(a) 95% aqueous glycerol solution. A representative error bar is depicted at B_0=12 mT.

(b) Sugar glass. A representative error bar is depicted at B_0=10 mT.

Figure 2.6: MARY curves of ~10 μM FMN and ~0.5 mM tryptophan encapsulated in different rigid matrices. The MFEs were measured by prompt fluorescence at room temperature.

Examples of MARY curves in aqueous glycerol solutions and sugar glasses are shown in Figure 2.6. The MFEs are relatively large compared to the ones presented in the previous chapter. This can be explained by the increased viscosity, which has previously been shown by Evans *et al.* to enhance MFEs by slowing down radical recombination.[39] Even though glycerol solutions can be flowed, the MFE of FMN-tryptophan in 95% glycerol was also measured using a static sample, in part for comparability with sugar glasses but mainly because anisotropy studies would have to be conducted on immobile samples. Interestingly, it is significantly lower than that of a flowed sample measured with the same experimental parameters. This can be explained by the interplay between photobleaching and diffusion. Flavins are extremely sensitive to photobleaching and photodegrade quite quickly, even

under gentle illumination conditions, which is why FMN-tryptophan solution samples are usually flowed.[20] Fluorescence-detected MFEs have been shown to be a function of flavin concentration.[53] Hence, if the sample bleaches considerably and the flavin concentration drops, the MFE is expected to be suppressed. Fluorescence anisotropy showed that sugar glasses and glycerol solutions are strongly immobilising. Within these confining environments, the photobleached fluorophores cannot be replenished efficiently by diffusion from the non-illuminated part of the sample, making it even more sensitive to photobleaching. The lower MFE observed in sugar glasses compared to glycerol is more surprising given that the latter is more immobilising. This can be explained by the fact that sugar glasses were prepared in smaller cuvettes than the ones used for glycerol in order for them to dry faster. Because of the smaller accessible volume of non-irradiated fluorophores, photobleaching had a larger impact on sugar glasses than on glycerol solutions over the course of the experiment as the photobleached sample could not be replenished as efficiently, hence giving rise to a smaller MFE. For this reason, the experiment was made as short as possible by decreasing the number of field points acquired.

Fluorescence anisotropy showed that PVA is the most immobilising matrix. As such, it is more subject to photobleaching than the other media. It is, therefore, likely that even the very gentle photoexcitation conditions employed caused the sample to photodegrade extremely quickly, making any attempt at detecting MFEs vain. Additionally, in intermolecular systems, diffusion plays a crucial role in the establishment of magnetic field effects. The radical pair can only be formed if the electron donor and acceptor are close enough for the electron transfer to occur and they then need to diffuse apart for spin interconversion to take place before re-encounter. In PVA films, the estimated average distances between FMN and tryptophan molecules is of the order of a couple of nanometers but electron transfers typically take place over distances of the order of a few Å. Hence, it is likely that, in such a rigid matrix, the donor-acceptor separation is too large for the electron transfer to occur. If this is the primary cause of the absence of MFEs in PVA, using intramolecular systems would solve that problem. As mentioned above, cryptochromes are out of the question as PVA films are prepared at too high a temperature. An intramolecular model system would, therefore, have to be used. The only intramolecular flavin-based model system is FAD, which has an appreciable MFE at low pH and was recently showed to exhibit a small MFE (about seven times smaller than at low pH) at neutral pH.[86] Unfortunately, no MFE could be detected for FAD in PVA films either, which definitily rules

out the use of PVA films for the detection of anisotropic MFEs.

2.7 Using aqueous glycerol solutions as an immobilising medium

Based on the experimental results and considerations detailed above, aqueous glycerol solutions appear to be the most promising medium for the encapsulation of flavin-based radical pairs. However, a note of caution is due here since the steady-state anisotropy results presented above only reflect the degree of immobilisation of the fluorophore on the timescale of its fluorescence lifetime ($\sim$ 5 ns) and should not be extrapolated to longer timescales without closer inspection.

2.7.1 Methods

To fully assess the ability of glycerol solutions to immobilise radical pairs long enough for anisotropic MFEs to be detected, time-resolved anisotropy measurements were performed. The FS5 fluorescence spectrometer was used in its time-correlated single photon counting (TCSCP) mode. The sample was excited with a 450 nm pulsed diode laser (repetition rate 5 MHz) and the fluorescence was detected at 530 nm by a TCSCP photomultiplier over a 60 s averaging period. For the deconvolution procedure, the instrument response function (IRF) was determined using a freshly made solution of ludox in water (half-bandwidth $\sim$ 240 ps). The samples were placed within a liquid nitrogen cryostat to control the temperature.

Time-resolved fluorescence and fluorescence anisotropy decays were fitted with a sum of exponentials convolved with the IRF according to:

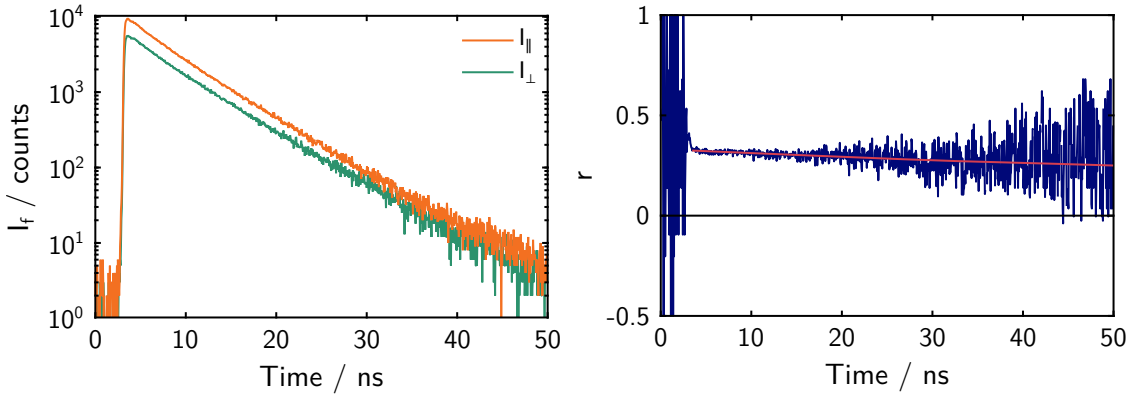
$$r(t) = \mathrm{IRF} * \sum_i a_i e^{-t/\tau_i} \tag{2.12}$$

where a_i and τ_i represent the amplitude and lifetime associated with the component i.

2.7.2 Immobilising model systems

The fluorescence anisotropy decay of FMN in 95 % glycerol at 278 K, which is the temperature at which most MFE experiments are run, is depicted in Figure 2.7. It was found to be well described by a single exponential with a rotational correlation time

$\tau_c(278\,\mathrm{K}) = 192 \pm 44\,\mathrm{ns}$.



(a) Vertically and horizontally polarised components of the fluorescence.

(b) Time-resolved fluorescence anisotropy and corresponding fit.

Figure 2.7: Time-resolved fluorescence anisotropy measurement of FMN in 95% glycerol following excitation at 450 nm.

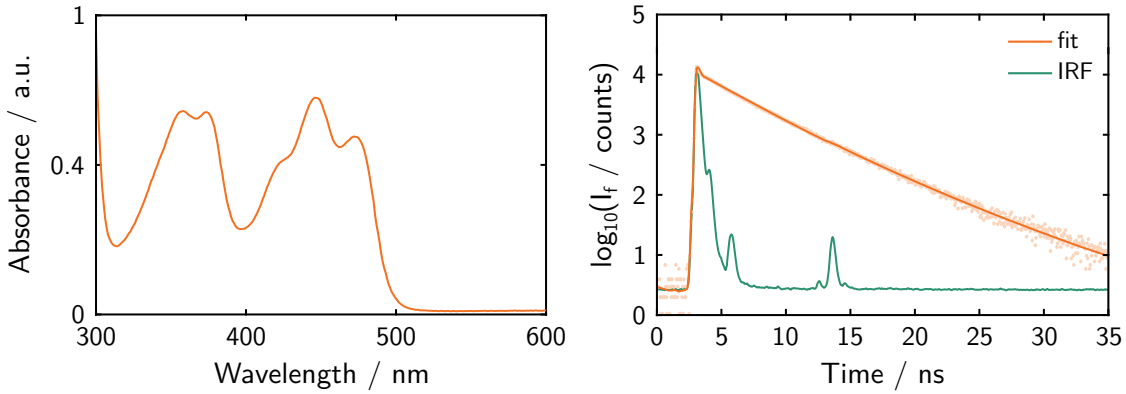
Based on the discussion in Section 2.5, the time-resolved fluorescence anisotropy results for FMN indicate that its rotational correlation time is long enough to immobilise the flavin over the timescale of the magnetosensitive processes. However, in such a viscous environment, the RP formation is most likly much longer than the measured rotational correlation time and it is, therefore, improbable that, in the case of an intermolecular system, the radical pair partners would maintain their orientations over the course of the RP formation. It might be possible to find a set of experimental conditions under which this system could develop anisotropic MFEs (for instance, by increasing the concentrations of RP partners to accelerate the RP formation) but it would most likely require a very long optimisation process which, in light of the elements discussed below, might not be worth conducting.

2.7.3 Immobilising cryptochromes

Given how much larger cryptochromes are (MW $\approx$ 50-70 kDa[87]) compared to flavins, their rotational mobility is expected to be significantly more hindered in glycerol solutions. This was tested on a sample provided by Prof. Henrik Mouritsen's lab containing *Er*Cry4 W369F, a mutant of the cryptochrome 4 from the night-migratory European robin (*Erithacus rubecula*). The sample was prepared in Tris buffer (pH 8, 20 mM Tris, 200 mM NaCl, 20% glycerol) and measured at 278 K.

In order to characterise the sample, its absorption spectrum as well as its time-resolved

fluorescence decay were first measured. The results are displayed in Figure 2.8.



(a) UV-vis absorption spectrum.

(b) TCSCP fluorescence decay and corresponding triple exponential fit. The instrument response function (IRF) is shown for reference.

Figure 2.8: Photophysical characterisation of *Er*Cry W369F in Tris buffer (pH 8, 20% glycerol) at 5 °C.

The absorption spectrum exhibits the two absorption bands characteristic of flavins. The presence of the vibrational structure of the 450 nm peak confirms that the flavin is correctly bound to the protein.[81] The lack of signal beyond 520 nm indicates that the flavin is in its oxidised form, as expected.

The fluorescence decay is well-fitted by a sum of three exponentials with $\tau_1 = 5.5\,\text{ns}$, $\tau_2 = 3.2\,\text{ns}$ and $\tau_3 < 240\,\text{ps}$. The lifetime of the last component could not be resolved as it is faster than the instrument response. Although the time-resolved fluorescence of this specific cryptochrome has never been investigated before, these results are in good agreement with previous reports on other cryptochromes.[24,88,89] The fast component is attributed to the FAD cofactor buried within the protein. The longer components stem from the existence of unbound flavin in the sample. It is common to find traces of free flavin that has not been properly incorporated into the protein in cryptochrome samples. The difference between the lifetimes of the slower components originates from the different conformations adopted by FAD. It is well known that FAD has two main conformations: the stacked conformation, in which the molecule adopts a U-shape where the isoalloxazine ring and the adenine are close to each other, and the open conformation. Recent developments have identified a third, partially-stacked conformation where the isoalloxazine and adenine moieties are not stacked but still interact with each other, resulting in a lower fluorescence lifetime than that of the open conformation.[90] At pH 8, both the open and partially stacked conformations exist in solution, which explains the presence of the two ns-lifetimes.[91]

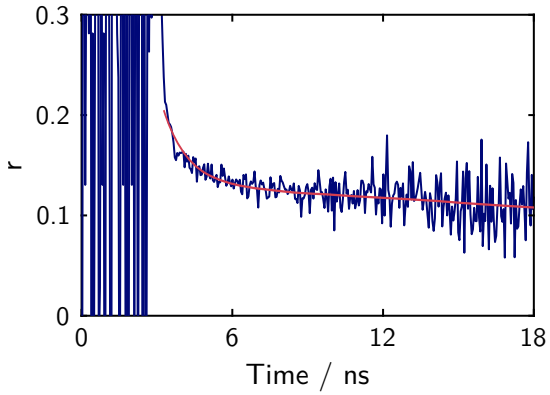


Figure 2.9: Time-resolved fluorescence anisotropy of *Er*Cry W369F mutant in Tris buffer (pH 8, 20% glycerol) at 5 °C following excitation at 450 nm.

The time-resolved anisotropy decay of *Er*Cry4 W369F at 278 K is depicted in Figure 2.9. It is well-described by two exponential components with $\tau_1 = 78 \pm 19$ ns and $\tau_2 = 0.9 \pm 0.1$ ns.

The fast component is attributed to free flavin and the slow component corresponds to the global rotational diffusion of the protein. The rotational diffusion coefficient and correlation time of a globular protein can be estimated relatively well using the Stokes-Einstein relation:[92]

$$D = \frac{k_B T}{6\eta V}, \tau_c = \frac{1}{6D} = \frac{\eta V}{k_B T} \tag{2.13}$$

in which η is the dynamic viscosity of the solvent in Pa.s, T is the temperature in Kelvin and V is the volume of the protein in m^3. In the case of a globular protein, the volume can be estimated using:[84]

$$V = \mathrm{MW}(\overline{\nu} + h) \tag{2.14}$$

where MW is the molecular weight of the protein in Dalton, $\overline{\nu}$ is the specific volume in m^3/g and h is the degree of hydration in m^3/g. Empirically, for most proteins $\overline{\nu} = 0.73$ mL/g and $h = 0.2$ mL/g.[93,94] Alternately, the molecular volume can also be determined quite easily using programs such as Chimera.[27] Both methods give comparable results. Using a molecular weight of 64 kDa, the estimated rotational correlation time of a cryptochrome in 20% glycerol at 278 K ($\eta = 3.22$ cP[95]) is $\tau_c = 83$ ns, which is in excellent agreement with the slower lifetime measured.[96] This is probably not slow enough, according to the criterion established above, for the cryptochrome RP to develop an appreciable anisotropic MFE. However, some cryptochromes are also stable in buffers containing 50% glycerol, and MFEs have even been measured in such conditions.[36] In this case, the estimated rotational

correlation time is $\tau_c \sim 400\,\text{ns}$, which would be more than sufficient. This could not be tested with the robin cryptochrome as, so far, our collaborators have only been able to express and purify this protein with reasonable confidence under very specific conditions which do not include such a high glycerol content.

2.8 Conclusion and outlook

This chapter has explored different methods to generate an aligned and immobilised population of radical pairs for the measurement of their directionally dependent response to a magnetic field.

Following a systematic assessment and comparison of several rigid matrices, aqueous glycerol solutions were found to be the most promising for the following reasons:

- They can be easily prepared in spectroscopy labs and can be studied using the experiments traditionally employed for the investigation of MFEs.
- The absorption and fluorescence spectra of FMN in these solutions exhibit the expected characteristic features, which indicates that the photophysical properties of the flavin are not altered in this different environment. Most importantly, glycerol has proven to be very protein-friendly and is routinely used in buffers for cryptochromes.[34]
- MFEs can de detected in glycerol solutions containing a flavin-based radical pair.
- Fluorescence anisotropy studies demonstrated that glycerol solutions hinder the rotational diffusion of the flavin very efficiently.

In spite of this, aqueous glycerol solutions are not rigid enough to immobilise intermolecular model systems long enough for anisotropic MFEs to develop. An intramolecular model system (*i.e.* FAD) could, in principle, exhibit anisotropic MFEs in such conditions, but it would still be subjected to fast photobleaching which would complicate the detection of such effects.

In cryptochromes, photobleaching is less of an issue as the proteins can reoxidise. A closer inspection of the degree of immobilisation provided by glycerol solutions revealed that, in the conditions traditionally used for the study of MFEs in cryptochromes (*i.e.* 20% glycerol at 5 °C), the rotational correlation time of the proteins is expected to be

$\sim$ 80 ns, which is, in all probability, not long enough for them to exhibit an anisotropic MFE. However, some cryptochromes have previously been studied in buffers with higher glycerol contents. At 50% glycerol (v/v) for instance, the rotational correlation time of a cryptochrome is expected to be about 400 ns, which is in principle sufficient for the radicals to be a source of directional information.

Chapter 3

Magnetic Field Effects in Viscous Solutions

In the previous chapter, aqueous glycerol solutions were established as the most suitable immobilising medium for the detection of anisotropic magnetic field effects in flavin-based systems. As part of this investigation, a surprising and previously unsuspected MFE was discovered. In the absence of any traditional electron donor, such as HEWL, tryptophan or similar, FMN was found to exhibit an appreciable MFE in aqueous glycerol solutions.

The existence of this MFE has the potential to be problematic. To date, all spectroscopic experiments aiming to characterise the magnetosensitivity of cryptochromes have been conducted in buffers containing up to 60% glycerol by volume.[34] Crucially, cryptochrome samples always contain a small amount of free flavin molecules whose concentration is not controllable and might change over the course of a spectroscopic measurement. Indeed, when cryptochromes solutions are received from collaborators in Germany, they already contain some free flavin. Upon arrival, the samples are washed several times so that most of the free flavin is eliminated but, as seen in the previous chapter, some traces are still present in the final sample. Further, the flavin cofactor in cryptochromes is not covalently bound but rather trapped inside the protein backbone and may be released if the protein misfolds over the course of the experiment, which affects its concentration over time.

So far, the presence of free flavin has been mostly neglected as it was assumed to be of little consequence. Indeed, even though FAD has been shown to generate an intramolecular radical pair between the isoalloxazine ring and the adenine moiety, the MFE stemming from this phenomenon is mostly visible at very low pH and is barely detectable at physiological pH, at which cryptochromes experiments are conducted.[86,97] In light of the existence of the previously unknown MFE exibited by free flavin in glycerol aqueous solutions, the impact of the presence of free flavin needs to be examined more closely. Whilst it is unlikely that the MFEs previously recorded on cryptochromes in glycerol-containing buffers are solely originating from the reaction of free flavin in glycerol, the intrinsic cryptochrome MFE

could very well be distorted by that of the free flavin. Either way, this calls for a better understanding of the mechanism of this field sensitivity and a careful examination of the conditions under which it arises.

3.1 Methods

In order to fully characterise and understand the origin of the MFE of FMN in aqueous solutions, a variety of experiments were employed.

PF MARY

The PF MARY apparatus was introduced in Chapter 1. The samples were flowed with a syringe pump as the very narrow tubing of the customary peristaltic pump is not suitable for solutions with high glycerol content. As a result, the quality of the flow was not as good as usual and the signal-to-noise of the obtained MARY curves was slightly lower than for the data presented in the previous chapters.

Transient absorption

Transient absorption (TA) spectroscopy was employed to determine the mechanism of the reaction. The measurements were performed on a Ultrafast Systems EOS spectrometer modified for MFE experiments. Pump excitation at 450 nm was provided by a mode-locked picosecond Nd:YAG laser (Ekspla PL2210) and an optical paramagnetic generator (OPG, PG403). The probe light source of the spectrometer is a supercontinuum white light laser. The sample was flowed by a syringe pump through a fluorescence flow cell (Hellma, 1 cm path length) placed at the point of pump-probe overlap. The magnetic field was provided by a set of home-built Helmholtz coils surrounding the sample and controlled by a LabVIEW code. Note that the data acquisition software is designed in such a way that it prioritises the collection of points at early times. Therefore, the time points are not distributed evenly across the time range of interest. Instead, the interval between each point increases as the pump-probe delay time becomes larger. Thus, in order to properly examine longer delay times, a lower temporal resolution must be employed. Several data sets with different temporal resolutions are usually measured in order to properly characterise the sample's behaviour over the full time range.

Cavity ring-down spectroscopy

As mentioned in the Introduction, cavity ring-down spectroscopy (CRDS) is quite similar to TA but uses an optical cavity to enhance the sensitivity by passing light through the sample multiple times. CRDS measurements were conducted on a spectrometer built by Matthew Golesworthy and based on that described by Maeda *et al.*[38] The sample was flowed by a syringe pump through quartz flow cell (Hellma, 165-QS, 1 mm path length) placed in the centre of an optical cavity comprised of two highly reflective mirrors (Layertec). Pump excitation at 450 nm was provided by a Nd:YAG (Continuum, Surelite I) pumped dye laser (Sirah, Cobra). The probe beam was generated by a tunable optical parametric oscillator (Opotek, Opolette) and introduced into the cavity via the front mirror. The probe light leaving the rear mirror was detected by a photomultiplier tube (Hamamatsu, H6780) and recorded on a digital oscilloscope (LeCroy, WaveSurfer 64MXs-A). MFE measurements were conducted using a 30 mT magnetic field generated by a set of home-built Helmholtz coils. CRDS experiments were conducted in collaboration with Matthew Golesworthy.

3.2 Origin of the magnetic field effect

3.2.1 Characteristics of the magnetic field effect

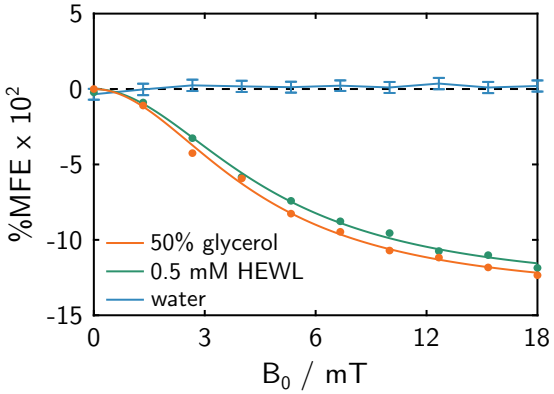


Figure 3.1: MFE of 50 μM FMN in different solvents. The data were acquired using PF MARY with an excitation power of 20 mW.

The magnetosensitivity of 50 μM FMN measured by PF MARY in different conditions is depicted in Figure 3.1. These data highlight three important observations:

- FMN in pure water (in blue), which serves as a negative control, is not magnetosensitive whereas, in the presence of glycerol, the sample exhibits a very clear MFE (in

orange). The absence of MFE in water might seem trivial but is actually essential as it confirms that the MFE observed in glycerol is real and not merely an artefact stemming from a potentially poorly calibrated experiment or dirty experimental components (*e.g.* cuvette, tubing).

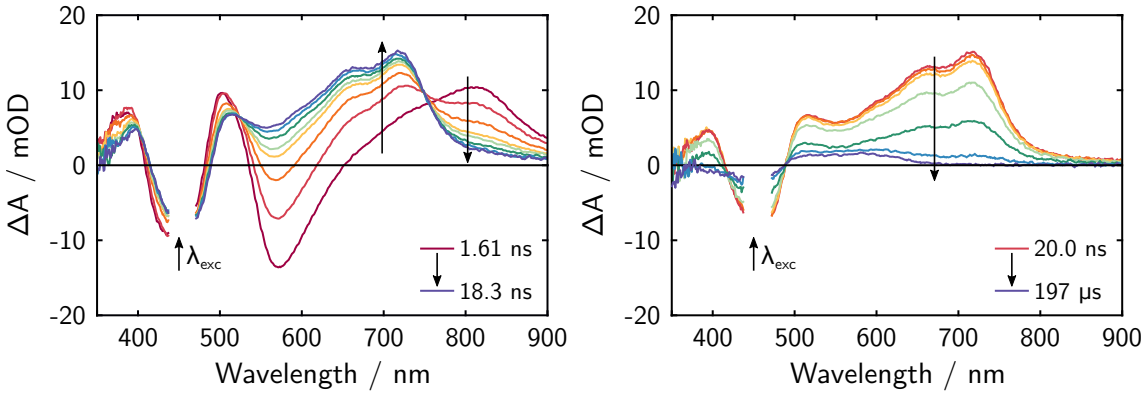
- The MFE of FMN in glycerol is negative, akin to that of a triplet-born radical pair. Similar results were also obtained with different flavin and glycerol concentrations, which suggest that an increase in the field always results in a decrease of the system's fluorescence. Conversely, in cryptochromes, the MFE is expected to be positive when measured by fluorescence spectroscopy, as first observed by Evans and co-workers (see Chapter 5 for a more detailed discussion).[39] Thus, the main concern regarding the existence of this MFE is alleviated as the validity of the positive MFE detected in cryptochromes is now ascertained.

- Worryingly, the MFE of FMN in a aqueous glycerol solution is of the same order of magnitude as that of the traditional radical pair model system FMN-HEWL in the absence of glycerol (in green). This implies that MFEs of model systems in the presence of glycerol might be the result of two separate phenomena and that the studies that have so far been conducted on such systems may need to be revisited and potentially reinterpreted accordingly in light of this new development.

Additionally, it should be noted that commercially available FMN is only 73-79% pure (F6750, Sigma Aldrich, purity determined by fluorimetry). In principle, the presence of impurities in the sample could lead to the development of an MFE. However, similar results were obtained with purified FMN, which was kindly provided by the lab of Prof. Erik Schleicher.

3.2.2 Photophysical characterisation of the system

In order to gain some insight into the origin of the MFE, the spectro-temporal evolution of the system was first examined. The transient absorption spectra of a solution of 200 μM FMN in 50% glycerol measured at different pump-probe delay times are displayed in Figure 3.2. Note that a larger FMN concentration was employed for TA experiments in order to maximise the signal-to-noise ratio but was found not to affect the general behaviour of the system.



(a) Early times.

(b) Later times.

Figure 3.2: Evolution of the transient absorption spectrum of 200 μM in 50% glycerol/50% phosphate buffer pH 7.4. The data presented here was recorded with a temporal resolution of 1 ns.

Several spectral features can be distinguished. The negative bands at 450 nm and 570 nm can be attributed to the ground state bleach and stimulated emission, respectively.[98] The positive features at 380, 505, 700 and 810 nm correspond to the absorption of transient species.

The photochemistry of flavins has been relatively well characterised and the temporal evolution of the signal can, therefore, be interpreted in light of the reference spectra available in the literature. Two distinct phases can be distinguished. At early times (a), the singlet excited state is immediately formed. It is easily identifiable by the presence of the stimulated emission band and the absorption peak at 800 nm.[99] As expected, it then proceeds to the triplet excited state via intersystem crossing, giving rise to the feature at 700 nm.[99,100] What is more surprising is the behaviour of the system at later times (b). Instead of a simple decay of the triplet and coinciding recovery of the ground state, the formation of a long-lived species (whose main absorption feature is between 500 and 650 nm) can be seen. The spectrum at $t = 197\,\mu$s is reminiscent of the spectral signature of the neutral flavin semiquinone, $FMNH^{\bullet}$, but also comprises small contributions from the triplet state and the ground state absorption, as demonstrated by Figure 3.3.[100,101]

3.2.3 Time-resolved MFE

Before analysing further the transient absorption data and examining the kinetics of the system, it is worth checking that this suprising formation of the flavin semiquinone radical in glycerol-containing solvents at later times is indeed responsible for the development of

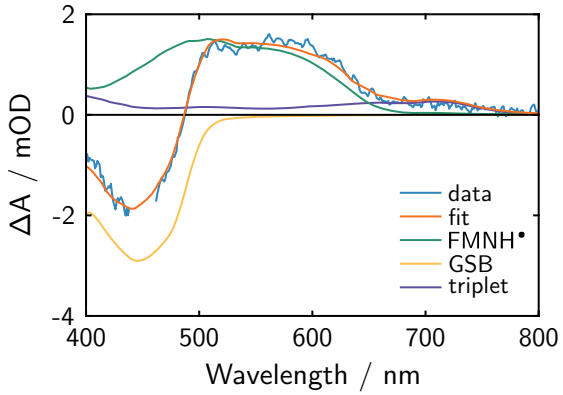
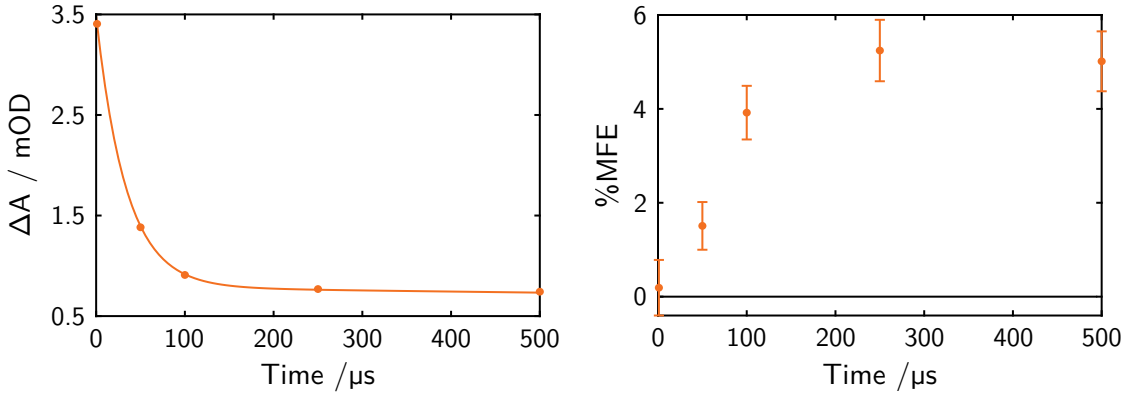


Figure 3.3: Deconvolution of the transient absorption spectrum at $t = 197\,\mu$s (from Figure 3.2) following excitation at 450 nm. The data corresponds to a linear combination of the spectra of FMNH$^\bullet$, the flavin triplet excited state and the ground state bleach (GSB). The reference spectra are reproduced from Li *et al.*[100]

the MFE. Unfortunately, the TA experiment was found not to be sufficiently sensitive to detect this MFE and cavity ring-down spectroscopy was employed instead as its multi-pass nature renders this experiment more sensitive than the single pass TA. However, the time resolution of the former is effectively limited by the ring-down time, *i.e.* the rate at which light exits the cavity, meaning that the experiment is essentially blind to pump-probe delay times below 1 μs. Based on the TA data presented above, the formation of the long-lived radical occurs on the μs timescale, which makes CRDS perfectly suitable for the investigation of this process. The MFE detected at 570 nm following photoexcitation at 450 nm is presented in Figure 3.4. Note that the sample was prepared in 75% glycerol as glycerol effectively acts as a pulsation dampener and allows the flow to be of better quality which, in turn, increases the signal-to-noise ratio of the MFE.

The decay of ΔA at 570 nm is consistent with the TA data showed above and corresponds to the decay of the triplet state and coincident formation of FMNH$^\bullet$. It can be well fitted with a double exponential with timescales $\tau_1 = 34 \pm 0.5\,\mu$s and $\tau_2 = 6.9 \pm 0.5$ ms.

Importantly, a positive MFE, characteristic of a triplet-formed RP examined by an absorption-based technique, develops concomitantly with the formation of the flavin radical. This confirms that this species at the origin of the magnetosensitivity exhibited by flavins in aqueous glycerol solutions. Both the flavin radical and the MFE are surprisingly long-lived, as confirmed by experiments conducted on a longer timescale, which detected their presence 10 ms after photoexcitation.



(a) Decay of the transient absorption of the system in the absence of the field. The line corresponds to a double exponential fit.

(b) Time-resolved MFE measured at 30 mT.

Figure 3.4: Temporal evolution of the absorption and MFE of a solution of 200 μM FMN in 75% glycerol measured by CRDS at 570 nm with pump-probe delay times ranging from 1 to 500 μs.

3.3 Proposed mechanism

The previous section concluded that the flavin semiquinone radical is responsible for the development of the MFE observed in flavin-containing glycerol acqueous solution, which raises the question of its formation in the apparent absence of an electron donor. Considering that FMN and glycerol are the only solutes present in the sample, it is clear that $FMNH^{\bullet}$ has to be the product of a reaction between either FMN and glycerol or two FMN molecules. Examples of both processes, which are discussed below, can be found in the literature.[101–103]

3.3.1 Potential mechanisms considered

Triplet-triplet annihilation

In the absence of an exogenous electron donor, it has been demonstrated that two flavin triplet excited states could generate a flavin semiquinone radical via triplet-triplet annihilation. This reaction was first observed by Hammerich *et al.* and was then further characterised by Bernt Melø and co-workers.[101,102] Based on their analyses, the annihilation of two triplet molecules produces a cation-anion pair and the anion rapidly converts into a semiquinone radical, which can then form radical pairs following random encounters

with other semiquinone molecules, as follows:

$$^3F^* + {}^3F^* \longrightarrow F^{\bullet +} + F^{\bullet -} \tag{3.1a}$$

$$F^{\bullet -} \longrightarrow FH^\bullet \tag{3.1b}$$

$$FH^\bullet + FH^\bullet \longrightarrow [FH^\bullet\, FH^\bullet] \longrightarrow FH_2 + F \tag{3.1c}$$

Although the TA data presented above do not exhibit any obvious indication of the presence of the flavin anion radical, its spectral signature could be hidden by that of the ground state, which absorbs in the same spectral region.[104] The fate of the cation radical is more complex and unclear. Bernt Melø and co-workers speculated that it could form lumiflavin, whose absorption spectrum is almost identical to that of FMN, and a ribityl radical by-product, but there little experimental evidence to substantiate this hypothesis.[101] A very small MFE on this reaction was recently detected in pure water by Antill *et al.*[86] Assuming this reaction takes place here, the presence of glycerol could effectively foster the development of the MFE, as observed by Evans *et al.*, allowing it to reach a magnitude similar to that of FMN-HEWL, as measured experimentally.[39]

Reaction of FMN and glycerol

As part of their extensive work examining the behaviour of flavins by flash photolysis, Green and Tollin have demonstrated that hydroxylic solvents, and in particular glycerol, could photoreduce flavin molecules and generate the flavin semiquinone radical via hydrogen abstraction.[103] While no MFE has ever been reported on this system, it is entirely possible that the radical pairs formed by $FMNH^\bullet$ with either glycerol or, similar to the first mechanism, another flavin semiquinone radical, could give rise to a MFE.

3.3.2 Formation of $FMNH^\bullet$

Global target analysis

Global target analysis (GTA) of the transient absorption data presented above can be used to unravel the processes underlying the observed spectroscopic changes and gain some insight into the mechanism of the formation of $FMNH^\bullet$. A very brief introduction to GTA will be given here. Several excellent reviews discussing the intricacies of this analysis

method, such as that of van Stokkum, are available in the literature.[105]

Essentially, GTA is based on two principles. First, temporal and spectral properties are assumed to be separable, meaning that the spectra of the species present in the system are considered to be time-independent. Second, spectral properties abide by the superposition principle such that the measured transient absorption spectra result from the superposition of the spectral properties (ϵ) of the n species present in the system weighted by their respective concentration (c), as follows:

$$\Delta\mathrm{A}(t,\lambda) = \sum_{i=1}^{n} c_i(t)\epsilon_i(\lambda) \tag{3.2}$$

which can conveniently be expressed in matrix form:

$$\mathbf{A} = \mathbf{EC} = \begin{pmatrix} \epsilon_1(\lambda_1) & \epsilon_2(\lambda_1) & \cdots & \epsilon_n(\lambda_1) \\ \epsilon_1(\lambda_2) & \epsilon_2(\lambda_2) & \cdots & \epsilon_n(\lambda_2) \\ \vdots & \vdots & \ddots & \vdots \\ \epsilon_1(\lambda_i) & \epsilon_2(\lambda_i) & \cdots & \epsilon_n(\lambda_i) \end{pmatrix} \begin{pmatrix} c_1(t_1) & c_1(t_2) & \cdots & c_1(t_j) \\ c_2(t_1) & c_2(t_2) & \cdots & c_2(t_j) \\ \vdots & \vdots & \ddots & \vdots \\ c_n(t_1) & c_n(t_2) & \cdots & c_n(t_j) \end{pmatrix} \tag{3.3}$$

where **C** contain the time-dependent concentrations of the species present in the system and **E** corresponds to their respective spectra, the so-called species associated difference spectra (SADS).

The aim of this precedure is to determine a model-based description of the behaviour of the system with precisely estimated parameters. This can be achieved by parametrising $c_i(t)$ using a kinetic model (target) and fitting the experimental data to this model by least square minimisation of χ^2:

$$\chi^2 = \sum_{\lambda,t} (\Delta\mathrm{A}_{\mathrm{exp}}(t,\lambda) - \Delta\mathrm{A}_{\mathrm{fit}}(t,\lambda))^2 \tag{3.4}$$

Within the scope of this study, two models were considered based on the potential mechanisms detailed above. Given that glycerol does not absorb in the visible and is in large excess, the hydrogen abstraction from glycerol can be described by a simple sequential model:

$$^1\mathrm{F}^* \longrightarrow {}^3\mathrm{F}^* \longrightarrow \mathrm{FH}^\bullet \longrightarrow \mathrm{P} \tag{3.5}$$

where P corresponds to a population sink representing the final products of the reaction at later times. The resulting SADS obtained using a Matlab-based toolbox, are shown

together with their respective lifetimes in Figure 3.5.[106] The SADS are in excellent agreement with the preliminary analysis conducted above and the reference spectra available in the literature, which suggests that the model chosen describes the behaviour of the system relatively well.[100]

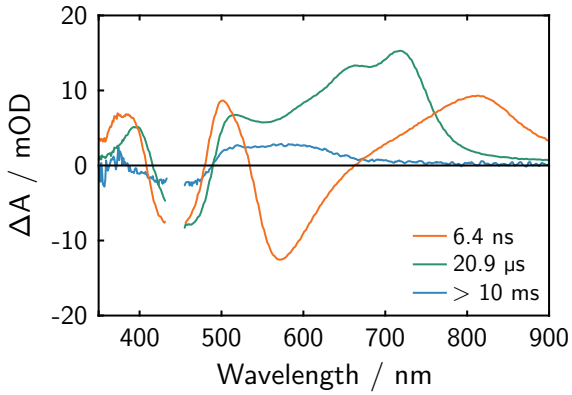


Figure 3.5: Species associated difference spectra obtained by global analysis with the hydrogen abstraction mechanism as a target and conducted using the 500 time points acquired by transient absorption.

The triplet-triplet annihilation was modelled as follows:

$$\begin{aligned} {}^1\mathrm{F}^* &\longrightarrow {}^3\mathrm{F}^* \\ 2\,{}^3\mathrm{F}^* &\longrightarrow \mathrm{FH}^\bullet \\ \mathrm{FH}^\bullet &\longrightarrow \mathrm{P} \end{aligned} \tag{3.6}$$

More complex models incorporating the formation of the initial anion-cation pair were also tested but this step could not be resolved with the time resolution used for this experiment. As displayed in Figure 3.6, the SADS obtained were very similar to those obtained for the hydrogen abstraction model. However, the third one also exhibited a negative feature at $\lambda > 650\,\mathrm{nm}$, most likely to compensate for the slower decay of the triplet state compared to the previous model. Given that the oxidised flavin does not absorb nor fluoresce in that region, this negative feature bears no physical meaning, which suggests that this model is not a good description of the system's behaviour.

Thus, the flavin semiquinone radical most likely stems from the abstraction of a hydrogen atom from glycerol. This is consistent with the observations of Hemmerich *et al.*, who hinted that this reaction might be dominant over triplet-triplet annihilation.[102]

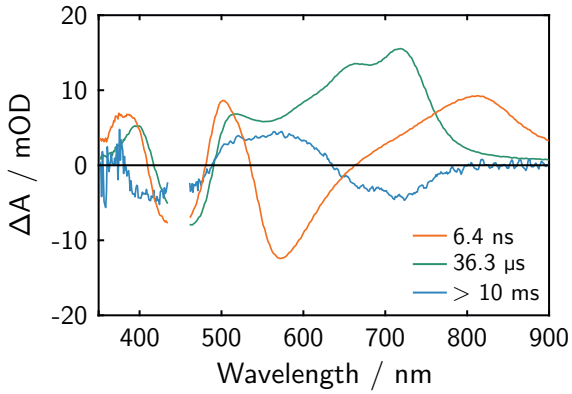


Figure 3.6: Species associated difference spectra obtained by global analysis with the triplet-triplet annihilation mechanism as a target and conducted using the 500 time points acquired by transient absorption.

Interestingly, Green and Tollin demonstrated that many hydroxylic solvents could react with the flavin and form $FMNH^{\bullet}$. Yet, the examination of FMN in solutions of ethanol and 1,2-propanediol revealed that the system is not magnetosensitive in these conditions. This suggests that the formation of the radical is not sufficient for a MFE to develop and that the high viscosity of glycerol might foster its development.[39,103]

3.4 Conclusion and outlook

This chapter demonstrated the existence of a previously unsuspected MFE measured in solutions of flavins in glycerol/water. Spectroscopic studies revealed that it originates from the presence of neutral flavin semiquinone radicals formed by hydrogen abstraction from glycerol, as determined by global target analysis of transient absorption data.

The existence of this magnetic field effect raised several concerns. First and foremost, the main issue regarding the flavin-glycerol MFE was its potential to undermine previous MFE measurements conducted on cryptochromes as all cryptochrome samples contain a small amount of free flavin molecules and are prepared in glycerol-containing buffers. Fortunately, MFE studies confirmed the triplet-born nature of the radical pair, hence reinforcing the validity of these cryptochrome data.

Further, it appears that the flavin-glycerol MFE requires relatively high flavin concentrations and excitation power to be detected and less sensitive experiments, such as the transient absorption apparatus, are not able to observe it. This suggests that its potential to distort the intrinsic MFE of cryptochromes is minimal as these samples are investigated

using low-power excitation and contain relatively small amounts of free flavin ($\sim 7\,\mu$M assuming 10% of the flavin absorption of a sample stems from free flavin molecules).[34]

Regarding the main objective of this thesis, the presence of this field effect is expected to have a relatively limited impact on the ability to measure anisotropic MFEs on cryptochromes in glycerol solutions. Indeed, as just explained, in cryptochrome solutions, under the experimental conditions used for these samples, the free flavin-glycerol MFE is largely dominated by that of the proteins themselves. Additionally, in the improbable scenario where the free flavin MFE actually contributed significantly to the overall MFE detected, it would most likely not exhibit any anisotropic MFE as the experimental conditions employed to immobilise cryptochromes would not be sufficient to effectively hinder the rotational diffusion of the free flavin molecules, as seen in the previous chapter.

Chapter 4

Detection of Magnetic Field Effects by Confocal Microscopy in flavin-lysozyme crystals

The detection of anisotropic magnetic field effects requires the creation of a population of oriented radicals with limited rotational mobility. As discussed above, this can be achieved by photoselection of an isotropic and immobilised sample or by direct molecular alignment. In Chapter 2, different rigid matrices were investigated as potential media to immobilise a radical pair. The systematic comparison of their properties highlighted glycerol solutions as the most promising option. However, the discovery of an unexpected magnetic field effect on the reaction of flavins in glycerol aqueous solutions, although its impact is expected to be relatively limited, calls for the investigation of possible alternative immobilisation strategies. Indeed, as discussed in Chapter 3, cryptochrome samples typically contain small amounts of free flavin whose reaction with the glycerol present in the buffer could distort the intrinsic protein MFE.

In this chapter, the study of MFEs in single protein crystals is explored. Although this immobilisation strategy is most fitting for the detection of anisotropic MFEs as proteins are highly ordered within the crystal lattice, it also comes with several challenges:

- Crystal growth. Depending on the protein to be crystallised, crystal growth can either be extremely trivial or a technical feat. Unfortunately, growing cryptochrome crystals seems to fall under the latter category. In particular, thus far, no one has ever been able to successfully crystallise cryptochromes from migratory birds.

- Experimental study of MFEs in crystals. As protein crystals have a very high solvent content (50% on average), they are very fragile, crush easily and cannot bear being dehydrated.[107] Thus, protein crystals are very difficult to handle and are best kept in their mother liquor (see below). In principle, their magnetosensitivity could be studied by prompt fluorescence MARY but the resulting data would then be a convolution of the MFEs steming from both crystal and solution, which would almost

be impossible to deconvolve. A technique that discriminate the fluorescence emitted by the crystals from that of the surrounding solution is, therefore, required for the investigation of MFEs in crystals.

A possible solution to the latter problem lies in the use of micoscopy techniques, which have previously been exploited to study MFEs in solutions. Dodson *et al.* first reported the use of total internal reflection fluorescence microscopy for the measurement of MFEs in extremely small volumes.[108] In the same year, Beardmore and co-workers demonstrated the remarkable sensitivity of a transient optical absorption detection (TOAD) microscope.[49] Widefield fluorescence microscopy was also employed by Kattnig *et al.* in the work that revealed the existence of enhanced MFEs.[40] These studies highlighted spatial resolution as one the main advantages of microscopic techniques over more traditional MFE experiments.

This chapter showcases confocal microscopy as a powerful technique for the elucidation of magnetic field effects in single protein crystals. Confocal microscopy is first introduced and its advantages over other microscopy techniques are discussed. The instrument is then characterised by measuring the MFEs of solutions of FMN-HEWL and a well-studied cryptochrome. Finally, these studies are extended to protein crystals and the viability of confocal microscopy for the detection of anisotropic magnetic field effects is discussed.

The work presented in this chapter was conducted in collaboration with Dr. Marcin Konolaczyk and Jamie Gravell and was recently published.[109] Some passages of text are quoted verbatim from the publication.

4.1 Experimental methods

4.1.1 Introduction to confocal microscopy

A brief introduction to the key concepts underlying laser-scanning confocal microscopy is given here. More details can, for instance, be found on the online learning platforms of most microscope manufacturers.[110–113]

Like all microscopy techniques, confocal microscopy allows to image a sample and render some of its smallest features visible. In conventional widefield microscopy, the whole sample is illuminated and a significant amount of fluorescence emitted by the sample below and above the objective focal plane is detected. Confocal microscopy differs from widefield microscopy by its ability to control the thickness of the optical slice being imaged. This

feature stems from the use of tightly focused light and the existence of a pinhole which blocks out-of-focus light. Within the scope of this chapter, this is crucially important as the pinhole allows to discriminate the fluorescence emitted by the crystal from that of the surrounding solution.

The core of the optical setup of a laser-scanning confocal microscope is depicted in Figure 4.1. A laser beam is reflected onto a dichroic mirror and tightly focused to a diffraction-limited spot within the sample by the objective lens. The resulting fluorescence emission is collected by the objective and focused onto a photomultiplier tube (PMT). The pinhole placed in the focal plane in front of the detector acts as a spatial filter and excludes fluorescence from above and below the focal plane being imaged. In order to create an image, the specific point of the sample onto which the excitation light is tightly focused is scanned in a raster pattern. This is achieved using a pair of scanning mirrors mounted on galvanometers.

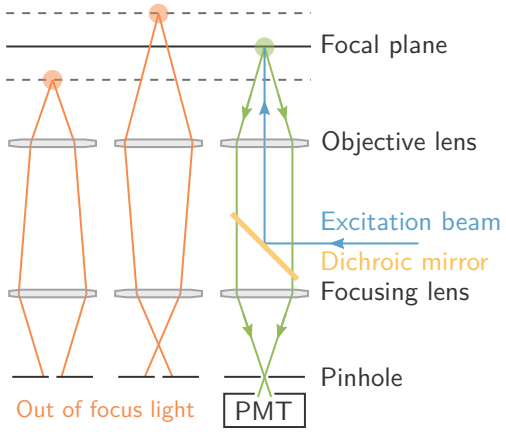


Figure 4.1: Principle of confocal microscopy. The fluorescence (in green) emitted from the focal place being imaged is detected by the photomultiplier tube (PMT) while out-of-focus fluorescence (in orange) is mostly cut out by a pinhole.

4.1.2 Apparatus

All the experiments presented in this chapter were carried out using an inverted Zeiss confocal microscope (LSM 5 Exciter). The sample was excited continuously at 458 nm through a 63× oil-immersion objective. A 475 nm long-pass filter was placed in front of the PMT to prevent scattered light from the excitation beam to reach the detector.

In order to measure magnetic field effects, a magnetic field was generated by a pair of home-built solenoids wound around ferrite cores mounted onto a custom-made sample stage. The applied field was switched alternately between 0 and 16 mT (with a rise time of ~70 ms) every few frames using a waveform generator (Rigol DG1022). Note that the internal clock of the LSM 5 Exciter could not be synchronised with that of the waveform generator but no appreciable dephasing between the field steps and the frames acquisition was observed over the course of the experiments presented below.

4.1.3 Data analysis

The data were acquired as a time stack of frames. The pixels in the region of interest (ROI) of each frame were averaged together and their intensity analysed over the course of the experiment. An example of time-resolved field-dependent fluorescence intensity averaged over all the pixels of the ROI is shown in Figure 4.2. The field-induced steps in the fluorescence decay curve can be easily distinguished (see insert in Figure 4.2, allowing the data to be split into field-on (in blue) and field-off (in orange) segments. A few data points were omitted at the edges of each segment to allow for minor timing uncertainties.

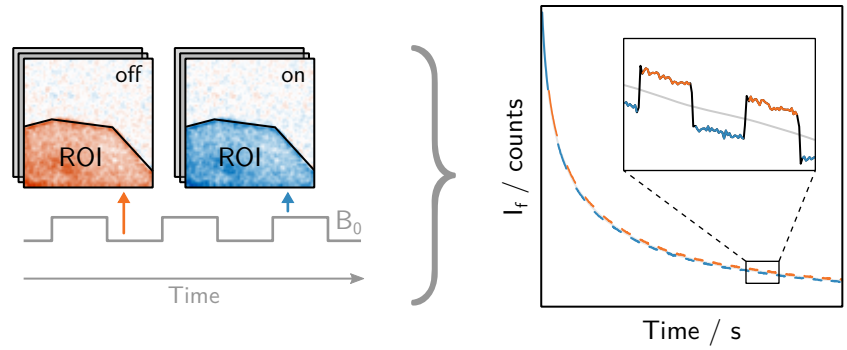


Figure 4.2: Methodology for the determination of the time-resolved field-dependent fluorescence intensity. For each frame, all the pixels in a chosen ROI are averaged together. In this case, the ROI corresponds to the location of the crystal. This allows to plot the average fluorescence intensity as a function of time. Field-on (in blue) and field-off (in orange) segments are clearly visible in the fluorescence trace (right panel). Here, the case of a triplet-born RP is displayed.

Like in all fluorescence-based experiments, the magnetic field effect is defined as the field-induced fractional change in the fluorescence intensity (MFE $= \Delta I_f / I_f(0)$). When measured by confocal microscopy, the MFE can be visualised at two different levels, as detailed in the following paragraphs.

Spatially-resolved %MFE averaged temporally

To obtain spatially-resolved %MFE, multiple small ROIs were considered. In this work, it was found that a 4×4 pixel bin was sufficient to detect MFEs of good quality. The average intensity of each ROI was then sliced into on/off segments in synchrony with the field steps. Each triplet of segments was then considered independently. As illustrated in the left panel of Figure 4.3, the outer segments were fitted with a quadratic function which was then used to interpolate the values of the central segment. This allowed ΔI_f and, in turn, the MFE to be determined as a function of time. Usually, the initial decay of the fluorescence intensity is too fast compared to the field switching to resolve the MFE in this region (like in the right panel of Figure 4.2). Therefore, these initial segments were discarded. The final %MFE value was obtained by averaging the MFE over a chosen period of time.

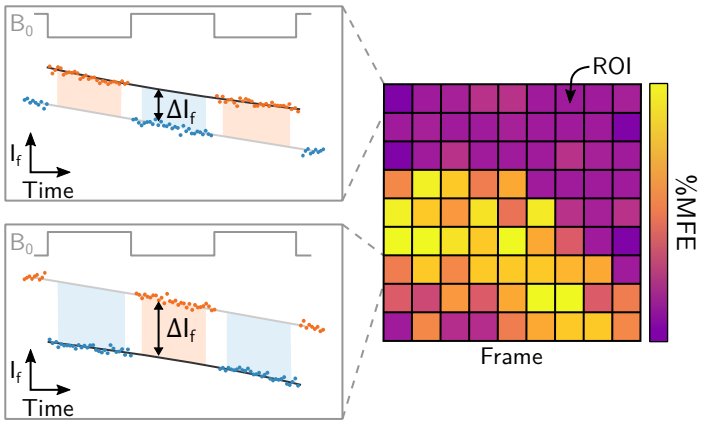


Figure 4.3: Methodology for the determination of spatially-resolved MFEs. The frame is split into multiple ROIs (right panel). For each ROI, the fluorescence intensity is split into on/off segments. The MFE of each segment is determined by fitting the surrounding segments with a quadratic function whose difference to the central segment is ΔI_f (left panel). The temporally-resolved MFE is obtained by repeating this process for all segments. The average MFE of the ROI is determined by averaging the temporally-resolved MFE over a multiple segments. Here, the case of a triplet-born RP is depicted.

%MFE averaged temporally and spatially

The average %MFE step was obtained by averaging over all the pixels in the ROI (the location of the crystal) and, once again, splitting them into on/off segments. As will be exemplified below, under certain conditions, the MFEs of some samples cannot simply be

represented by a step function and exhibit specific dynamics within individual field steps Thus, the method outlined above and used for spatially-resolved MFEs had to be adapted. The fluorescence baseline, which corresponds to the general field-independent decay of the fluorescence intensity, was first determined. As shown in the top panel of Figure 4.4, it is obtained from a smoothing interpolent through the baseline points (in green). The latter are determined from the centre points (in yellow) between each pair of on-off and off-on segments and are placed at the midpoint between subsequent centre points. The centre point between two consecutive segments is placed at the midpoint between the edges of the segments, which are determined by fitting both segments with quadratic functions and evaluating them at the edge. The obtained fluorescence baseline is shifted such that it coincides with the final points of the field-off segments, and is then used in place of the off data to calculate the time-resolved MFE. The average %MFE step over a field cycle is obtained by averaging the time-resolved MFE over multiple field steps. It is either fitted with a square wave or a piecewise single exponential.

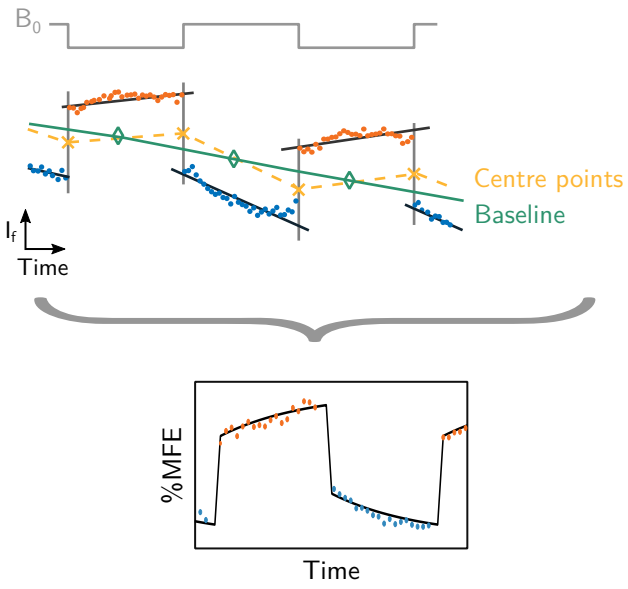


Figure 4.4: Methodology for the determination of the average MFE over a magnetic field cycle. The fluorescence baseline used for the calculation of the MFE is a smoothing interpolent through the baseline points (green diamonds), which are determined from the centre points between each pair of segments (yellow crosses). See main text for details. The baseline is shifted so that it coincides with the off segments, and used to obtain the time-resolved MFE. The overall MFE is determined by averaging the time-resolved MFE over multiple field steps.

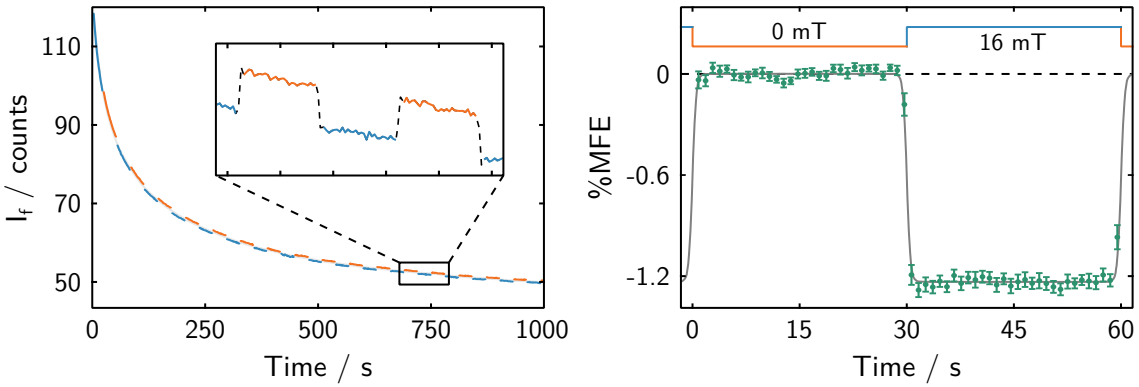
4.2 Results and discussion

4.2.1 Detection of magnetic field effects in solution

Before investigating MFEs in crystals, it is important to make sure that the LSM 5 Exciter confocal microscope yields results similar to previously reported data for solutions of particularly well-characterised systems. For this purpose, some of the investigations performed by Kattnig *et al.* were reproduced.[40] They constitute a relatively good benchmark even though they were carried out using a widefield fluorescence microscope and different data analysis protocols. The results outlined below will serve as an important reference point in the analysis of the crystal results discussed in the following section.

FMN-HEWL

The study of the magnetosensitivity of FMN-HEWL by confocal microscopy is presented in Figure 4.5a. The data shows the time-resolved fluorescence intensity of the sample. Here, as the sample is a uniform solution, the full frame was chosen as the ROI over which the fluorescence is averaged.



(a) Time-resolved fluorescence intensity after the onset of continuous illumination. The magnetic field was switched between 0 (orange segments) and 16 mT (blue segments) approximately every 30 s.

(b) %MFE averaged over 14 on-off steps. A square wave was fitted to the data to guide the eye.

Figure 4.5: Measurement of an aqueous solution of 10 μM FMN and 1 mM HEWL by confocal microscopy. The sample was excited at 458 nm with a laser power of 42 μW.

It is immediately apparent that the fluorescence decays quite substantially over the course of the experiment, which is due to the complex interplay between multiple phenomena:

- Photodegradation. As discussed in the previous chapters, flavins are particularly susceptible to photodegradation. More specifically, the main photoproduct of FMN is lumichrome. It absorbs very little at 458 nm ($\epsilon_{\mathrm{lch}}(458\,\mathrm{nm}) \simeq 430\,\mathrm{M^{-1}cm^{-1}}$ for lumichrome compared to $\epsilon_{\mathrm{FMN}}(458\,\mathrm{nm}) \simeq 11430\,\mathrm{M^{-1}cm^{-1}}$ for FMN) and its fluorescence quantum yield is one order of magnitude smaller than that of FMN.[22,23,114] Thus, over the course of the experiment, as FMN photodegrades, a less absorbing and less fluorescent species is formed, which causes the overall fluorescence of the sample to drop.

- Flavin diffusion. It is also a crucial factor at play here as the diffusion of fresh FMN into the irradiated region and of lumichrome and other photoproducts out of the illuminated area modulates the concentration of available FMN and, in turn, the measured fluorescence of the sample.

- Oxygen diffusion. The sample is exposed to air as only a small drop is pipetted onto a coverslip and no attempt at controlling the atmosphere was made, in part because oxygen plays a crucial role in the cryptochrome experiments presented later. The sample is, therefore, affected by triplet-triplet quenching (^{3}FMN-$^3O_2$) and, in turn, oxygen diffusion within the irradiated area.

As detailed above, the analysis protocols allow to uncouple the magnetosensitive behaviour from the general fluorescence decay. From the inset in Figure 4.5a, in which a triplet of off-on-off segments is highlighted, it is obvious that the system's fluorescence is modulated by the magnetic field. The observed decrease in fluorescence when the field is applied is expected of an intermolecular RP born in an initial triplet state like FMN-HEWL. The overall MFE averaged spatially over the whole frame and temporally over the course of the experiment (*i.e.* 14 on-off steps) is presented in Figure 4.5b. Its magnitude of $-1.25\,\%$ is in good agreement with the data measured by Kattnig *et al.* in a similar solution.[40]

Arabidopsis thaliana cryptochrome 1 (*At*Cry1)

Although several cryptochromes have been well characterised by absorption spectroscopy, measuring their magnetosensitivity by fluorescence has proven challenging. To date, there are only two reports of fluorescence-detected MFEs on cryptochromes, both by Evans, Kattnig and co-workers.[39,40] They both investigated a single cryptochrome, the cryptochrome 1

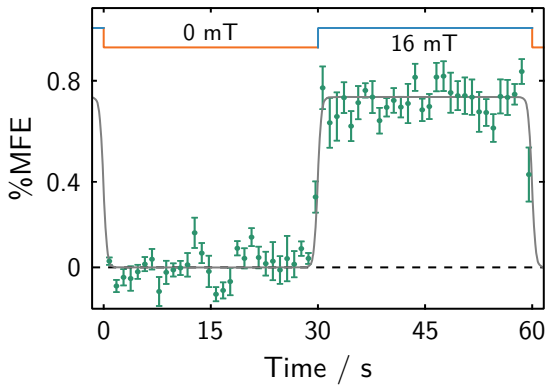


Figure 4.6: Average %MFE of *At*Cry1. The sample was excited at 458 nm with a laser power of 15 μW. An applied magnetic field was switched between 0 and 16 mT every ∼30 s. The data show an average of four on-off steps. A step function was fitted to the data to guide the eye.

from the plant *Arabidopsis thaliana* (*At*Cry1). These studies are highly significant as they firmly established fluorescence spectroscopy as a viable method for the detection of MFEs in these proteins. However, the quality of the *At*Cry1 data was inferior to that obtained for FMN-HEWL solutions. This system is, therefore, of particular interest within the scope of this chapter as it constitutes an excellent test to assess the capability of the apparatus to study more challenging samples.

*At*Cry1 was donated by Planet Biotechnology Inc., USA. The cryptochrome was prepared at a concentration of ∼75 mM in 50 mM Tris/HCl buffer (pH 7.0, 100 mM NaCl, ∼ 30% glycerol v/v). Potassium ferricyanide (2 mM) was employed to promote reoxidation of the flavin. In order to minimise protein degradation, the experiment was conducted at approximately 5°C using a water-cooled sample holder.

The average MFE of *At*Cry1 over an on-off step is depicted in Figure 4.6. As opposed to FMN-HEWL, switching the field off increases the fluorescence of *At*Cry1, giving rise to a positive MFE, which is expected for singlet-born RPs. The signal-to-noise ratio of the data is excellent, especially considering that only four on-off steps could be averaged as the sample photodegraded quite quickly after about 300 s. The resulting %MFE of -0.75% is larger than in Kattnig and Evans' previous reports.[39,40] This can be attributed to different illumination conditions as well as the presence of potassium ferricyanide. However, the smaller MFE observed for the cryptochrome sample compared to that of FMN-HEWL is consistent with previous works.

4.2.2 Detection of magnetic field effects in crystals

The data presented above demonstrated that confocal microscopy is a reliable technique for the measurement of MFEs in solution and yields comparable results to more traditional methods. In the second half of the chapter, these preliminary studies in solutions are expanded to single crystals. Due to the generally low availability of cryptochromes and how challenging crystallising them can be, cryptochrome crystals are not suited for methodology development. However, HEWL is readily available and relatively easy to crystallise under carefully optimised conditions (see below). As it is also part of one of the best characterised RP model systems, it is an ideal candidate for proof-of-principle studies on MFEs in single protein crystals.

Lysozyme crystal growth

The growth of high quality single FMN-doped lysozyme crystals is an imperative prerequisite for the investigation of their magnetosensitivity. Unfortunately, as highlighted in McPherson's excellent review, macromolecular crystallisation is a complicated process which is not well understood at a fundamental level and is mostly empirical.[107] Protein crystallisation relies on the creation of a supersaturated solution (or mother liquor), in which the protein exceeds the solubility limit but is nonetheless still present in solution under specific chemical and physical parameters. The system is then in a non-equilibrium state and the formation and development of a solid state allows the equilibrium to be re-established. Many combinations of experimental parameters will yield amorphous precipitates and successful crystallisation requires to carefully optimise experimental paramaters such as pH, precipitant (usually ionic salts) concentration, temperature and protein concentration. Crystallisation proceeds in two steps. It starts with nucleation, in which a small ordered cluster of proteins is formed in the mother liquor. The resulting nuclei subsequently grow in an ordered manner during the growth phase, giving rise to crystals. Both phenomena occur when the solution is supersaturated and are highly dependent on the solution characteristics, as illustrated by the phase diagram for crystal growth depicted in Figure 4.7, in which the adjustable paramater is usually the concentration of salt added to the solution but can also be pH or temperature.

The maximum solubility curve (thicker solid line) separates a region of undersaturation (region 1), in which the protein is soluble, from a region of supersaturation, which itself

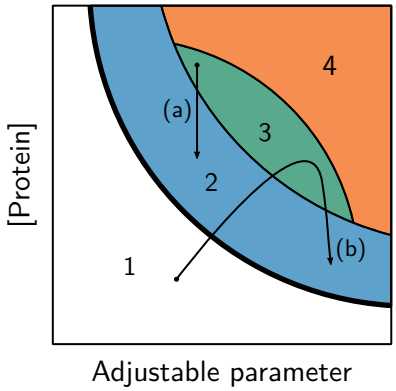


Figure 4.7: Protein crystallisation phase diagram. The adjustable parameter refers to any of the different experimental parameters that affects the state of the system: precipitant concentration, pH and temperature. Regions 1-4 correspond to the undersaturated, metastable, nucleation and precipitation zones, respectively. The thicker line denotes the border between the undersaturated and supersaturated zones. The paths followed by the two main crystallisation methods are represented: (a) batch method, (b) vapor diffusion. Adapted from [107] and [115]

comprises three sub-zones:

- The nucleation region (3) is characterised by the spontaneous formation of crystal nuclei.
- The metastable region (2), in which the nuclei develop into crystals.
- The precipitation region (4), at very high supersaturation, where the protein precipitates amorphously.

In order for nucleation and crystal growth to occur, the sample must reach supersaturation. This can be achieved in various ways, including the two most common ones, which are highlighted in Figure 4.7:

- Batch method (path a). The protein and salt solutions are mixed such that supersaturation conditions are immediately generated.
- Vapour diffusion (path b). A solution containing the protein below its solubility limit is placed on a coverslip inverted over a well (hanging drop) containing a precipitant solution at a higher concentration than the protein solution. Supersaturation is reached by vapour diffusion from the drop to the well solution, which leads to an increase in the protein and salt concentrations in the drop, hence moving the system to the nucleation zone.

In either case, once the system reaches the nucleation zone and crystals start growing,

the protein concentration in the mother liquor drops, hence moving the system to the metastable region, where crystal growth is fostered.

Both crystallisation techniques were investigated and successfully produced lysozyme crystals. However, crystallisation via the batch method was found to have a higher yield of crystals as well as shorter crystallisation times (one to two days) and was, therefore employed in this work. A protein solution (3.5 mM HEWL, 100 μM FMN) and a precipitant solution (1 M NaCl) were mixed in equal proportions. Both stock solutions were prepared in 0.1 M acetate buffer, pH = 4.2. In order to allow the sample to be easily imaged, 1 mL of the resulting solution was pipetted in a glass-bottom dish and stored in the dark at room temperature for a couple of days.

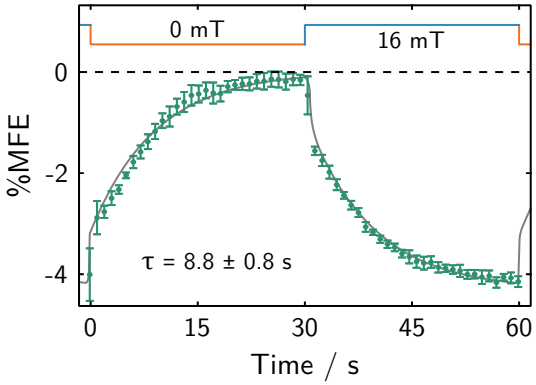
The integrity of the crystals was assessed by X-ray diffraction with a resolution of 1.5 Å, courtesy of Dr Kirsten Christensen (Chemistry Department X-ray crystallography facility). These studies allowed to confirm that the crystals were free of defects and not twinned (*i.e.* single crystals). They also determined that HEWL crystallised in the tetragonal space group P $4_3\,2_1\,2$, which is consistent with previous reports.[31] As shown in the table below, when grown in the presence of FMN, HEWL crystals exhibited an increased unit cell volume, indicating that the crystal structure expanded to incorporate the dopant. No additional difference from the FMN-free crystals was observed, suggesting that FMN is not ordered within the crystal. This is due to the existence of pores that allow the dye-containing solvent to diffuse through the crystal.[116]

	HEWL crystals	FMN-HEWL crystals
a-axis length / Å	76.776	78.776
b-axis length / Å	76.776	78.776
c-axis length / Å	36.99	37.09
Unit cell volume / Å^3	21 805	23 020

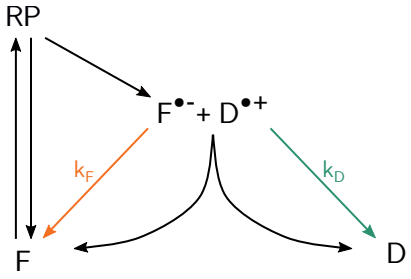
MFE measurements

%MFE averaged temporally and spectrally The overall MFE of an FMN-doped crystal is displayed in Figure 4.8. For this study, a relatively large crystal was selected so that it

occupied the whole field of view, which could, therefore, be used as the ROI. As confirmed by X-ray crystallography, FMN is not bound in this system but diffuses within the crystal. As a result, the system follows the same photocycle as in an FMN-HEWL solution with the radical pair formed in an initial triplet state, giving rise to a negative MFE.



(a) Average response of an FMN-HEWL crystal to a magnetic field cycle under continuous photoexcitation at 37 μW. The data show an average of five on-off steps. An exponential with a time constant τ was fitted to both parts of the field step to guide the eye.



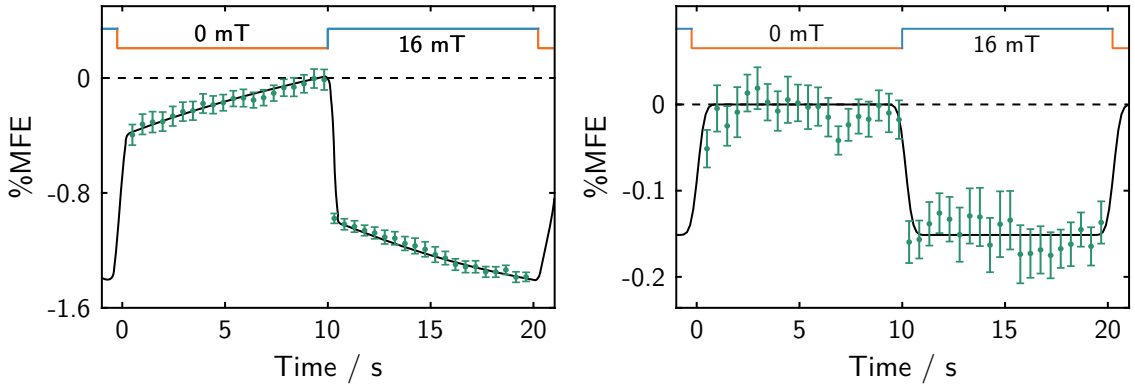
(b) Simplified RPM highlighting slow diffusion processes responsible for the development of EMFEs on a RP comprised of a flavin F and an electron donor D. The rate constants of the reactions responsible for the removal of the flavin and electron donor radicals are k_F and k_D, respectively. They occur in addition to the recombination of the radicals represented by the curved arrows.[40]

Figure 4.8: MFE on an FMN-doped HEWL crystal.

However, the shape of the MFE is quite different from that of an FMN-HEWL solution (Figure 4.5) as it exhibits biphasic kinetics characteristic of an enhanced MFE. Immediately after changing the magnetic field intensity, a prompt MFE develops. It is followed by a much slower phase, during which the MFE continues to rise with an exponential time constant $\tau = 8.8 \pm 0.8\,\mathrm{s}$, giving rise to a delayed MFE. These observations are consistent with the findings of Kattnig *et al.*, who first demonstrated the existence of enhanced MFEs (EMFEs).[40] The fast component is attributed to the attainment of a new steady state and the slower component results from the discrepancy between the termination rates of the two radical pair partners. The nature and magnitude of the EMFE have been shown to be linked to the ratio k_D/k_F, where $k_{D/F}$ is the rate of the termination reaction of the electron donor/the flavin (see Figure 4.8b and Introduction). Although a detailed quantification of k_D and k_F is not possible here due to the scanning nature of the microscope (as opposed to the widefield microscope used by Kattnig *et al.*[40]), the fact that the MFE is enhanced suggests that $k_D > k_F$. The termination rates are highly dependent on the experimental conditions. In particular, the viscosity of the solution plays a critical role and has been

proven to lead to an increase of k_D/k_F and, in turn, to an enhancement of the MFE.[39,53] Here, although the viscosity of the solvent is not, *per se*, different from that of an FMN-HEWL solution, the crystal matrix certainly constitutes a more hindered environment whose behaviour seems to be analogous to that of a locally viscous solution, hence giving rise to an enhanced MFE.

The impact of the presence of a crystal is more obvious when investigating the MFE of a crystal which does not occupy the whole field of view, as presented in Figure 4.9. In this case, the average %MFE can be measured for two different ROIs, one within the crystal (a), and one in the surrounding solution (b). As both regions are imaged together, all experimental parameters that could otherwise affect the nature of the EMFEs (*e.g.* laser power and scan rate) are identical for both ROIs. Yet, the MFE within the crystal is enhanced whilst that of the solution is not, which confirms that it is indeed the microenvironment of the RP within the crystal that induces the amplification of the MFE.



(a) Within the crystal.

(b) Within the mother liquor.

Figure 4.9: Average %MFE of an FMN-doped HEWL crystal and its mother liquor measured in two different ROIs. The magnetic field is switched between 0 and 16 mT approximately every 10 s.

FMN diffusion within lysozyme crystals The results presented above suggest that the immediate surrounding of the RP within the crystal is vastly different from within the mother liquor. A more thorough investigation of the diffusion of the flavin molecules within the crystal can be conducted using fluorescence recovery after photobleaching (FRAP). This technique, whose principle is described in Figure 4.10, consists in irradiating a small ROI at high power, hence irreversibly photobleaching the fluorophores in this region, and monitoring the subsequent recovery of the fluorescence.[117]

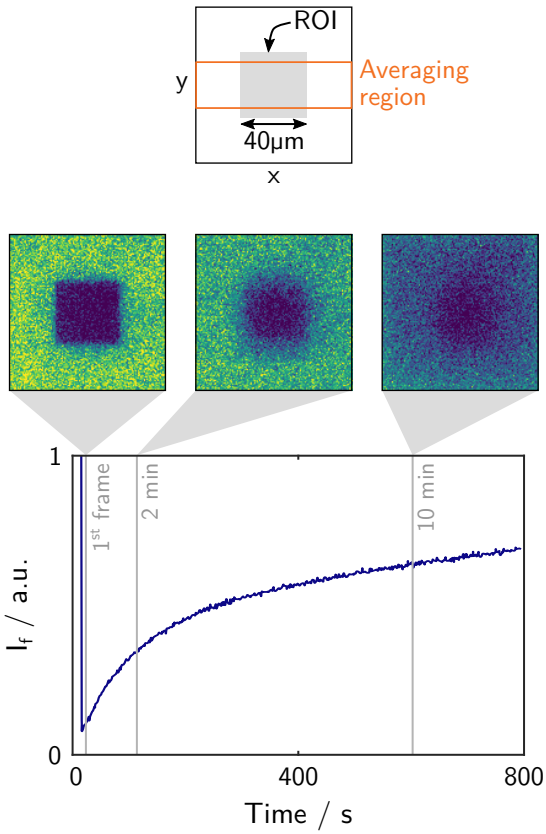


Figure 4.10: Top: Definition of the ROI bleached during the FRAP experiment and the averaging region used for data analysis (see main text for details). Middle: Fluorescence images of an FMN-HEWL crystal at different times after bleaching of an $40 \times 40\,\mu$m ROI for 5 s (from $t = 0$ s) with a 458 nm laser at 70 μW. Bottom: Recovery of the fluorescence intensity of the crystal over time. The fluorescence intensity was corrected for photobleaching of the whole frame and normalised to the intensity before bleaching.

Here, a 458 nm laser was employed at a power of 70 μW to bleach a $40{\times}40{\times}5\,\mu\text{m}^3$ region within a 101.8 μm wide frame for 5 s. This bleaching period was found to be sufficient to induce strong photobleaching while being short enough to minimise fluorophore diffusion. The fluorescence recovery was then monitored with the same laser at 0.9 μW. The initial high power illumination results in significant photobleaching and, in turn, a drop in the fluorescence intensity within the bleached ROI. A recovery of the fluorescence is then observed as fresh fluorophores diffuse into the ROI and bleached sample out of it. The spatiotemporal evolution of the fluorescence after bleaching allows to estimate the diffusion coefficient of the fluorophore within the bleached ROI. In principle, because lysozyme crystals are anisotropic environments, the diffusion coefficient of an FMN molecule within a crystal is described by a tensor.[118] The experimental and data analysis (see below) procedures employed here only provide an effective diffusion coefficient of the fluorophore

but this will suffice for the present discussion as the aim is to characterise the global diffusion of FMN within the crystal and compare it to that of FMN in water, which is isotropic. The fluorescence recovery curve is shown at the bottom of Figure 4.10. Note that it was corrected for the bleaching of the whole frame due to the monitoring laser, and normalised to the intensity of the frame before bleaching, as follows:

$$I_f(t) = \frac{I_b(t) + (I_{nb}(t=0) - I_{nb}(t))}{I_{nb}(t=0)} \tag{4.1}$$

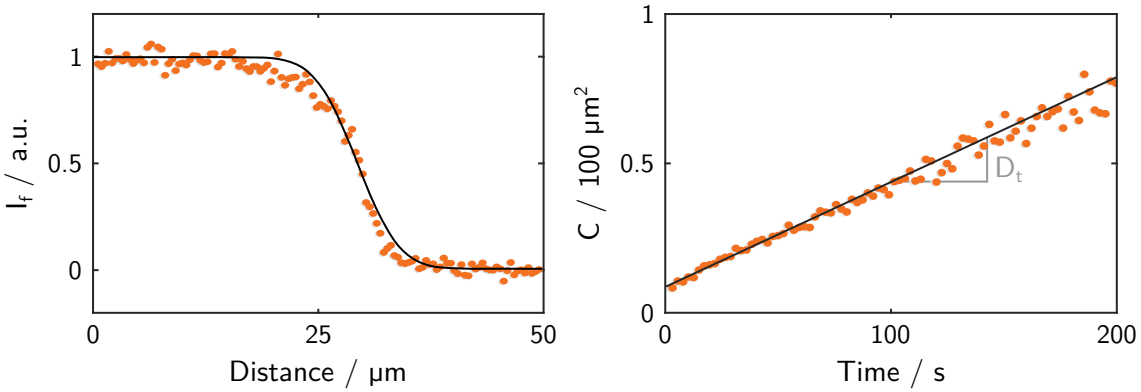
where I_b and I_{nb} denote the average fluorescence intensity inside and outside the bleached ROI, respectively.

The analysis of the FRAP data was conducted according to the method outlined by Aarts *et al.*[119] The intensity profiles along the x-axis at different times after bleaching were obtained by averaging over several pixels along the y-axis (orange region in the top panel of Figure 4.10). Both the left and right edges were then averaged together and normalised to the fluorescence intensity outside of the bleached ROI. The resulting normalised intensity profiles across the edge of the bleached area could be fitted relatively well with an error function:[120]

$$I(x,t) = \frac{1}{2}\left(1 - \mathrm{erf}\left(\frac{x - x_0}{2\sqrt{C}}\right)\right) , \tag{4.2}$$

where the width of the error function, C, is related to the translational diffusion coefficient, D_t, by $C = D_t t + b$. b accounts for broadening of the intensity profile mainly due to objective properties. The diffusion coefficient can then be determined by plotting the fitted C against time. A representative fluorescence profile across the edge of the bleached ROI as well as the evolution of C over time are presented in Figure 4.11.

After fitting C, a translational diffusion coefficient of D_t=3.4×10^{-13} m^{2}s^{-1} was obtained. This is in good agreement with data previously reported on fluorescein (a fluorescent probe of similar size and charge to FMN) in HEWL crystals where the diffusion coefficient was found to be between 0.53 and 1.90×10^{-13} m^{2}s^{-1} (depending on crystal direction).[118] Most importantly, D_t is three orders of magnitude smaller than the diffusion coefficient of FMN in water (5.57×10^{-10} m^{2}s^{-1}) determined by Tzedakis *et al.* by electrochemistry.[121] For such fast diffusion, FRAP cannot be employed as the fluorecence recovery is too fast compared to the time resolution of the experiment. This study confirms that the crystal effectively hinders the translational diffusion of the fluorophores, hence affecting the rates of the



(a) Error function fitted to the edge of the bleached ROI immediately after bleaching.

(b) Linear fit of the width of the error function, C. The gradient corresponds to the diffusion coefficient.

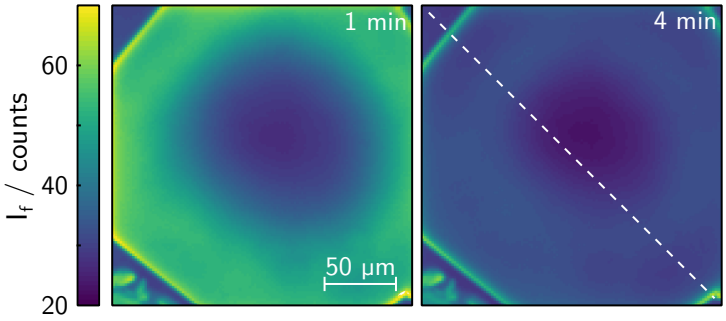
Figure 4.11: Extraction of the translational diffusion coefficient from FRAP data.

radical termination reactions, which explains the appearance of an enhanced MFE within the crystal as opposed to in solution.

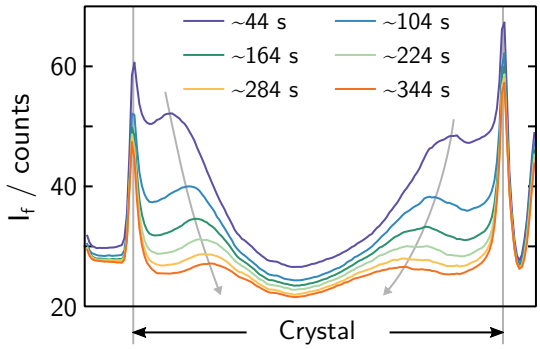
Spatially-resolved MFEs The previous paragraphs highlighted the different behaviours of the crystal and the mother liquor, hence demonstrating how powerful an imaging technique can be when investigating solid samples. These studies can be even more refined by considering smaller ROIs and conducting a fully spatially-resolved analysis of the fluorescence and magnetosensitivity of FMN-HEWL crystals.

The fluorescence images of an FMN-doped lysozyme crystal recorded during the first and the fourth minutes of the experiment are presented in Figure 4.12a. As already seen in the data presented above, the overall fluorescence intensity drops over time. This is attributed to photodegradation, which mainly forms lumichrome, a photoproduct that is essentially non-fluorescent when excited at 458 nm.[20,23] What is more surprising is that the fluorescence intensity is not uniform across the frame. In particular, the fluorescence intensities of the crystal and the surrounding solution are significantly different. Further, the fluorescence intensity is most intense at the edges of the crystal and drops towards the centre.

The first frame recorded at $t = 0\,\mathrm{s}$ is displayed in Figure 4.13 and highlights that the fluorescence of the crystal is much larger than that of the surrounding solution. This observation can be attributed to an increased local concentration of FMN within the crystal compared to the solution. This is due to the restrictive environment within the crystal, in



(a) Spatially-resolved fluorescence intensity at different times. Each picture correspond to an average over $\sim 60\,s$.



(b) Fluorescence intensity profiles across the crystal along the line indicated in (a) at different times. Each line corresponds to an average over $\sim 60\,s$. The grey vertical lines denote the edges of the crystal and the curved arrows highlight the wave-like motion of the secondary fluorescence maximum.

Figure 4.12: Spatially-resolved fluorescence of an FMN-doped HEWL crystal measured by confocal microscopy. The crystal was illuminated continously at 458 nm with a laser power of 37 μW.

which the flavin molecules diffuse through pores whose diameter is smaller than a nanometer, and to the attractive Coulomb force between HEWL and FMN.[116] Indeed, at pH 4.2, as depicted in Figure 4.14, the surface of HEWL, whose isolelectric point is 11.4, is positively charged. FMN interacts strongly with HEWL via its negatively charged phosphate group and has, therefore, a higher concentration within the tighly packed HEWL crystal than in the diluted protein solution.[30]

Figure 4.13 also shows that the fluorescence within the crystal is initially homogeneous. Thus, the bright edges that appear at later times are unlikely to be optical artefacts. Rather, their existence illustrates the discrepancy between the diffusion rates of FMN inside and outside the crystal.[122] As demonstrated by the FRAP study above, the diffusion coefficent within the crystal is three orders of magnitude smaller than in solution. Thus,

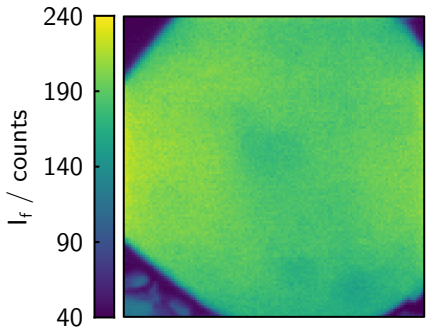


Figure 4.13: Fluorescence intensity image of the same crystal as in Figure 4.12 recorded at $t = 0\,\mathrm{s}$.

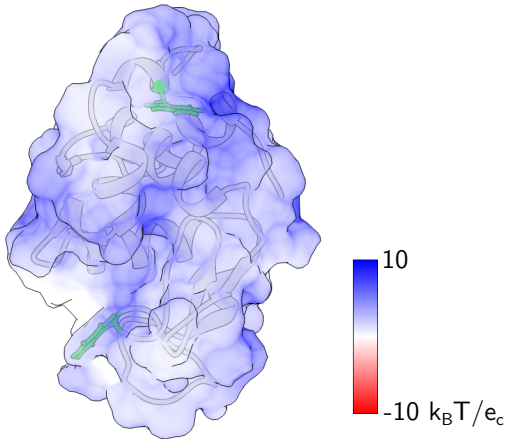


Figure 4.14: Electrostatic potential of HEWL calculated with an adaptive Poisson-Boltzmann solver at pH 4.2 and drawn with Chimera.[27] The tryptophan residues involved in the radical pair mechanism (in green) are located in a positively charged region (mainly due to lysine and arginine residues), fostering the interaction between the flavin (via the negatively charged phosphate group) and HEWL.

while photobleaching degrades FMN within the solution and the crystal indiscriminately, the edges of the crystal are continuously replenished by fresh FMN diffusing rapidly through the solution to the positively charged crystal surface. On the other hand, the much slower diffusion within the crystal makes the replenishment of FMN less efficient and leads to significant photodegradation and a subsequent fluorescence decrease inside the crystal.

A more detailed report of the temporal evolution of the fluorescence over time can be seen in Figure 4.15. It accentuates what was already suggested by the image of the crystal in Figure 4.12 recorded at $t = 4\,\mathrm{min}$: at later times, the fluorescence profile within the crystal in not a simple gradient decreasing continuously from the edges towards the center of the crystal. Rather, it exhibits a secondary maximum which manifests itself on the pictures as a more intense inner ring that seems to advance towards the center of the

crystal in a wave-like motion. This is particularly visible in Figure 4.12b, in which the fluorescence profile of the crystal along a diagonal slice is presented at different times.

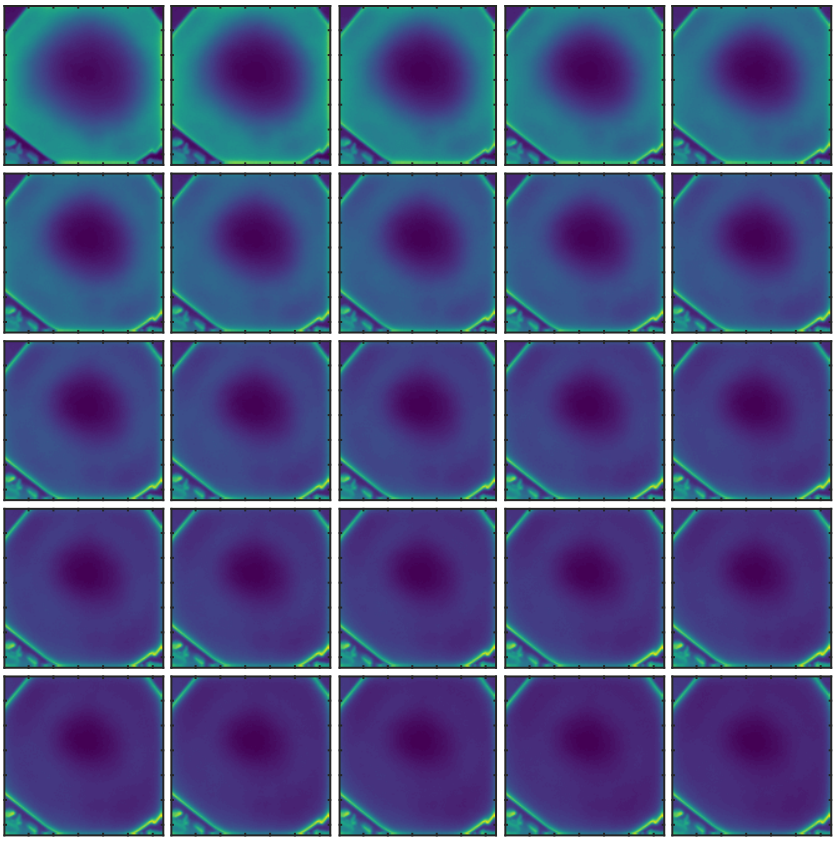


Figure 4.15: Average fluorescence intensity images of the same crystal as in Figure 4.12. Each image is an average over approximately 17s from time $t \sim$36 s to $t \sim$450 s.

The origin of this inner ring is so far elusive but it is visible in all the flavin-doped HEWL crystals examined. It is important to note that, while diffusion most likely contributes to the formation of the ring, it cannot account for it alone as it is a purely dispersive phenomenon. In order to get some insight into the underlying mechanism at play here, similar studies were conducted on a variety of dyes. More photostable dyes, such as fluorescein, did not exhibit such a behaviour, which suggests that photobleaching plays a critical role in the development of these features. Further, McPherson established that the interaction between flavins and HEWL was abnormally strong by comparing the rate of dye penetration into initially undyed crystals.[123] This prompted the investigation of fluorophores interacting more weakly with HEWL, such as acridine yellow, which is not charged at pH 4.2. Once again, as clearly seen in Figure 4.16, no secondary maximum is visible. Thus, it seems that the development of this more intense inner ring is due to a

combination of photodegradation and strong dye-crystal attractive interactions.

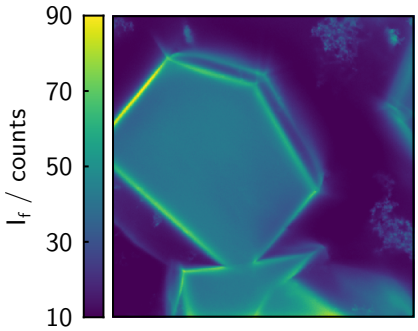
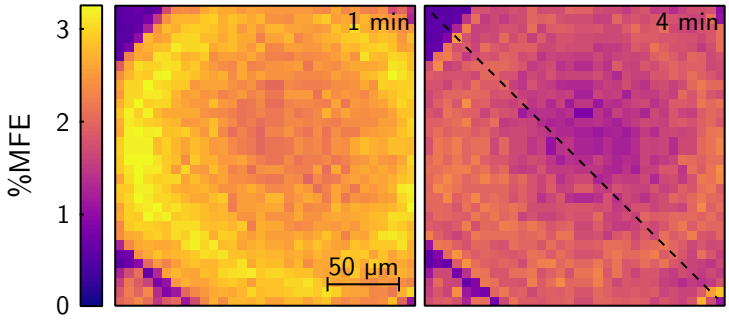
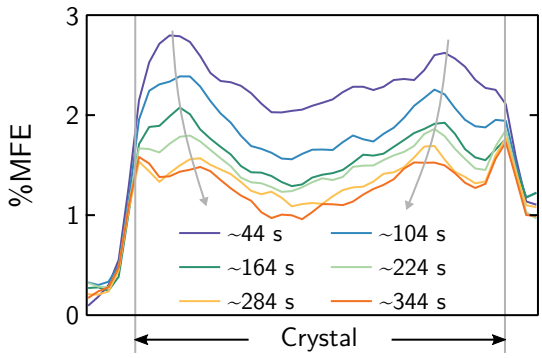


Figure 4.16: Fluorescence intensity image of a HEWL crystal doped with acridine yellow 4 min after the onset of continuous illumination at 448 nm. The data was acquired using a Leica confocal microscope (also employed in Chapter 5) and corresponds to an average over ~ 60 s.

Most importantly, the temporal evolution of the MFE, which can be seen in Figure 4.17 and, in more detail, in Figure 4.18, also seems to depend quite strongly on both the time of observation and the position within the crystal. The MFE profile is somewhat similar to that of the fluorescence. Although the sharp features at the edges of the crystal are missing, the MFE is most intense close to the edge, where the secondary maximum of the fluorescence was observed. The effect of diffusion on MFEs is relatively complex. On the one hand, fluorescence-detected MFEs are concentration-dependent and are, therefore, suppressed when photobleaching becomes dominant under slow diffusion conditions. On the other hand, slower diffusion also leads to an increase in the RP lifetime and, in turn, in the observed MFE.[39,40] Thus, because photobleaching is too intense in the centre of the crystal and diffusion is prohibitevely rapid at the edges, the field effect is most intense in an intermediate region near the crystal-solution interface.



(a) Time-averaged spatially-resolved %MFE. Left $t = 1\,\text{min}$, right $t = 4\,\text{min}$. Each picture corresponds to an average over $\sim 60\,\text{s}$.



(b) MFE profiles across the crystal along the line indicated in (a) at different times. Each line corresponds to an average over $\sim 60\,\text{s}$. The grey vertical lines denote the edges of the crystal and the curved arrows highlight the wave-like motion of the secondary MFE maximum.

Figure 4.17: Spatially-resolved MFE at 16 mT on an FMN-doped HEWL crystal measured by confocal microscopy. The crystal is the same as in Figure 4.12.

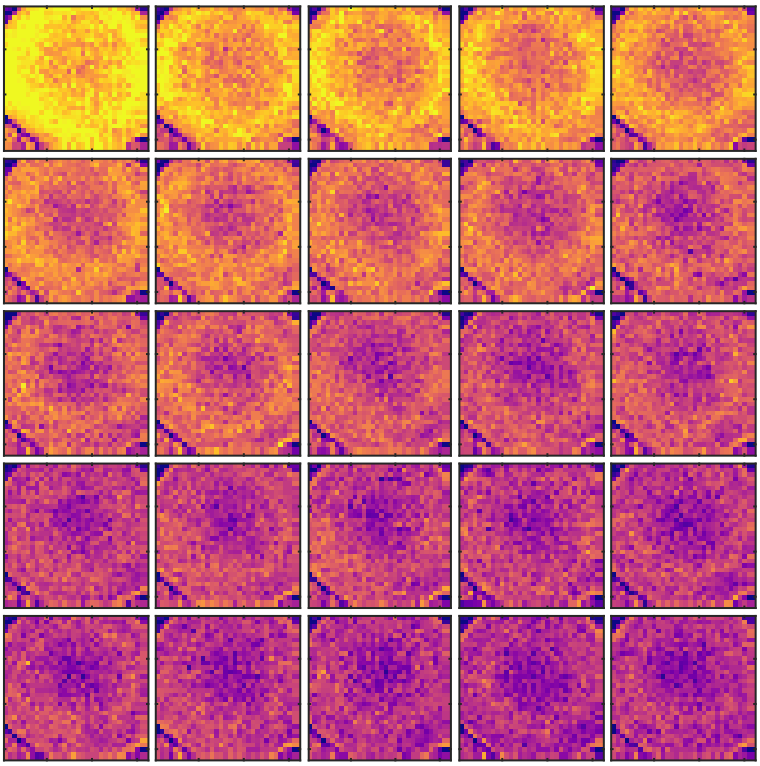


Figure 4.18: Average %MFE images of the same crystal as in Figure 4.17. Each image is an average over approximately 17s from time t ∼36 s to t ∼450 s.

4.3 Conclusion and outlook

This chapter demonstrated the power of confocal microscopy for the investigation of magnetic field effects, not only in solutions, but also in solid samples such as single crystals, owing to the ability of confocal imaging to image a thin focal plane by rejecting out-of-focus fluorescence.

This feature of confocal microscopy was fully utilised for the study of FMN-doped HEWL crystals, which showed that the technique offers a wealth of information compared to more traditional methods presently employed for MFE studies. In particular, it allows to examine the spatiotemporal evolution of magnetic field effects, which highlighted the roles played by photodegradation and diffusion. Although photobleaching and specific interactions between the dye and the crystal are likely to be involved, the previously unsuspected evolution of the field effect within FMN-doped crystals remains poorly understood and will require further examination.

These proof-of-principles studies of inhomogeneous systems open the way for a wider

variety of samples, especially biological systems such as cryptochrome-containing cells and tissues, for which spatial resolution is crucially important.

Regarding the wider scope of this thesis, and although FMN-HEWL crystals were merely employed here as a tool for methodology development, it is worth noting that, while lysozyme crystals do hinder the diffusion of the flavin molecules, the degree of immobilisation provided, as determined by FRAP, is not sufficient to give rise to anisotropic MFEs. However, considering the successful study of crystals as well as the excellent quality of the *At*Cry1 data, which demonstrated that confocal microscopy has the necessary sensitivity to probe magnetosensitive reactions in cryptochromes, the measurement of anisotropic MFEs in cryptochromes is becoming more attainable. Both single crystals of cryptochromes and photoselectively-excited, immobilised cryptochrome samples are attractive targets for these investigations.

Chapter 5

Isotropic and Anisotropic Magnetic Field Effects in Cryptochromes

The magnetosensitivity of cryptochromes have hitherto been mostly examined by absorption-based techniques as they provide crucial mechanistical information.[26,34,36,37] Fluorescence-based methods, on the other hand, are most suitable for the investigation of the possible mechanism of MFE amplification which was first reported by Kattnig and co-workers.[40] Crucially, these so-called enhanced MFEs have been suggested to play a key role in the implementation of the putative cryptochrome-based magnetic compass sense. So far, only *At*Cry1, a plant cryptochrome, has been shown to exhibit significant MFE amplification under conditions of continuous photoexcitation. In this chapter, a variety of cryptochromes are investigated. Beyond the plant cryptochrome originally studied, animal cryptochromes, including cryptochromes sourced from both migratory and non-migratory birds, are also considered. Further, the nature of the amplification and its dependence on experimental conditions are examined in more detail.

In Chapter 4, MFEs were successfully measured in cryptochromes and protein single crystals using confocal microscopy. Building upon these achievements, and motivated by their potential implication for the viability of the cryptochrome-based compass, the magnetosensitivity of cryptochrome single crystals is presented in the second part of this chapter.

5.1 Isotropic magnetic field effects in cryptochromes

The proteins examined, as well as their binomial nomenclature, are listed in the table below.

Protein name	Binomial nomenclature	Common name
*At*Cry1	*Arabidopsis thaliana*	Thale cress
*Dm*Cry	*Drosophila melanogaster*	Fruit fly
*Er*Cry4	*Erithacus rubecula*	European robin
*Cl*Cry4	*Columba livia*	Pigeon

All FAD-containing cryptochromes are subject to the radical pair mechanism described in detail in the Introduction. Following photoexcitation, a primary radical pair, RP_1 = $[FAD^{\bullet -} - TrpH^{\bullet}]$ is quickly formed via a series of electron transfers along a chain of tryptophan residues. It is then stabilised by the formation of a longer-lived secondary radical pair, RP_2. In spite of these similarities, some key differences exist between plant and animal cryptochromes. The most important distinction is the existence of an extended electron transfer pathway for animal cryptochromes, with the addition of a fourth tryptophan residue to the conserved tryptophan triad.[25] Another difference is the protonation state of the radicals in RP_2, which depends on the nature of the amino acid directly adjacent to the N5 position of the FAD ring.[26,124] Thus, in the animal cryptochromes investigated here, $RP_2 = [FAD^{\bullet -} - Trp^{\bullet}]$, whereas in *At*Cry1, $RP_2 = [FADH^{\bullet} - Trp^{\bullet}]$.[34]

The difference in the electron transfer pathways of plant and animal cryptochromes prompted the examination of the individual roles of the different tryptophans via site-specific mutation. The four tryptophans are refered to as Trp_X with X = A, B, C or D. Trp_A is the closest residue to the flavin cofactor, and Trp_D is the farthest. The corresponding mutants, in which Trp_X is replaced by a redox-inactive phenylalanine, are termed Trp_X mutants.

The data presented in this section were recorded in collaboration with Jamie Gravell.

5.1.1 Methods

Materials

*Dm*Cry was recombinantly expressed in *E. coli* by the groups of Prof. Stefan Weber and Prof. Erik Schleicher (University of Freiburg, Germany). The *Drosophila* samples were prepared in 50 mM HEPES buffer (pH 7.0, 100 mM NaCl, 20% (v/v) glycerol).[25]

The avian cryptochromes were provided by the lab of Prof. Henrik Mouritsen (University of Oldenburg, Germany). In both cases, a 20 mM Tris buffer (pH 8.0, 200 mM NaCl, 20% v/v glycerol) was used.

*At*Cry1 was donated by Planet Biotechnology Inc. and prepared in 50 mM Tris/HCl buffer (pH 7.0, 100 mM NaCl). For consistency, the glycerol content was lowered to 20% by volume as opposed to 30% like in the previous chapter.

In all cases, the quality of the sample was assessed by UV-vis spectroscopy, which allowed to detect the presence of partially and fully reduced flavin or significant scattering stemming from aggregated proteins. The sample was then either reoxidised with potassium ferricyanide or centrifuged accordingly. The concentration of the sample was adjusted using UV-vis spectroscopy to 0.6 OD at 450 nm ($\sim$50 μM). Finally, 2 mM of ferricyanide were added to promote the reoxidation of the sample during the experiment.

Apparatus

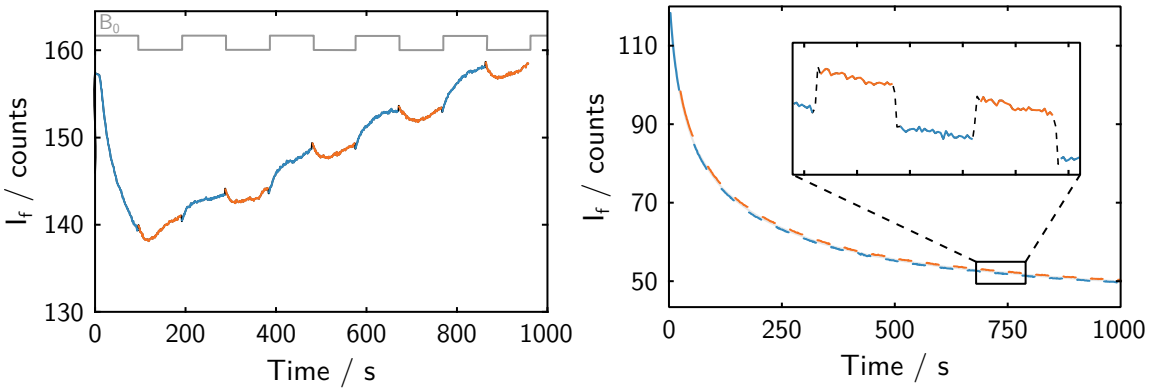
Spurred by the excellent data presented in Chapter 4, a new confocal microscope, a Leica SP8 microscope, was purchased. As opposed to the Zeiss one used in the previous chapter, the Leica microscope comprises, among other features, a trigger unit, which allows the magnetic field and the frames acquisition to be fully synchronised, hence removing any timing uncertainty. Additionally, the detection wavelength range is not simply controlled by a single long-pass filter anymore but can, instead, be precisely defined. Unless otherwise stated, the fluorescence of the sample was recorded between 475 and 645 nm.

Beyond these upgrades, the general principle of the experiment remains the same as described in Chapter 4. A 15 μL drop of the sample is illuminated at 448 nm and its fluorescence is detected simultaneously with an external magnetic field being switched between 0 and 16 mT every 100 frames (a frame is acquired every 959 ms). The data analysis procedure was identical to that outlined in Chapter 4.

5.1.2 Results and discussion

Competition between fluorophores

***At*Cry1** The time-resolved fluorescence intensity of *At*Cry1 is presented in Figure 5.1a. As before, the field-on and field-off segments are displayed in blue and orange, respectively. Before examining the magnetosensitive behaviour of the system, a striking difference from the FMN-HEWL data presented in Chapter 4 (and reproduced in Figure 5.1b for easier comparison) is immediately obvious. Whilst the fluorescence intensity of FMN-HEWL was globally decreasing over the course of the experiment, here, it is increasing following an initial decay and eventually becomes larger than the fluorescence at $t = 0\,\mathrm{s}$.



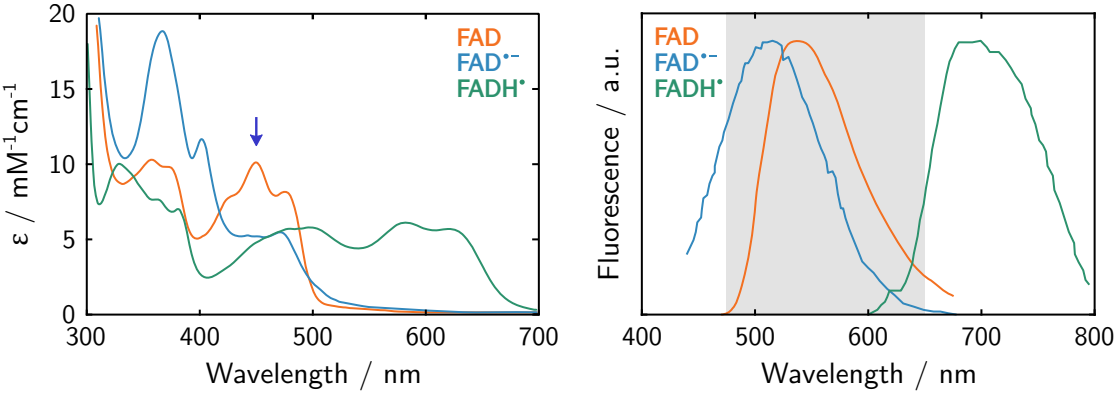
(a) *At*Cry1 solution measured with an excitation power of 36 μW.

(b) Solution of 10 μM FMN and 1 mM HEWL. Reproduced from Chapter 4 for easier comparison.

Figure 5.1: Comparison of the temporal evolution of the fluorescence intensity of a cryptochrome compared to a model system. The magnetic field is switched between 0 (orange segments) and 16 mT (blue segments) every few frames.

Such a behaviour can only be explained by the formation of another fluorescent species which is more fluorescent than FAD and is accumulating over the course of the experiment. Based on the relative rates of the different processes involved in the radical pair mechanism, Evans and co-workers established that, under conditions of continuous photoexcitation, the system could be relatively well described by a two-state model.[39] Indeed, the steady-state concentrations of the ground state (GS) and RP_2 vastly exceed those of the other species involved such that $[F - Trp]_{tot} \approx [F - Trp]_{GS} + [RP_2]$. Thus, RP_2 is the only species formed which is accumulating over the course of the experiment. Although relatively little attention has been paid to the study of the fluorescence of cryptochromes, the work of Kao *et al.* demonstrated that FAD in its semiquinone form is also fluorescent.[104] The absorp-

tion and fluorescence of a protein-bound FAD in its different redox states are depicted in Figure 5.2.



(a) Absorption spectra. The excitation wavelength used for the MFE experiments is indicated by the arrow. Reproduced from Liu *et al.*[125]

(b) Normalised fluorescence spectra. The detection region used for the MFE experiments is indicated by the shaded area. Reproduced from Kao *et al.*[104]

Figure 5.2: Photophysical characteristics of protein-bound FAD in different redox states.

Whilst the fluorescence quantum yields of flavin radicals have never been determined quantitatively, the work of Kao and co-workers suggests that the radicals' fluorescence is weak compared to that of FAD in its oxidised form.[104] Considering that the absorbance of $FADH^{\bullet}$ at 448 nm is also much weaker than that of FAD, and that the fluorescence detection window (475-645 nm) only partially overlaps with its fluorescence spectrum, it is unlikely that the formation of the radical could lead to such an increase of the overall fluorescence intensity.

An alternate explanation could be the presence of free flavin molecules. As mentioned previously, most protein samples contain some amount of unbound flavin. Additionally, upon photoexcitation, some proteins might degrade and misfold, leading to a subsequent release of the flavin cofactor. For absorption-based experiments, this phenomenon manifests as the formation of protein aggregates and a resulting rise in scattering. In the case of fluorescence spectroscopy, because the fluorescence quantum yield of free flavin is two orders of magnitude larger than that of bound flavin, the release of even an extremely small quantity of flavin can give rise to a substantial increase in the fluorescence intensity.[22]

The average MFE of *At*Cry1 over one magnetic field step is displayed in Figure 5.3. As expected of a singlet-born radical pair, the sample exhibits a positive MFE. Interestingly, a small prompt negative MFE is also visible immediately after the field change. It has been previously attributed to the reaction of a small amount of unbound flavin with the solvent accessible tryptophan residues on the surface of the protein.[40] In light of Chapter 3, it

is also possible that the flavin/glycerol magnetic field effect could be at play here even though it is expected to be very small in these conditions. The cryptochrome MFE is initially obscured by this secondary MFE but eventually overcomes it, giving rise to a large positive EMFE at longer times.

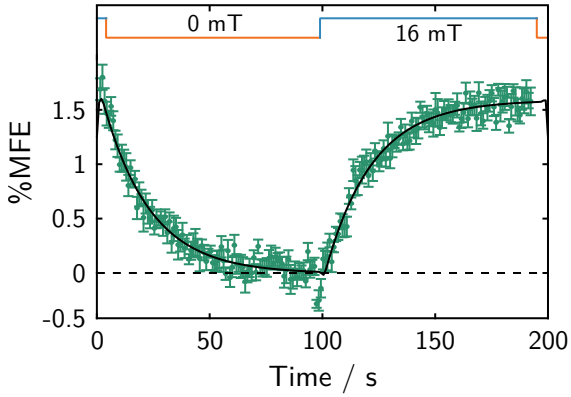


Figure 5.3: Average response of an *At*Cry1 solution to one magnetic field cycle. The excitation power was 36 μW.

At 36 μW, the sample exhibits a very clear enhanced MFE with a time constant of $\tau = 14.4\,\mathrm{s}$. Note that the amplification phenomenon is much slower here compared to the data measured by Kattnig *et al.* ($\tau = 3.4\,\mathrm{s}$).[40] This is due to the vastly different illumination conditions. As explained above, as opposed to widefield microscopy, confocal microscopy uses very tightly focused light and, therefore, does not illuminate the whole sample continuously. Rather, each frame corresponds to a scan of the field-of-view following a raster pattern. The sample is, strictly speaking, not photoexcited continuously, effectively rendering the overall dynamics of the system much slower.

***Dm*Cry $\mathbf{Trp_D}$ mutant** Similar studies were carried out on the *Dm*Cry $\mathrm{Trp_D}$ mutant. Its time-resolved fluorescence intensity is presented in Figure 5.4. Similar to *At*Cry1, the fluorescence increases over the course of the experiment due to the degradation of a small fraction of the proteins and the subsequent release of the flavin cofactor.

Surprisingly, the average MFE over a single field step, which is displayed in Figure 5.5 for several excitation powers, differs significantly from that of *At*Cry1. In particular, the shape of the MFE step at 24 μW is quite peculiar. Like in *At*Cry1, it exhibits a biphasic behaviour, with the prompt and the delayed components being of opposite signs but, here, the prompt MFE is positive and the enhanced MFE is negative. Because it is positive, the short component cannot be attributed to the presence of free flavin and, therefore, stems

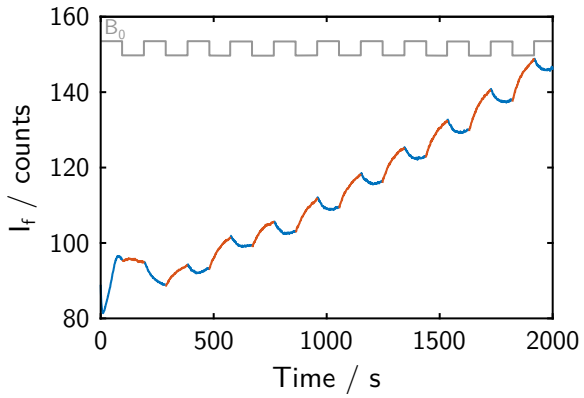


Figure 5.4: Fluorescence intensity of a solution of *Dm*Cry Trp_D mutant as a function of time. The magnetic field is switched between 0 (orange segments) and 16 mT (blue segments) approximately every 100 s. The excitation power was 49 μW.

from the usual fluorescence of the flavin singlet excited state within the proteins.

The origin of the enhanced MFE is less clear. Of course, because it is negative, one could think that it could be attributed to free flavin. This MFE could stem from the reaction of FAD with either glycerol or surface residues of the protein. However, under these conditions (*i.e.* low excitation power and low glycerol content) and as discussed in Chapter 3, the flavin-glycerol MFE would essentially not be visible by confocal microscopy. Further, the MFE involving a surface residue would, in principle, be analogous to that of FMN and HEWL and, therefore, as seen in the previous chapter, would not be expected to exhibit a significant enhanced MFE under these experimental conditions. This was confirmed by the measurement of the MFE of a solution of FMN-HEWL prepared in a cryptochrome buffer, which clearly exhibits no amplification, as shown in Figure 5.6. It is, therefore, improbable that free flavin could give rise to the MFE amplification observed in *Dm*Cry Trp_D mutant.

Similar to $FADH^{\bullet}$ in *At*Cry1, the $FAD^{\bullet-}$ radical formed in *Dm*Cry is also weakly fluorescent, but its fluorescence spectrum coincides significantly better with the detection window (see Figure 5.2).[104] Thus, the contribution of the flavin radical in RP_2 to the overall fluorescence of the system is expected to be much larger than in the plant cryptochrome. Because RP_2 is formed downstream from the magnetosensitive step in the radical pair mechanism, its response to a magnetic field is expected to be opposite to that of FAD, which is upstream from the singlet-triplet mixing step. Therefore, if the radical concentration is larger than that of FAD such that its contribution to the overall fluorescence of the system becomes dominant, the resulting MFE will be negative, as observed here.

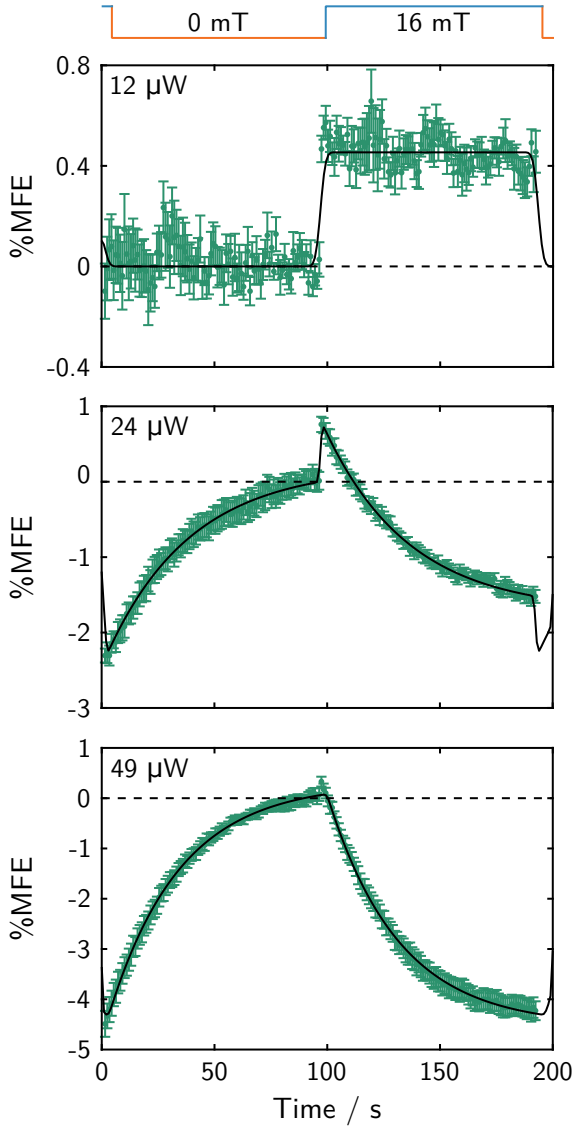


Figure 5.5: Average response of a solution of *Dm*Cry Trp_D mutant to one magnetic field cycle at different excitation powers, which are indicated in the top-left corner of each graph.

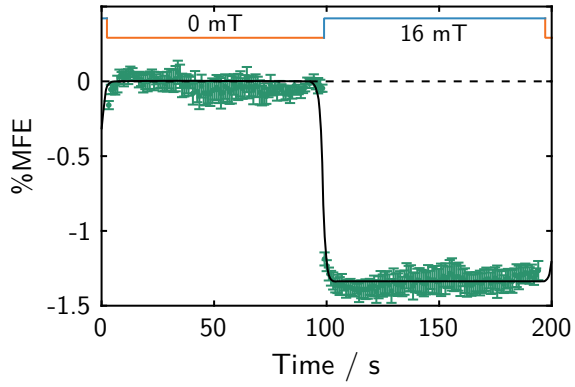


Figure 5.6: MFE of a solution of FMN-HEWL in Tris buffer (20% glycerol).

Following an approach analogous to that presented by Murakami *et al.* and later employed by Kattnig and co-workers, the ground state and RP_2 concentrations can be determined by examining the temporal evolution of the system which, based on Figure 5.7, is described by the following rate equations:[40,97]

$$\frac{d[\mathrm{F}-\mathrm{Trp}]}{dt} = -k_{\mathrm{EX}}[\mathrm{F}-\mathrm{Trp}] + k_{\mathrm{DS}}[^1\mathrm{F}^*-\mathrm{Trp}] + k_{\mathrm{BET}_1}[\mathrm{S}] + k_{\mathrm{BET}_2}[\mathrm{RP}_2] \tag{5.1a}$$

$$\frac{d[^1\mathrm{F}^*-\mathrm{Trp}]}{dt} = k_{\mathrm{EX}}[\mathrm{F}-\mathrm{Trp}] - (k_{\mathrm{ET}}+k_{\mathrm{DS}})[^1\mathrm{F}^*-\mathrm{Trp}] \tag{5.1b}$$

$$\frac{d[\mathrm{S}]}{dt} = k_{\mathrm{ET}}[^1\mathrm{F}^*-\mathrm{Trp}] - (3k_{\mathrm{HF}}+k_{\mathrm{BET}_1}+k_{\mathrm{RP}_2})[\mathrm{S}] + k_{\mathrm{HF}}([\mathrm{T}_0]+[\mathrm{T}_+]+[\mathrm{T}_-]) \tag{5.1c}$$

$$\frac{d[\mathrm{T}_0]}{dt} = -(3k_{\mathrm{HF}}+k_{\mathrm{RP}_2})[\mathrm{T}_0] + k_{\mathrm{HF}}([\mathrm{S}]+[\mathrm{T}_+]+[\mathrm{T}_-]) \tag{5.1d}$$

$$\frac{d[\mathrm{T}_+]}{dt} = -(2k_{\mathrm{HF}}+k_{\mathrm{RP}_2})[\mathrm{T}_+] + k_{\mathrm{HF}}([\mathrm{S}]+[\mathrm{T}_0]) \tag{5.1e}$$

$$\frac{d[\mathrm{T}_-]}{dt} = -(2k_{\mathrm{HF}}+k_{\mathrm{RP}_2})[\mathrm{T}_-] + k_{\mathrm{HF}}([\mathrm{S}]+[\mathrm{T}_0]) \tag{5.1f}$$

$$\frac{d[\mathrm{RP}_2]}{dt} = k_{\mathrm{RP}_2}([\mathrm{S}]+[\mathrm{T}_0]+[\mathrm{T}_+]+[\mathrm{T}_-]) - k_{\mathrm{BET}_2}[\mathrm{RP}_2] \tag{5.1g}$$

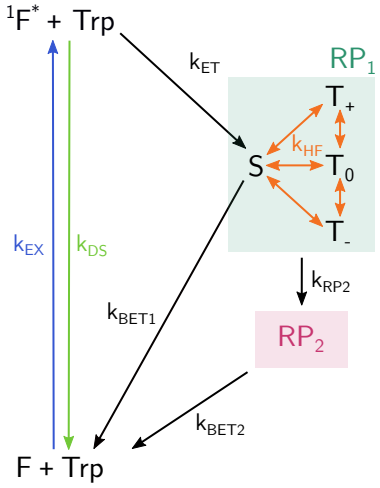


Figure 5.7: Reaction scheme for the formation of intramolecular radical pairs between a flavin cofactor (F) and a tryptophan residue in cryptochromes (see Introduction for details). The definition and values of the rate constants are given below in Table 5.1.

Rate constant	Value	Comment
k_{EX}	$3.3 \times 10^3\,\mathrm{s}^{-1}$	$= 448\,\mathrm{nm}$, $12\,\mu\mathrm{W}$.
	$6.5 \times 10^3\,\mathrm{s}^{-1}$	$= 448\,\mathrm{nm}$, $24\,\mu\mathrm{W}$.
	$1.3 \times 10^4\,\mathrm{s}^{-1}$	$= 448\,\mathrm{nm}$, $49\,\mu\mathrm{W}$.
		First order kinetics in the weak absorbance limit of the Beer-Lambert Law.
k_{DS}	$1 \times 10^8\,\mathrm{s}^{-1}$	Decay of the flavin excited state by processes other than electron transfer.[22]
k_{ET}	$1 \times 10^{10}\,\mathrm{s}^{-1}$	Formation of RP_1 by electron transfer.[34]
k_{BET_1}	$3.3 \times 10^4\,\mathrm{s}^{-1}$	Back electron transfer from RP_1 to the ground state.[36]
k_{RP_2}	$2.8 \times 10^4\,\mathrm{s}^{-1}$	Formation of RP_2 by proton transfer.[36]
k_{HF}	$8 \times 10^7\,\mathrm{s}^{-1}$	Coherent singlet-triplet interconversion of the spin states of the geminate radical pair by the hyperfine mechanism.[97]
k_{BET_2}	$2 \times 10^3\,\mathrm{s}^{-1}$	Back electron transfer from RP_2 to the ground state.[126]

Table 5.1: Values of the rate constants used in calculations of the relative concentrations of FAD and RP_2 at different excitation powers.

Note that the system was considered in the absence of a magnetic field. The scanning nature of the apparatus as well as the asymmetry of the slow radical termination reactions (that give rise to enhanced MFEs) were ignored for simplicity. Unfortunately, the rate constants of *Dm*Cry Trp_D mutant have not yet been properly characterised by time-resolved spectroscopy. Therefore, the exact concentrations of the ground state and RP_2 cannot be determined but the impact of the excitation power on the system's behaviour can still be explored using kinetic parameters from other cryptochromes. Thus, the rate constants of *Dm*Cry wild-type (WT) were used instead. The definition and values of the rate constants are given in Table 5.1.

The overall fluorescence of the system is a function of the concentrations of FAD and

RP_2 weighted by their respective fluorescence quantum yields. According to Figure 5.8, which presents the evolution of the calculated FAD and RP_2 concentrations, the relative contribution of RP_2 to the system's fluorescence increases with an increasing excitation power whilst that of the FAD decreases.

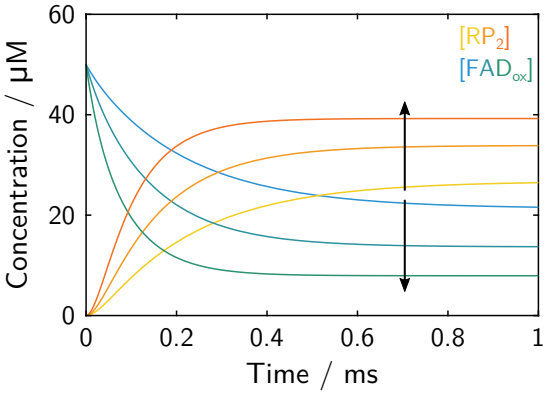
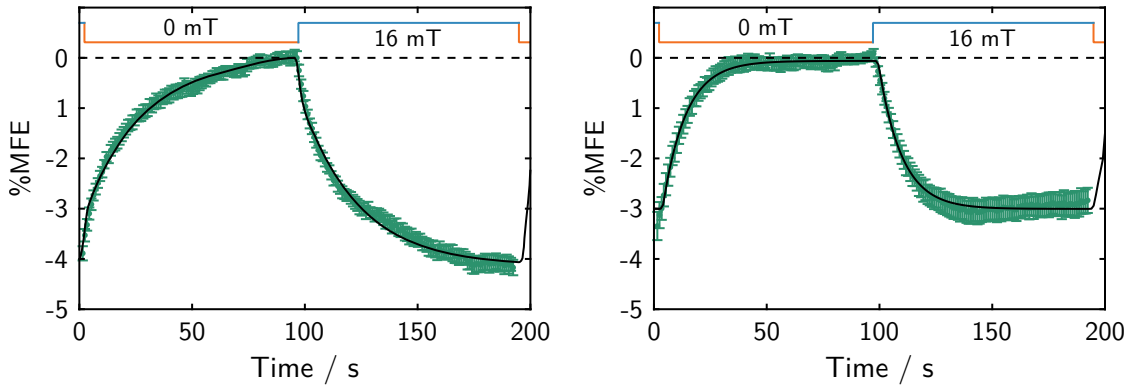


Figure 5.8: Simulated temporal evolution of the system in the absence of a magnetic field for different excitation powers (12, 24 and 49 μW). The corresponding rate constants are given in Table 5.1. The initial cryptochrome concentration was 50 μM. The scanning nature of the apparatus as well as the asymmetry of the slow radical termination reactions were ignored for simplicity. The arrows indicate the effect of increasing power.

Thus, the behaviour of the MFE on *Dm*Cry Trp_D mutant in Figure 5.5 can be interpreted as follows. At low power, FAD is dominant, yielding a positive MFE. As the excitation power increases, the long-lived radical pair accumulates and, eventually, its contribution to the total fluorescence overcomes that of the oxidised flavin whose concentration has been declining, resulting in an inversion of the MFE. The nature of the resulting MFE, therefore, depends on the relative concentrations of FAD and RP_2 as well as their respective fluorescence quantum yields.

Comparison of animal cryptochromes

***Dm*Cry and *Er*Cry4 WT** The *Drosophila* cryptochrome is the first animal cryptochrome whose magnetoreception has ever been investigated.[25,36] Therefore, it constitutes a good reference for comparison with the MFE of other animal cryptochromes and, in particular, that of the European robin, which is of prime importance as it is a migratory bird. Their respective MFEs at 49 μW are shown in Figure 5.9.



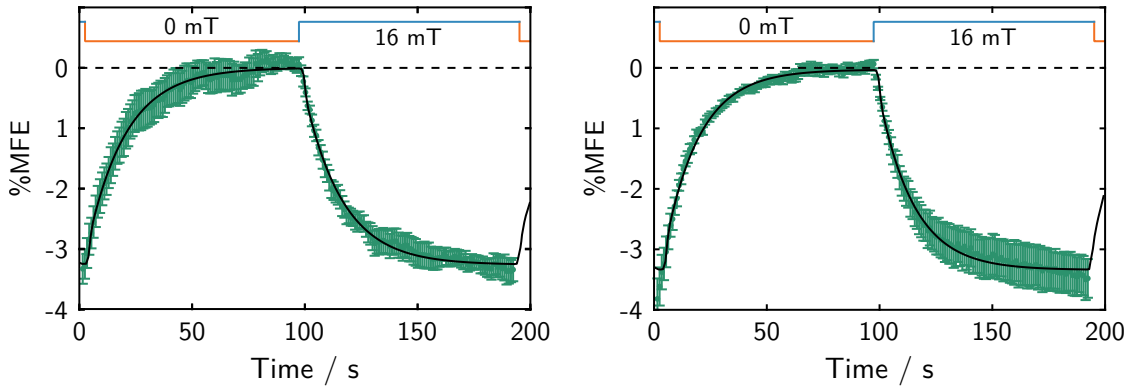
(a) *Dm*Cry WT (b) *Er*Cry4 WT

Figure 5.9: Comparison of the magnetosensitivities of two animal cryptochromes following photoexcitation at 49 μW.

Both cryptochromes exhibit relatively large negative MFEs. In light of the discussion above, the sign of their MFE was to be expected as they both form a flavin radical anion in RP_2. However, these results are extremely surprising considering that the MFE of *Dm*Cry WT has been reported to be markedly smaller than that of other cryptochromes, and almost an order of magnitude smaller than that of the robin.[36,37]

Comparing the results presented here to the previously reported data should be done with caution. Indeed, this is the first time cryptochromes other than *At*Cry1 are studied by fluorescence spectroscopy, which is vastly different from absorption-based experiments. Both types of techniques probe different species, have different sensitivities and detect different timescales. In the latter, the magnitude of the MFE is determined by how well the back electron transfer from RP_1, the formation of RP2 and spin relaxation compete with each other. Whilst this is still extremely important for fluorescence-based technniques, the continuous nature of the experiment renders the slower processes paramount. In particular, as highlighted above, the relative concentrations of FAD and RP_2 seems to govern the fluorescence-detected MFE of cryptochromes. These concentrations are themselves strongly affected by the rate of the back electron transfer from RP_2: the slower that step, the larger the RP_2 concentration. A recent study employing cavity ring-down spectroscopy demonstrated that the lifetime of RP_2 in the avian cryptochrome is less than half that of the insect cryptochrome.[126] This much faster back electron transfer most likely shifts the equilibrium between the radical and the oxidised flavin towards the latter, hence decreasing the overall negative MFE of the robin, making it comparable to that of the fruit fly.

***Dm*Cry and *Er*Cry4 Trp_D mutants** The main difference between animal and plant cryptochromes is the addition of a fourth tryptophan residue to the conserved tryptophan triad and the resulting extended electron transfer pathway.[25] Obviously, the potential role of this fourth tryptophan in magnetoreception is the source of much speculation. A working hypothesis is that the third tryptophan would act as a sensor and transmit the magnetic information to the fourth tryptophan which would then have a signalling function.[37]

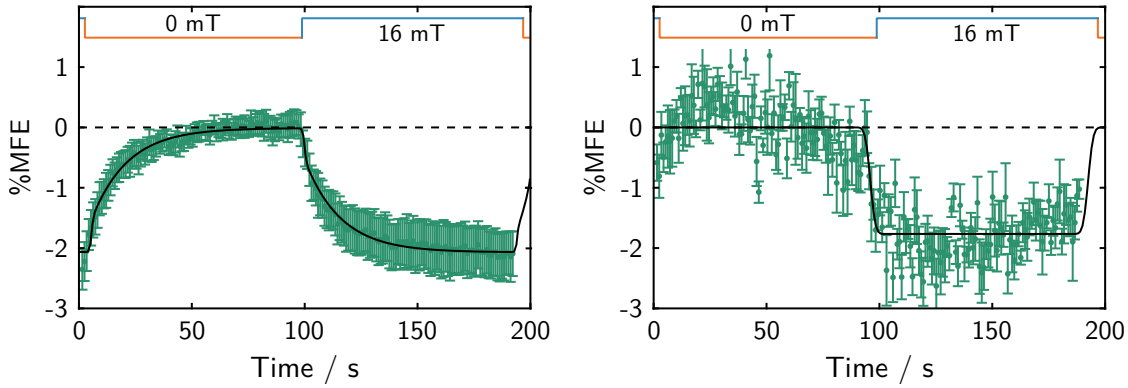


(a) *Er*Cry4 WT (b) *Er*Cry4 Trp_D mutant

Figure 5.10: Comparison of the magnetosensitivities of the *Er*Cry4 wild-type and Trp_D mutant following photoexcitation at 36 μW.

The respective MFEs of the wild-type and mutant robin cryptochromes are displayed in Figure 5.10. It appears that the mutation is relatively unimpactful as both the wild-type and the mutant exhibit very similar MFEs. This was also observed in *Dm*Cry (see Figures 5.5 bottom and 5.9a) and *Er*Cry4 at 49 μW. Once again, these results are in disagreement with previously reported absorption-detected data, in which substituting the last tryptophan with a redox-inert amino acid dramatically increases the magnitude of the MFE.[37] This behaviour has been attributed to the shorter lifetime of RP_1 in the mutant ($\tau_{RP_1} \sim 1\,\mu s$) compared to the wild-type ($\tau_{RP_1} = 10\,\mu s$).[126] The shorter electron transfer chain enhances the efficiency of the charge recombination which, in turn, allows the spin-selective back electron transfer to compete more effectively with the formation of RP_2 and relaxation processes, giving rise to larger MFEs in Trp_D mutants.[37,126] Here, this phenomenon is counterbalanced by the concomitant shorter lifetime of RP_2. As explained above, this shifts the equilibrium between the radical and FAD towards the latter, therefore decreasing the overall MFE of the Trp_D mutant.

Comparison of avian cryptochromes Cryptochromes have been found in both migratory and non-migratory birds. If they are indeed used for magnetoreception, it is likely that evolution would have optimised their functionality in birds which make use of this sense as oppposed to those that don't migrate. Thus, comparing the response to a field of a cryptochrome sourced from a migratory bird to that of a cryptochrome from a non-migratory bird may provide some insight into the biological role of cryptochromes.



(a) Fluorescence detected between 475 and 645 nm. (b) Fluorescence detected between 700 and 750 nm.

Figure 5.11: Average MFE of *Cl*Cry4 Trp_D mutant over one field step. The excitation power was 36 μW and the fluorescence was measured with different detection windows.

For this purpose, the Trp_D mutant of the pigeon cryptochrome was investigated. Its MFE is presented in Figure 5.11a. As for other animal cryptochromes, *Cl*Cry4 exhibits a negative MFE but it is smaller than that of the robin measured in similar conditions (-2.3% compared to -3.5%, see Figure 5.10b). This is very encouraging as it suggests that robins are more sensitive to the applied magnetic field. This would give credence to the hypothesis that the magnetic compass sense was optimised in robins as a result of evolutionary pressure. Unfortunately, there is no comparison of the MFEs of the Trp_D mutants of the two avian cryptochromes in the literature. However, recent absorption studies reported a much larger difference between the wild-type cryptochromes (∼-9.5% for the robin compared to ∼0.5% for the pigeon at 30 mT).[37] Relatively little has been published about the dynamics of the RPM in *Cl*Cry so it is impossible, at that stage, to interpret further the relative magnitudes of the robin and pigeon MFEs.

Most importantly, the pigeon has been shown to further stabilise the radical pair by protonation, leading to an accumulation of both $FAD^{\bullet-}$ and $FADH^{\bullet}$.[26,37] As mentioned above, both radicals fluoresce in different regions. In order to better characterise the MFE originating from the radical, which has been central to the interpretation of the

data presented in this chapter so far, the magnetic field effect was then measured between 700 and 750 nm. In this region, the flavin ground state is essentially non-fluorescent and the detected fluorescence is mostly that of $FADH^{\bullet}$. The resulting MFE is presented in Figure 5.11b. Although the MFE is quite noisy due to the weak fluorescence measured, its existence is unambiguous, which confirms that the negative MFEs measured so far in cryptochromes truly originate from the fluorescence of radicals.

5.2 Anisotropic magnetic field effects in cryptochrome crystals

The data presented above established the suitability of confocal microscopy for the investigation of MFEs in cryptochrome solutions and FMN-doped lysozyme crystals. Building upon these successes, this section employs this technique for the examination of anisotropic MFEs in cryptochrome crystals.

As discussed previously, anisotropic MFEs arise from anisotropic hyperfine interactions within the two radical pair partners. In cryptochromes, the flavin radical exhibits the largest anisotropic hyperfine interactions and, therefore, mostly dictates the behaviour of the radical pair.[47] As depicted in Figure 5.12, the hyperfine tensor of N5 (displayed in green) is the most anisotropic and is mainly oriented perpendicular to the isoalloxazine ring. The response of a cryptochrome radical pair to the direction of an applied magnetic field is, therefore, mainly governed by the relative orientation of the isoalloxazine ring and the magnetic field.

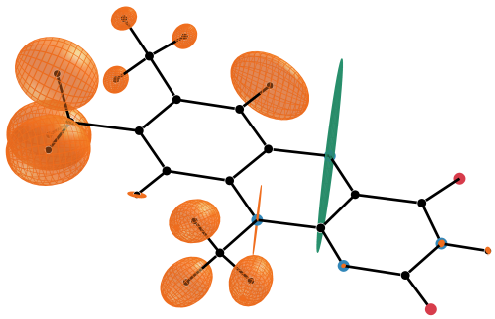


Figure 5.12: Hyperfine tensors of a flavin radical anion. Calculations were carried out using Orca at the B3LYP/EPR II level of theory for a flavin radical with a ribityl side chain truncated after the first carbon.[48] The hyperfine tensor of N5 is highlighted in green.

So far, only a few cryptochromes, including *At*Cry1 and *Dm*Cry, have been crystallised, but no one has ever been able to crystallise *Er*Cry4. The only avian cryptochrome that has been successfully crystallised is *Cl*Cry4. It adopts an orthorhombic structure in the space group P 2_1 2_1 2_1, meaning that the four proteins in the unit cell are related by a 2_1 screw axis (rotation by 180° and translation by half a unit cell along the rotation axis).[26] The unit cell of a crystal of *Cl*Cry4 WT is displayed in Figure 5.13 and the flavin cofactors are highlighted.

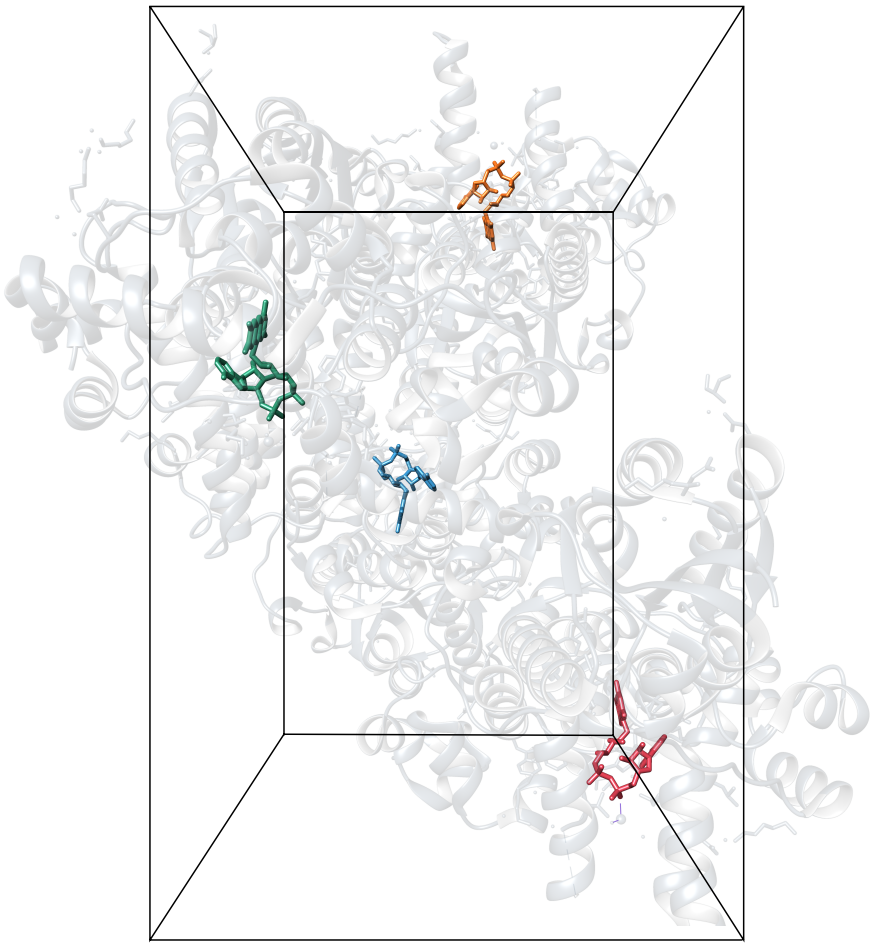


Figure 5.13: Unit cell of a crystal of *Cl*Cry4 WT drawn from PDB entry 6PU0 using Chimera.[26,27] The flavin cofactors of the proteins are highlighted.

Importantly, the isoalloxazine rings of all four flavin cofactor are almost parallel to each other, meaning that the main hyperfine tensors of the flavin radicals are mostly aligned, which bodes well for the development of an anisotropic response to the applied magnetic field.

5.2.1 Methods

Crystal growth

*Cl*Cry4 wild-type and Trp_D mutant were crystallised on-site by Yogarany Chelliah from Prof. Joseph Takahashi's lab. She prepared the crystals using the hanging drop method and following the protocol published recently by Zoltowski *et al.*[26]

MFE experiment

Apparatus The measurement of anisotropic magnetic field effects was conducted using the same Zeiss LSM 5 Exciter confocal microscope as in the previous chapter. As before, the sample was irradiated continuously by a 458 nm laser at 15 μW through a 63× oil-immersion objective and its fluorescence was recorded in parallel. In order to examine the effect of the direction of the field onto the sytem, two orthogonal pairs of coils were used. The magnetic field was kept at constant magnitude (16 mT) and rotated in the sample plane.

It is extremely important to note that the phase of the magnetic field rotation with respect to one of the principal axes of the crystal could not be controlled nor monitored over the course of the experiment for several reasons:

- The microscope employed could not be externally triggered, meaning that the frames acquisition and the waveform generator used to control the field could not be triggered together and were instead triggered manually roughly at the same time. While this was hardly a problem for the experiments presented in Chapter 4, where the field was a square wave, it is significantly more inconvenient here, where the direction of the field is continuously changing. Concretely, this means that the exact direction of the field at a given time cannot be determined.

- The general orientation of the crystal in the frame is unknown as the microscope was not equipped with a camera allowing to record bright-field images of the crystal at the beginning of an experiment.

Although the lack of control over the relative orientations of the crystal and the field is frustrating, it does not preclude the examination of anisotropic MFEs in crystals. Indeed, the period of the field rotation was chosen as an integer multiple of the scan speed

(1.96 s/frame) and no significant dephasing between the field and the frames acquisition was observed over the course of the experiment. Thus, the general behaviour of the field is well characterised and controlled and its impact on the system's fluorescence can, therefore, be monitored.

Data analysis The data analysis procedure is relatively similar to that used for the measurement of isotropic MFEs. The fluorescence intensity of each frame was averaged over an ROI corresponding to the location of the crystal. The resulting time-resolved fluorescence trace was then split into segments whose length was determined by the duration of a field rotation period. The fluorescence baseline was obtained from a smoothing interpolent through the first points of each segment and subtracted. The overall evolution of the fluorescence intensity over a field rotation was then determined by averaging together all the baseline-subtracted segments.

5.2.2 Results and discussion

The temporal evolution of the fluorescence of a crystal of *Cl*Cry4 Trp_D mutant subjected to a rotating magnetic field is presented in Figure 5.14. In this case, the field rotation period was chosen as 60 times the scan speed, *i.e.* 117.6 s. Similar to the data presented in the previous section, the fluorescence increases over the course of the experiment due to the release of free flavin.

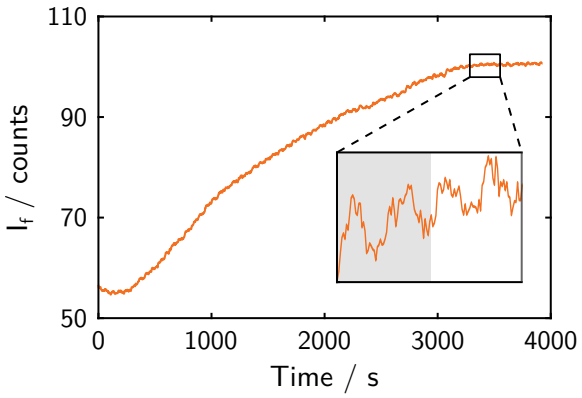


Figure 5.14: Fluorescence intensity of a *Cl*Cry4 Trp_D mutant crystal with a 16 mT magnetic field rotating in the sample plane at a period of 117.6 s. The modulation of the fluorescence over two field periods, which are highlighted by different background colours, is shown expanded in the inset.

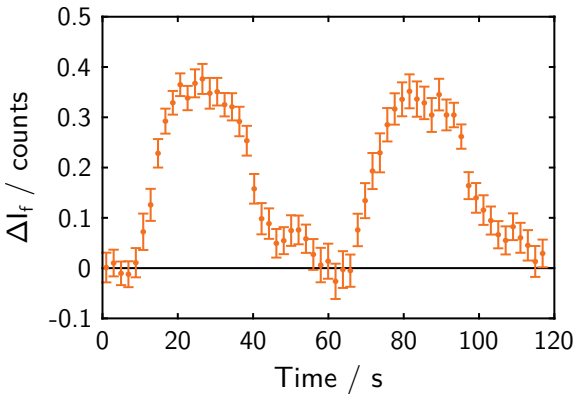


Figure 5.15: Average change in the fluorescence intensity of a *Cl*Cry4 Trp_D mutant crystal over a full field rotation period of a 16 mT magnetic field (field rotation period of 117.6 s). In this case, 22 field rotation periods were averaged together.

Most importantly, a small oscillation is clearly superimposed onto the overall fluorescence increase. Based on the inset, in which the fluorescence intensity over two full field periods is shown expanded, the period of this oscillation seems to be half of that of the field. This was confirmed by the Fourier transform of the baseline-subtracted signal and is also more clearly visible in Figure 5.15, where the average response of the crystal's fluorescence to a full rotation of the magnetic field is displayed. As explained above, the exact phase of the magnetic field as a given time is not known. For this reason, the data is presented as a function of time rather than angle.

The evolution of the system's fluorescence over a field rotation period is in agreement with what is expected of a chemical compass based on the radical pair mechanism, in which it is the inclination of the field, rather than its polarity, that determines the response of the system. The fluorescence intensity is, therefore, expected to be invariant with respect to the field polarity such that, for an arbitraty angle θ between one of main axes of the crystal and the field direction, $I_f(\theta) = I_f(\theta + \pi)$. Such a behaviour was also observed in the absorbance-detected MFE of the original triad chemical compass.[14,127] Crucially, the clear dependence of the system's fluorescence on the direction of the magnetic field demonstrates its ability to act as a chemical compass.

A similar pattern was also observed in a wild-type cryptochrome crystal, as shown in Figure 5.16, in which only a half period is displayed. In this case, only 15 half periods could be averaged as the data was of lower quality than for the mutant. This is most likely because all the crystals were prepared at once but run at different times. The Trp_D mutant crystals were investigated first and were, therefore, fresher than the wild-type

samples, which were examined at a later time.

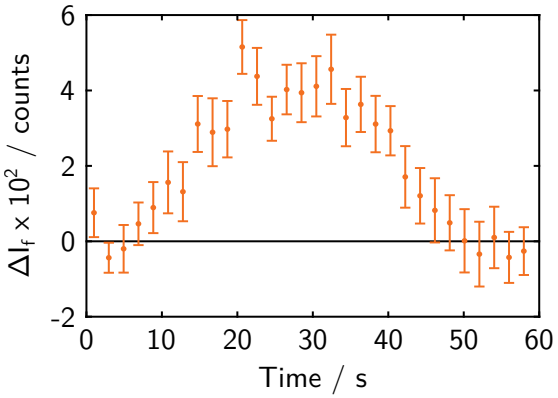


Figure 5.16: Average change in the fluorescence intensity of a *Cl*Cry4 WT crystal over half a field rotation period of a 16 mT magnetic field. (field rotation period of 117.6 s). 15 half periods were averaged together.

The data presented above most likely consitutes the first report of an anisotropic magnetic field effect on the reactivity of a cryptochrome protein. In particular, the fact that two different samples exhibit similar responses to the direction of the field strongly suggests that the anisotropic MFEs detected are indeed real and gives credence to the putative role of cryptochromes as chemical compasses. However, this study is suffering from a lack of knowledge regarding the phase of the field and the crystal orientation and should imperatively be reproduced in more controlled experimental conditions. This prompted the purchase of the Leica confocal microscope, which allows to carefully control and monitor the orientations of both the field and the crystal. Similar studies were scheduled to take place in May 2020. Unfortunately, due to the travel restrictions in place, Yogarany Chelliah was not able to travel to Oxford to grow the cryptochrome crystals and these experiments have yet to be reproduced.

5.3 Conclusion and outlook

This chapter has explored the magnetosentivity of a variety of cryptochromes in different conditions using confocal microscopy.

For the first time, the MFEs of animal cryptochromes, including that of a migratory bird, were investigated using a fluorescence-based technique. This study revealed the existence of a hitherto unsuspected magnetic field effect originating from the weak fluorescence of the flavin semiquinone radicals. Under conditions of continuous photoexcitation,

the radicals accumulate over the course of the experiment and their contribution to the overall fluorescence of the system may, under appropriate conditions, exceed that of FAD. This phenomenon yields a negative MFE in spite of the singlet-born nature of the radical pair and the overall MFE detected, therefore, results from the competing MFEs from the oxidised flavin and the radicals. Their relative magnitudes depend on the experimental conditions as well as the different rate constants of the system under investigation. The deconvolution of these two MFEs is challenging, especially given that the fluorescence quantum yields of the radicals are unknown. Of course, they will need to be determined in order for more quantitative analyses to be conducted. Wavelength-resolved studies, which take advantage of the different fluorescence spectra of the species involved, may also allow to discriminate the two competing MFEs.

Beyond cryptochrome solutions, and building upon the conclusions of the previous chapters, anisotropic MFEs were then investigated in pigeon cryptochrome crystals using confocal microscopy, which is uniquely suited for this purpose. Both *Cl*Cry wild-type and $\mathrm{Trp_D}$ mutant crystals exhibited a very clear dependence on the direction of a magnetic field of constant magnitude rotating in the sample plane. This demonstrates the ability of cryptochromes to exhibit a compass behaviour and, thereby, alleviates one of the main concerns regarding the cryptochrome hypothesis.

Conclusion

General Discussion and Outlook

This work has identified several suitable approaches for the measurement of directionally dependent magnetic field responses – anisotropic magnetic field effects – in cryptochromes in order to, ultimately, be able to determine whether they can function as chemical compasses. Indeed, although magnetosensitive radical pair reactions in cryptochromes are now well-established as the leading candidate for the underlying mechanism of the avian compass sense, unequivocal evidence that these proteins are the primary magnetic sensors is still sorely lacking.[13] In particular, even though a variety of theoretical studies have suggested that cryptochromes were fit for purpose as chemical compasses, the lack of tangible proof that the direction of a magnetic field can affect their reactivity has cast doubt on the viability of a cryptochrome-based avian compass.[5,6]

Within this context, what is crucially needed is an experiment with the power to prove that migratory birds really do use cryptochromes as the primary magnetic sensor. One such experiment could involve selectively manipulating the magnetic properties of the cryptochrome radical pair by isotopic enrichment of the flavin radical *in vivo*. As isotopes have different spin quantum numbers and gyromagnetic ratios, isotopic substitution is expected to dramatically alter the magnitude and/or symmetry of the hyperfine interaction and, in turn, the birds' migratory behaviour. Chapter 1 discussed the feasibility of such an experiment by investigating the impact of ^{13}C isotopic enrichment on the magnetic responses of model systems in the low-field region in which the avian compass operates.

Owing to the sensitivity of the newly improved prompt fluorescence MARY apparatus, the examination of the FMN-ascorbic acid system revealed that a significant asymmetry between the hyperfine couplings of the two radical pair partners was necessary for an appreciable low field effect to develop. Thus, ^{13}C-enrichment of the flavin radical, whose effect on the hyperfine coupling is only marginal, was found to have almost no impact on the magnetosensitivity of the system. This was also observed in the FMN-HEWL model

system, which is more similar to the cryptochrome radical pair.

At this stage, this study is not sufficient to ascertain the viability of the *in vivo* experiment as it is inherently limited by the fact that only the isotropic MFEs of model systems could be examined. Indeed, isotopically labelled flavins have yet to be successfully incorporated into cryptochromes. The spin chemistry of the proteins differs from that of model systems and they could, therefore, respond quite differently to isotopic enrichment. Likewise, anisotropic MFEs, whose behaviour cannot be inferred from that of isotropic MFEs, have yet to be detected in flavin-based systems. Thus, further preliminary tests involving the measurement of anisotropic MFEs in cryptochromes will be required before conclusions can be drawn regarding the feasibility of the *in vivo* experiment. In the meantime, fully simulating the impact of different isotopic substitutions (for instance with a combination of ^{13}C and ^{15}N) on the magnetosensitivity of the system would certainly be very beneficial in order to identify the most promising isotopologue.

Concretely, anisotropic responses to a magnetic field can only develop if the radical pairs are somewhat immobilised and aligned. Experimentally, this can be achieved either by photoselection of an immobilised sample or by direct molecular alignment. In Chapter 2, a variety of rigid and viscous media were investigated for the immobilisation of flavin-based radical pairs. They were systematically assessed and compared based on three main criteria. First, their ability to maintain the photophysical properties of the system was established by examining the absorption and fluorescence spectra of FMN in the different media. Then, the degree of immobilisation provided was determined by fluorescence anisotropy. Finally, the MFEs of the FMN-tryptophan system encapsulated in the different rigid matrices were measured by prompt fluorescence MARY in order to ensure that the spin chemistry of the system was not impeded. Following these investigations, it was concluded that glycerol aqueous solutions showed the most promise.

However, as developed in Chapter 3, glycerol seems to be able to act as an electron donor and its reaction with flavin molecules was found to give rise to an MFE. While the existence of this unexpected MFE is certainly worrying considering that the small amount of free flavin present in cryptochrome samples could react with the glycerol-containing buffer, the fact that it stems from a triplet-born radical pair makes it distinguishable from the flavin-tryptophan MFE of interest. Additionally, it seems to require higher glycerol

content and excitation power to develop compared to what is usually employed for cryptochrome measurements. Thus, the impact of the previously unsuspected flavin-glycerol MFE is expected to be relatively limited.

However, its existence prompted the investigation of alternative immobilisation methods such as direct molecular alignment in protein crystals. Exploring the magnetosensitivity of such samples comes with many challenges. Indeed, cryptochromes have proven to be particularly difficult to crystallise and most of the traditional MFE experiments are optimised for liquid samples. Chapter 4 showcased confocal microscopy as a reliable technique for the detection of MFEs in both solutions and crystals. Proof-of-principle studies were conducted in FMN-HEWL and cryptochrome solutions as well as FMN-doped HEWL crystals. As highlighted by the examination of the interplay between dopant diffusion and photobleaching in FMN-HEWL crystals, the high quality of the data allows to extract a wealth of information, including the spatio-temporal evolution of the fluorescence intensity and the magnetic field effect, paving the way for the study of more complex biological samples such as cells and tissues.

Expanding beyond methodology development, confocal microscopy was employed in Chapter 5 for a more in-depth investigation of the fluorescence-detected magnetosensitivity of cryptochromes. First, the behaviours of a variety of cryptochrome solutions, including plant, insect and bird cryptochromes, were compared and contrasted. Surprisingly, animal cryptochromes were found to exhibit a negative MFE, which was attributed to the fluorescence of the flavin radical. The relative concentrations of the fully oxidised and semiquinone flavins, which depend on the experimental conditions as well as the nature of the cryptochrome, seem to be the main factor determining the sign of the overall MFE measured. In order to determine the relative importance of the MFEs originating from the two fluorophores, a more quantitative analysis will be required. This includes the determination of their respective fluorescence quantum yields as well as the characterisation of the effect of raster scanning on the kinetics of the system. Further, while the fluorescence of the radical certainly appears to be the most likely explanation for the presence of this negative MFE at this stage, several additional experiments, such as the study of a flavin-less protein in the presence of free flavin, could be conducted in order to fully verify this hypothesis and ascertain that the role of free flavin is indeed negligible.

Crucially, this study fully established confocal microscopy as a valid detection technique for the measurement of MFEs in cryptochrome solutions. Indeed, not only does it provide data of excellent quality but it also uses ten times less sample than some other experiments. Now that a wider selection of bird cryptochromes have very recently become available, it opens the way for a larger investigation of cryptochromes from strategically chosen birds on the phylogenetic tree, thereby potentially gaining some insight into the evolutionary optimisation of the avian magnetic compass sense.

Finally, the response of a pigeon cryptochrome crystal to the direction of the field was investigated and a very clear modulation of the fluorescence intensity could be observed as the field was rotated in the sample plane. Although this result is very exciting and could very well be the first anisotropic MFE to ever be detected in cryptochromes, it should be treated with caution as it has yet to be reproduced. The recent relaxation of travel restrictions as well as the puchase of a Leica microscope, which allows to properly synchronise the field with the frames acquisition and to record the position of the crystal with respect to the field of view, are expected to allow the verification of this result very soon. Obviously, due to the low availability of cryptochrome crystals, only a single set of experimental parameters was tested. As more crystals become available, a proper optimisation of the frame rate and laser power as well as the way the direction of the field is varied would certainly need to be conducted, especially considering the potential impact of enhanced MFEs on the response of the system to the direction of the field.

Thus, this work suggests that crystallising cryptochromes is the most promising approach for the measurement of anisotropic MFEs. It may eventually be employed to determine the impact of isotopic substitution on anisotropic MFEs in an effort to establish the viability of the *in vivo* experiment. Considering how these proteins can only be crystallised in a very narrow range of experimental conditions, it is not impossible that isotopic labelling could disturb this process. If so, the use of glycerol aqueous solutions could constitute a good alternative as glycerol was shown to immobilise cryptochromes very efficiently. A proper characterisation of the amount of free flavin present in the sample throughout the experiment, for instance using time-resolved fluorescence, would then be needed in order to fully ascertain that the signal detected truly originates from the cryptochrome radical pair.

Appendix

Table of Hyperfine Parameters

Nucleus	Natural abundance	^{13}C
N1	-0.01	–
C2	–	-0.03
N3	-0.04	–
H3	-0.01	–
C4	–	-0.17
C4a	–	-0.22
N5	0.51	–
C5a	–	-0.86
C6	–	0.54
H6	-0.42	–
C7	–	-0.56
C7α	–	0.08
H(C7 — CH_3)	0.16	–
C8	–	0.66
C8α	–	-0.28
H(C8 — CH_3)	0.49	–
C9	–	-0.38
H9	0.06	–
C9a	–	0.20
N10	0.19	–
C10α	–	-0.18
H(N10 — CH_3)	0.31	–
C10a	–	-0.20

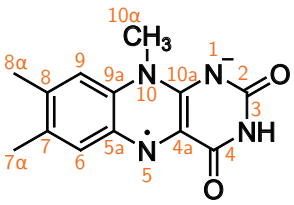


Table 1: Hyperfine couplings in mT of a flavin radical anion $F^{\bullet -}$ calculated by DFT using Orca at the B3LYP/EPRII level of theory.[48]

Nucleus	Natural abundance	^{13}C
N1	0.04	–
C2	–	-0.16
N3	-0.02	–
H3	-0.07	–
C4	–	-0.51
C4a	–	0.61
N5	0.43	–
H5	-0.82	–
C5a	–	-0.56
C6	–	0.23
H6	-0.19	–
C7	–	-0.22
C7α	–	0.02
H(C7 — CH_3)	0.04	–
C8	–	0.34
C8α	–	-0.14
H(C8 — CH_3)	0.28	–
C9	–	-0.27
H9	0.06	–
C9a	–	0.10
N10	0.24	–
C10α	–	-0.19
H(N10 — CH_3)	0.40	–
C10a	–	-0.62

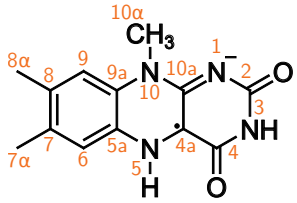


Table 2: Hyperfine couplings in mT of a flavin neutral radical FH• calculated by DFT using Orca at the B3LYP/EPRII level of theory.[48]

Nucleus	Natural abundance
N1	0.37
H2	0.04
H(C3 —— CH_2R)	1.72
H5	-0.44
H6	0.06
H7	-0.36
H8	-0.05

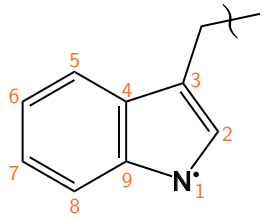


Table 3: Hyperfine couplings in mT of the tryptophan radical $Trp^{\bullet}$ calculated by DFT using Orca at the B3LYP/EPRII level of theory.[48]

Nucleus	C12	C13
C1	–	-0.42
C2	–	-0.54
C3	–	-0.11
C4	–	-0.33
H4	0.39	–
C5	–	0.17
H5	-0.01	–
H(C5 —— OH)	-0.04	–
C6	–	0.03
H6	0.01	–
H(C6 —— OH)	∼0	–

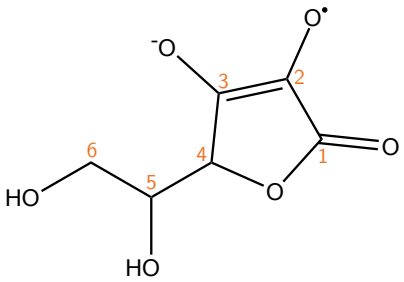


Table 4: Hyperfine couplings in mT of the ascorbate radical $Asc^{\bullet-}$ calculated by DFT using Orca at the B3LYP/EPRII level of theory.[48]

References

1. Mouritsen, H. Long-distance navigation and magnetoreception in migratory animals. *Nature* **2018**, *558*, 50–59.

2. Johnsen, S.; Lohmann, K. J. The physics and neurobiology of magnetoreception. *Nature Reviews Neuroscience* **2005**, *6*, 703–712.

3. Fleissner, G.; Holtkamp-Rötzler, E.; Hanzlik, M.; Winklhofer, M.; Fleissner, G.; Petersen, N.; Wiltschko, W. Ultrastructural analysis of a putative magnetoreceptor in the beak of homing pigeons. *Journal of Comparative Neurology* **2003**, *458*, 350–360.

4. Wiltschko, R.; Wiltschko, W. The magnetite-based receptors in the beak of birds and their role in avian navigation. *Journal of Comparative Physiology A - Neuroethology Sensory Neural and Behavioral Physiology* **2013**, *199*, 89–98.

5. Schulten, K.; Swenberg, C. E.; Weiler, A. A Biomagnetic Sensory Mechanism Based on Magnetic Field Modulated Coherent Electron Spin Motion. *Zeitschrift fur Physikalische Chemie* **1978**, *111*, 1–5.

6. Ritz, T.; Adem, S.; Schulten, K. A Model for Photoreceptor-Based Magnetoreception in Birds. *Biophysical Journal* **2000**, *78*, 707–718.

7. Treiber, C. D.; Salzer, M. C.; Riegler, J.; Edelman, N.; Sugar, C.; Breuss, M.; Pichler, P.; Cadiou, H.; Saunders, M.; Lythgoe, M.; Shaw, J.; Keays, D. A. Clusters of iron-rich cells in the upper beak of pigeons are macrophages not magnetosensitive neurons. *Nature* **2012**, *484*, 367–370.

8. Emlen, S. T.; Emlen, J. T. A technique for recording migratory orientation of captive birds. *The Auk* **1966**, *83*, 361–367.

9. Wiltschko, W.; Wiltschko, R. Magnetic compass of European robins. *Science* **1972**, *176*, 62–64.

10. Wiltschko, W.; Wiltschko, R. Migratory orientation of European Robins is affected by the wavelength of light as well as by a magnetic pulse. *Journal of Comparative Physiology A* **1995**, *177*, 363–369.

11. Engels, S.; Schneider, N. L.; Lefeldt, N.; Hein, C. M.; Zapka, M.; Michalik, A.; Elbers, D.; Kittel, A.; Hore, P. J.; Mouritsen, H. Anthropogenic electromagnetic noise disrupts magnetic compass orientation in a migratory bird. *Nature* **2014**, *509*, 353–356.

12. Günther, A.; Einwich, A.; Sjulstok, E.; Feederle, R.; Bolte, P.; Koch, K.-W.; Solov'yov, I. A.; Mouritsen, H. Double-Cone Localization and Seasonal Expression Pattern Suggest a Role in Magnetoreception for European Robin Cryptochrome 4. *Current Biology* **2018**, *28*, 211–223.e4.

13. Hore, P. J.; Mouritsen, H. The Radical-Pair Mechanism of Magnetoreception. *Annual Review of Biophysics* **2016**, *45*, 299–344.

14. Kerpal, C.; Richert, S.; Storey, J. G.; Pillai, S.; Liddell, P. A.; Gust, D.; Mackenzie, S. R.; Hore, P. J.; Timmel, C. R. Chemical compass behaviour at microtesla magnetic fields strengthens the radical pair hypothesis of avian magnetoreception. *Nature Communications* **2019**, *10*.

15. Steiner, U. E.; Ulrich, T. Magnetic Field Effects in Chemical Kinetics and Related Phenomena. *Chemical Reviews* **1989**, *89*, 51–147.

16. Brocklehurst, B. Spin correlation in the geminate recombination of radical ions in hydrocarbons. *J. Chem. Soc. Faraday Trans II* **1976**, *72*, 1869–1884.

17. Timmel, C. R.; Till, U.; Brocklehurst, B.; Mclauchlan, K. A.; Hore, P. J. Effects of weak magnetic fields on free radical recombination reactions. *Molecular Physics* **1998**, *95*, 71–89.

18. Hemmerich, P.; Nagelschneider, G.; Veeger, C. Chemistry and molecular biology of flavins and flavoproteins. *FEBS Letters* **1970**, *8*, 69–83.

19. Chaves, I.; Pokorny, R.; Byrdin, M.; Hoang, N.; Ritz, T.; Brettel, K.; Essen, L.-O.; van der Horst, G. T. J.; Batschauer, A.; Ahmad, M. The Cryptochromes: Blue Light Photoreceptors in Plants and Animals. *Annual Review of Plant Biology* **2011**, *62*, 335–364, PMID: 21526969.

20. Holzer, W.; Shirdel, J.; Zirak, P.; Penzkofer, A.; Hegemann, P.; Deutzmann, R.; Hochmuth, E. Photo-induced degradation of some flavins in aqueous solution. *Chemical Physics* **2005**, *308*, 69–78.

21. Sikorska, E.; Khmelinskii, I. V.; Worrall, D. R.; Koput, J.; Sikorski, M. Spectroscopy and Photophysics of Iso-and Alloxazines: Experimental and Theoretical Study. *Journal of Fluorescence* **2004**, *14*, 57–64.

22. Holzer, W.; Penzkofer, A.; Fuhrmann, M.; Hegemann, P. Spectroscopic Characterization of Flavin Mononucleotide Bound to the LOV1 Domain of Phot1 from Chlamydomonas reinhardtii. *Photochemistry and Photobiology* **2002**, *75*, 479–487.

23. Sikorski, M.; Sikorska, E.; Koziolowa, A.; Gonzalez Moreno, R.; Bourdelande, J. L.; Steer, R. P.; Wilkinson, F. Photophysical properties of lumichromes in water. *Journal of Photochemistry and Photobiology B: Biology* **2001**, *60*, 114–119.

24. Song, S. H.; Dick, B.; Penzkofer, A.; Pokorny, R.; Batschauer, A.; Essen, L. O. Absorption and fluorescence spectroscopic characterization of cryptochrome 3 from Arabidopsis thaliana. *Journal of Photochemistry and Photobiology B: Biology* **2006**, *85*, 1–16.

25. Nohr, D.; Franz, S.; Rodriguez, R.; Paulus, B.; Essen, L.-O.; Weber, S.; Schleicher, E. Extended Electron-Transfer in Animal Cryptochromes Mediated by a Tetrad of Aromatic Amino Acids. *Biophysical Journal* **2016**, *111*, 301–311.

26. Zoltowski, B. D.; Chelliah, Y.; Wickramaratne, A.; Jarocha, L.; Karki, N.; Xu, W.; Mouritsen, H.; Hore, P. J.; Hibbs, R. E.; Green, C. B.; Takahashi, J. S. Chemical and structural analysis of a photoactive vertebrate cryptochrome from pigeon. *Proceedings of the National Academy of Sciences of the United States of America* **2019**, *116*, 19449–19457.

27. Pettersen, E. F.; Goddard, T. D.; Huang, C. C.; Couch, G. S.; Greenblatt, D. M.; Meng, E. C.; Ferrin, T. E. UCSF Chimera - A visualization system for exploratory research and analysis. *Journal of Computational Chemistry* **2004**, *25*, 1605–1612.

28. Brautigam, C. A.; Smith, B. S.; Ma, Z.; Palnitkar, M.; Tomchick, D. R.; Machius, M.; Deisenhofer, J. Structure of the photolyase-like domain of cryptochrome 1 from Arabidopsis thaliana. *Proc. Natl. Acad. Sci. U. S. A.* **2004**, *101*, 12142–12147.

29. Hore, P. J.; Kaptein, R. Proton Nuclear Magnetic Resonance Assignments and Surface Accessibility of Tryptophan Residues in Lysozyme Using Photochemically Induced Dynamic Nuclear Polarization Spectroscopy. *Biochemistry* **1983**, *22*, 1906–1911.

30. Miura, T.; Maeda, K.; Arai, T. Effect of Coulomb Interaction on the Dynamics of the Radical Pair in the System of Flavin Mononucleotide and Hen Egg-White Lysozyme (HEWL) Studied by a Magnetic Field Effect. *J. Phys. Chem. B* **2003**, *107*, 6474–6478.

31. Weiss, M. S.; Palm, G. J.; Hilgenfeld, R. Crystallization, structure solution and refinement of hen egg-white lysozyme at pH 8.0 in the presence of MPD. *Acta Crystallographica Section D: Biological Crystallography* **2000**, *56*, 952–958.

32. Posener, M. L.; Adams, G. E.; Wardman, P.; Cundall, R. B. Mechanism of tryptophan oxidation by some inorganic radical-anions: a pulse radiolysis study. *J. Chem. Soc., Faraday Trans. 1* **1976**, *72*, 2231–2239.

33. Mayhew, S. G. The effects of pH and semiquinone formation on the oxidation–reduction potentials of flavin mononucleotide. *European Journal of Biochemistry* **1999**, *265*, 698–702.

34. Maeda, K.; Robinson, A. J.; Henbest, K. B.; Hogben, H. J.; Ahmad, M.; Schleicher, E.; Weber, S.; Timmel, C. R.; Hore, P. J. Magnetically sensitive light-induced reactions in cryptochrome are consistent with its proposed role as a magnetoreceptor expressed the proteins. *Proceedings of the National Academy of Sciences* **2012**, *109*, 4774–4779.

35. Evans, E. W.; Dodson, C. A.; Maeda, K.; Biskup, T.; Wedge, C. J.; Timme, C. R.; Timmel, C. R. Magnetic field effects in flavoproteins and related systems. *Interface Focus* **2013**, *3*, 20130005.

36. Sheppard, D. M.; Li, J.; Henbest, K. B.; Neil, S. R.; Maeda, K.; Storey, J.; Schleicher, E.; Biskup, T.; Rodriguez, R.; Weber, S.; Hore, P. J.; Timmel, C. R.; MacKenzie, S. R. Millitesla magnetic field effects on the photocycle of an animal cryptochrome. *Scientific Reports* **2017**, *7*, 42228.

37. Xu, J. et al. Cryptochrome 4 from a night-migratory songbird has the magnetic properties required of a light-dependent magnetoreceptor. *Nature* **2021**, in press.

38. Maeda, K.; T Neil, S. R.; Henbest, K. B.; Weber, S.; Schleicher, E.; Hore, P. J.; Mackenzie, S. R.; Timmel, C. R. Following Radical Pair Reactions in Solution: A Step Change in Sensitivity Using Cavity Ring-Down Detection. *Journal of the American Chemical Society* **2011**, *133*, 17807–17815.

39. Evans, E. W.; Li, J.; Storey, J. G.; Maeda, K.; Henbest, K. B.; Dodson, C. A.; Hore, P. J.; Mackenzie, S. R.; Timmel, C. R. Sensitive fluorescence-based detection of magnetic field effects in photoreactions of flavins. *hysical Chemistry Chemical Physics* **2015**, *17*, 18456–18463.

40. Kattnig, D. R.; Evans, E. W.; Déjean, V.; Dodson, C. A.; Wallace, M. I.; Mackenzie, S. R.; Timmel, C. R.; Hore, P. J. Chemical amplification of magnetic field effects relevant to avian magnetoreception. *Nature Chemistry* **2016**, *8*, 384–391.

41. Hore, P. J.; Worster, S. B. Proposal to use superparamagnetic nanoparticles to test the role of cryptochrome in magnetoreception. *Journal of the Royal Society Interface* **2018**, *15*, 20180587.

42. Abbas, C. A.; Sibirny, A. A. Genetic Control of Biosynthesis and Transport of Riboflavin and Flavin Nucleotides and Construction of Robust Biotechnological Producers. *Microbiology and Molecular Biology Reviews* **2011**, *75*, 321–360.

43. Brocklehurst, B. Magnetic isotope effects in biology: A marker for radical pair reactions and electromagnetic field effects? *International Journal of Radiation Biology* **1997**, *72*, 587–596.

44. Hore, P. J. *Nuclear magnetic resonance*; Oxford University Press, 1995.

45. Rodgers, C. T.; Norman, S. A.; Henbest, K. B.; Timmel, C. R.; Hore, P. J. Determination of radical re-encounter probability distributions from magnetic field effects on reaction yields. *Journal of the American Chemical Society* **2007**, *129*, 6746–6755.

46. Ilya Kuprov, Spin dynamics. Spin Interaction Hamiltonians, part I. `http://spindynamics.org/documents/sd_m1_lecture_06.pdf`.

47. Hore, P. J.; Lee, A. A.; Lau, J. C. S.; Hogben, H. J.; Biskup, T.; Kattnig, D. R. Alternative radical pairs for cryptochrome-based magnetoreception.

48. Neese, F. The ORCA program system. *WIREs Computational Molecular Science* **2012**, *2*, 73–78.

49. Beardmore, J. P.; Antill, L. M.; Woodward, J. R. Optical Absorption and Magnetic Field Effect Based Imaging of Transient Radicals. *Angewandte Chemie International Edition* **2015**, *54*, 8494–8497.

50. Evans, E. W.; Kattnig, D. R.; Henbest, K. B.; Hore, P. J.; Mackenzie, S. R.; Timmel, C. R. Sub-millitesla magnetic field effects on the recombination reaction of flavin and ascorbic acid radicals. *The Journal of Chemical Physics* **2016**, *145*, 085101.

51. Brocklehurst, B.; Dixon, R.; Gardy, E.; Lopata, V.; Quinn, M.; Singh, A.; Sargent, F. The effect of a magnetic field on the singlet/triplet ratio in geminate ion recombination. *Chemical Physics Letters* **1974**, *28*, 361–363.

52. Pereiro, I.; Fomitcheva Khartchenko, A.; Petrini, L.; Kaigala, G. V. Nip the bubble in the bud: A guide to avoid gas nucleation in microfluidics. *Lab on a Chip* **2019**, *19*, 2296–2314.

53. Evans, E., Making physics work for biology: using spin chemistry to understand protein mechanism and structure. Ph.D. thesis, University of Oxford, 2016.

54. Buchachenko, A. L. Magnetic Isotope Effect: Nuclear Spin Control of Chemical Reactions. *The Journal of Physical Chemistry A* **2001**, *105*, 9995–10011.

55. Turro, N. J. Influence of nuclear spin on chemical, reactions: Magnetic isotope and magnetic field effects (A Review). *Proceedings of the National Academy of Sciences* **1983**, *80*, 609–621.

56. Henbest, K. B.; Athanassiades, E.; Maeda, K.; Kuprov, I.; Hore, P. J.; Timmel, C. R. Photoionization of TMPD in DMSO solution: mechanism and magnetic field effects. *Molecular Physics* **2006**, *104*, 1789–1794.

57. Hore, P. J. Are biochemical reactions affected by weak magnetic fields? *Proceedings of the National Academy of Sciences* **2012**, *109*, 1357–1358.

58. Weller, A.; Nolting, F.; Staerk, H. A quantitative interpretation of the magnetic field effect on hyperfine-coupling-induced triplet formation from radical ion pairs. *Chemical Physics Letters* **1983**, *96*, 24–27.

59. Stass, D.; Tadjikov, B.; Molin, Y. Manifestation of quantum coherence upon recombination of radical ion pairs in weak magnetic fields. Systems with equivalent nuclei. *Chemical Physics Letters* **1995**, *235*, 511–516.

60. Maeda, K.; Miura, T.; Arai, T. A practical simulation and a novel insight to the magnetic field effect on a radical pair in a micelle. *Molecular Physics* **2006**, *104*, 1779–1788.

61. Solov'Yov, I. A.; Mouritsen, H.; Schulten, K. Acuity of a cryptochrome and vision-based magnetoreception system in birds. *Biophysical Journal* **2010**, *99*, 40–49.

62. Abolpour Homaei, A.; Sariri, R.; Vianello, F.; Stevanato, R. Enzyme immobilization: an update. *Journal of Chemical Biology* **2013**, *6*, 185–205.

63. Zeng, Z.; Wei, J.; Liu, Y.; Zhang, W.; Mabe, T. Magnetoreception of Photoactivated Cryptochrome 1 in Electrochemistry and Electron Transfer. *ACS Omega* **2018**, *3*, 4752–4759.

64. Hartnett, A. M.; Ingersoll, C. M.; Baker, G. A.; Bright, F. V. Chemical Processing of Advanced Materials. *Analytical Chemistry* **1999**, *71*, 1215–1224.

65. Rafferty, C. N.; Clayton, R. K. Properties of Reaction Centers of Rhodopseudomonas Sphaeroides in Dried Gelatin Films. *Biochimica et Biophysica Acta* **1978**, *502*, 51–60.

66. D'Agostino, C.; Liuzzi, R.; Gladden, L. F.; Guido, S. Swelling-induced structural changes and microparticle uptake of gelatin gels probed by NMR and CLSM. *Soft Matter* **2017**, *13*, 2952–2961.

67. Penzer, G. R.; Radda, G. K. Flavins in a Solid Matrix. *Nature* **1967**, *213*, 251–253.

68. Rostas, A.; Einholz, C.; Illarionov, B.; Heidinger, L.; Al Said, T.; Bauss, A.; Fischer, M.; Bacher, A.; Weber, S.; Schleicher, E. Long-Lived Hydrated FMN Radicals: EPR Characterization and Implications for Catalytic Variability in Flavoproteins. *Journal of the American Chemical Society* **2018**, *140*, 16521–16527.

69. Möbius, K.; Savitsky, A.; Nalepa, A.; Malferrari, M.; Francia, F.; Lubitz, W.; Venturoli, G. The Magic of Disaccharide Glass Matrices for Protein Function as Decoded by High-Field EPR and FTIR Spectroscopy. *Applied Magnetic Resonance* **2015**, *46*, 435–464.

70. Wright, W. W.; Guffanti, G. T.; Vanderkooi, J. M. Protein in sugar films and in glycerol/water as examined by infrared spectroscopy and by the fluorescence and phosphorescence of tryptophan. *Biophysical Journal* **2003**, *85*, 1980–1995.

71. Dashnau, J. L.; Zelent, B.; Vanderkooi, J. M. Tryptophan interactions with glycerol/water and trehalose/sucrose cryosolvents: Infrared and fluorescence spectroscopy and ab initio calculations. *Biophysical Chemistry* **2005**, *114*, 71–83.

72. Fiksiński, K.; Frąckowiak, D. Comparison of Various Films Used in Biophysical Investigations as Anisotropic Matrices. *Spectroscopy Letters* **1980**, *13*, 873–889.

73. Drabent, R. Flavomonucleotide Complex Formation Stabilized by Polymer Matrix. *Acta Physica Hungarica* **1985**, *58*, 113–117.

74. Grajek, H.; Zurkowska, G.; Bojarski, P.; Kuklinski, B.; Smyk, B.; Drabent, R.; Bojarski, C. Spectroscopic manifestations of flavomononucleotide dimers in polyvinyl alcohol films. *Biochimica et Biophysica Acta* **1998**, *1384*, 253–267.

75. Kotaki, A.; Yagi, K. Fluorescence Properties of Flavins in Various Solvents. *Journal of Biochemistry* **1970**, *68*, 509–516.

76. Stanley, R. J.; Jang, H. Electronic Structure Measurements of Oxidized Flavins and Flavin Complexes Using Stark-Effect Spectroscopy. *Journal of Physical Chemistry A* **1999**, *103*, 8976–8984.

77. Behrends, R.; Fuchs, K.; Kaatze, U.; Hayashi, Y.; Feldman, Y. Dielectric properties of glycerol/water mixtures at temperatures between 10 and 50 °C. *Journal of Chemical Physics* **2006**, *124*.

78. Valle, L.; Morán Vieyra, F. E.; Borsarelli, C. D. Hydrogen-bonding modulation of excited-state properties of flavins in a model of aqueous confined environment. *Photochemical & Photobiological Sciences* **2012**, *11*, 1051–1061.

79. Visser, A. J. W. G.; Santema, J. S.; Van Hoekt, A. Spectroscopic and Dynamic Characterization of FMN in Reverse Micelles Entrapped Water Pools. *Photochemistry and Photobiology* **1984**, *39*, 11–16.

80. Bystra, K.; Drabent, R.; Szubiakowska, L.; Smyk, B. Spectroscopy Letters Spectral

Properties of Flavins in Hydrophilic Matrices. *Spectroscopy Letters* **1983**, *16*, 513–530.

81. Nielsen, C.; Nørby, M. S.; Kongsted, J.; Solov'Yov, I. A. Absorption Spectra of FAD Embedded in Cryptochromes. *Journal of Physical Chemistry Letters* **2018**, *9*, 3618–3623.

82. Fleming, J., Spectroscopic Studies of Avian Cryptochromes. Ph.D. thesis, University of Oxford, 2020.

83. Tsentalovich, Y. P.; Lopez, J. J.; Hore, P. J.; Sagdeev, R. Z. Mechanisms of reactions of flavin mononucleotide triplet with aromatic amino acids. *Spectrochimica Acta Part A* **2002**, *58*, 2043–2050.

84. Lakowicz, J. R. *Principles of Fluorescence Spectroscopy, Third Edition*; Springer, New York, 2006.

85. Johansson, L.; Davidsson, A.; Lindblom, G.; Razi Naqvi, K. Bio-chemistry 15. *Biochemistry* **1979**, *18*, 4249–4253.

86. Antill, L. M.; Beardmore, J. P.; Woodward, J. R. Time-resolved optical absorption microspectroscopy of magnetic field sensitive flavin photochemistry. *Review of Scientific Instruments* **2018**, *89*, 023707.

87. Partch, C. L.; Sancar, A. Photochemistry and Photobiology of Cryptochrome Blue-light Photopigments: The Search for a Photocycle. *Photochemistry and Photobiology* **2005**, *81*, 1291–1292.

88. Zirak, P.; Penzkofer, A.; Moldt, J.; Pokorny, R.; Batschauer, A.; Essen, L. O. Photocycle dynamics of the E149A mutant of cryptochrome 3 from Arabidopsis thaliana. *Journal of Photochemistry and Photobiology B: Biology* **2009**, *97*, 94–108.

89. Shirdel, J.; Zirak, P.; Penzkofer, A.; Breitkreuz, H.; Wolf, E. Absorption and fluorescence spectroscopic characterisation of the circadian blue-light photoreceptor cryptochrome from Drosophila melanogaster (dCry). *Chemical Physics* **2008**, *352*, 35–47.

90. Sengupta, A.; Khade, R. V.; Hazra, P. pH dependent dynamic behavior of flavin mononucleotide (FMN) and flavin adenine dinucleotide (FAD) in femtosecond to

nanosecond time scale. *Journal of Photochemistry and Photobiology A: Chemistry* **2011**, *221*, 105–112.

91. Esposito, R.; Delfino, I.; Portaccio, M.; Iannuzzi, C.; Lepore, M. An insight into pH-induced changes in FAD conformational structure by means of time-resolved fluorescence and circular dichroism. *European Biophysics Journal* **2019**, *48*, 395–403.

92. Halle, B.; Davidovic, M. Biomolecular hydration: From water dynamics to hydrodynamics. *Proceedings of the National Academy of Sciences* **2003**, *14*, 12135–12140.

93. Visser, A. J. W. G.; Lee, J. Lumazine Protein from the Bioluminescent Bacterium Photobacterium phosphoreum. A Fluorescence Study of the Protein-Ligand Equilibrium. *Biochemistry* **1980**, *19*, 4366–4372.

94. Bae, S. H.; Dyson, H. J.; Wright, P. E. Prediction of the rotational tumbling time for proteins with disordered segments. *Journal of the American Chemical Society* **2009**, *131*, 6814–6821.

95. Cheng, N. S. Formula for the viscosity of a glycerol-water mixture. *Industrial and Engineering Chemistry Research* **2008**, *47*, 3285–3288.

96. *Personal communication from Prof Henrik Mouritsen's lab.*

97. Murakami, M.; Maeda, K.; Arai, T. Dynamics of intramolecular electron transfer reaction of FAD studied by magnetic field effects on transient absorption spectra. *J. Phys. Chem. A* **2005**, *109*, 5793–5800.

98. Brazard, J.; Usman, A.; Lacombat, F.; Ley, C.; Martin, M. M.; Plaza, P. New Insights into the Ultrafast Photophysics of Oxidized and Reduced FAD in Solution. *The Journal of Physical Chemistry A* **2011**, *115*, 3251–3262, PMID: 21438617.

99. Li, G.; Glusac, K. D. Light-triggered proton and electron transfer in flavin cofactors. *Journal of Physical Chemistry A* **2008**, *112*, 4573–4583.

100. Li, H.; Melø, T. B.; Razi Naqvi, K. Triplets, radical cations and neutral semiquinone radicals of lumiflavin and riboflavin: An overhaul of previous pump-probe data and new multichannel absolute absorption spectra. *Journal of Photochemistry and Photobiology B: Biology* **2012**, *106*, 34–39.

101. Bernt Melø, T.; Adriana Ionescu, M.; Haggquist, G. W.; Razi Naqvi, K. Hydrogen abstraction by triplet flavins. I: Time-resolved multi-channel absorption spectra of flash-irradiated riboflavin solutions in water. *Spectrochimica Acta - Part A: Molecular and Biomolecular Spectroscopy* **1999**, *55*, 2299–2307.

102. Hemmerich, P.; Knappe, W.-R.; Kramer, H. E. A.; Traber, R. Distinction of 2e- and 1e- Reduction Modes of the Flavin Chromophore as Studied by Flash Photolysis. *European Journal of Biochemistry* **1980**, *104*, 511–520.

103. Green, M.; Tollin, G. Flash Photolysis of Flavins I - Photoreduction in Non-aqueous Solvents. *Photochemistry and Photobiology* **1968**, *7*, 129–143.

104. Kao, Y. T.; Saxena, C.; He, T. F.; Guo, L.; Wang, L.; Sancar, A.; Zhong, D. Ultrafast dynamics of flavins in five redox states. *Journal of the American Chemical Society* **2008**, *130*, 13132–13139.

105. Van Stokkum, I. H.; Larsen, D. S.; Van Grondelle, R. Global and target analysis of time-resolved spectra. *Biochimica et Biophysica Acta - Bioenergetics* **2004**, *1657*, 82–104.

106. van Wilderen, L. J. G. W.; Lincoln, C. N.; van Thor, J. J. Modelling Multi-Pulse Population Dynamics from Ultrafast Spectroscopy. *PLOS ONE* **2011**, *6*, 1–14.

107. McPherson, A.; Gavira, J. A. Introduction to protein crystallization. *Acta Crystallographica Section F: Structural Biology Communications* **2014**, *70*, 2–20.

108. Dodson, C. A.; Wedge, C. J.; Murakami, M.; Maeda, K.; Wallace, M. I.; Hore, P. J. Fluorescence-detected magnetic field effects on radical pair reactions from femtolitre volumes. *Chemical Communications* **2015**, *51*, 8023–8026.

109. Déjean, V.; Konowalczyk, M.; Gravell, J.; Golesworthy, M. J.; Gunn, C.; Pompe, N.; Foster Vander Elst, O.; Tan, K. J.; Oxborrow, M.; Aarts, D. G.; Mackenzie, S. R.; Timmel, C. R. Detection of magnetic field effects by confocal microscopy. *Chemical Science* **2020**, *11*, 7772–7781.

110. `https://www.microscopyu.com`.

111. `https://www.leica-microsystems.com/science-lab/science-lab-home/`.

112. `https://www.olympus-lifescience.com/en/microscope-resource/`.

113. http://zeiss-campus.magnet.fsu.edu.

114. Lostao, A.; Gómez-Moreno, C.; Mayhew, S. G.; Sancho, J. Differential Stabilization of the Three FMN Redox Forms by Tyrosine 94 and Tryptophan 57 in Flavodoxin from Anabaena and Its Influence on the Redox Potentials. *Biochemistry* **1997**, *36*, 14334–14344, PMID: 9398151.

115. Chayen, N. E.; Saridakis, E. Protein crystallization: From purified protein to diffraction-quality crystal. *Nature Methods* **2008**, *5*, 147–153.

116. Cvetkovic, A.; Picioreanu, C.; Straathof, A. J.; Krishna, R.; Van Der Wielen, L. A. Relation between pore sizes of protein crystals and anisotropic solute diffusivities. *Journal of the American Chemical Society* **2005**, *127*, 875–879.

117. Lorén, N.; Hagman, J.; Jonasson, J. K.; Deschout, H.; Bernin, D.; Cella-Zanacchi, F.; Diaspro, A.; McNally, J. G.; Ameloot, M.; Smisdom, N.; Nydén, M.; Hermansson, A.-M.; Rudemo, M.; Braeckmans, K. Fluorescence recovery after photobleaching in material and life sciences: putting theory into practice. *Quarterly Reviews of Biophysics* **2015**, *48*, 323–387.

118. Cvetkovic, A.; Straathof, A. J.; Hanlon, D. N.; Van Der Zwaag, S.; Krishna, R.; Van Der Wielen, L. A. Quantifying anisotropic solute transport in protein crystals using 3-D laser scanning confocal microscopy visualization. *Biotechnology and Bioengineering* **2004**, *86*, 389–398.

119. Aarts, D.; Lekkerkerker, H. Confocal scanning laser microscopy on fluid-fluid demixing colloid-polymer mixtures. *Journal of Physics Condensed Matter* **2004**, *16*, 4231–4242.

120. Simeonova, N. B.; Kegel, W. K. Real-space fluorescence recovery after photo-bleaching of concentrated suspensions of hard colloidal spheres. *Faraday Discussions* **2003**, *123*, 27–35.

121. Tzedakis, T.; Kane, C.; Roche, J.; Groenen Serrano, K.; Reynes, O. Electrochemical study in both classical cell and microreactors of flavin adenine dinucleotide as a redox mediator for NADH regeneration. *Electrochimica Acta* **2009**, *55*, 2286–2294.

122. Velev, O. D.; Kaler, E. W.; Lenhoff, A. M. Surfactant diffusion into lysozyme crystal matrices investigated by quantitative fluorescence microscopy. *Journal of Physical Chemistry B* **2000**, *104*, 9267–9275.

123. McPherson, A. Penetration of dyes into protein crystals. *Acta Crystallographica Section F: Structural Biology Communications* **2019**, *75*, 132–140.

124. Hense, A.; Herman, E.; Oldemeyer, S.; Kottke, T. Proton transfer to flavin stabilizes the signaling state of the blue light receptor plant cryptochrome. *Journal of Biological Chemistry* **2015**, *290*, 1743–1751.

125. Liu, B.; Liu, H.; Zhong, D.; Lin, C. Searching for a photocycle of the cryptochrome photoreceptors. *Current Opinion in Plant Biology* **2010**, *13*, 578–586.

126. Zollitsch, T., Investigation of Magnetic Field Effects on Protein Photochemistry using Cavity Enhanced Spectroscopy. Ph.D. thesis, University of Oxford, 2018.

127. Maeda, K.; Henbest, K. B.; Cintolesi, F.; Kuprov, I.; Rodgers, C. T.; Liddell, P. A.; Gust, D.; Timmel, C. R.; Hore, P. J. Chemical compass model of avian magnetoreception. *Nature* **2008**, *453*, 387–390.